FABRICATION AND CHARACTERIZATION OF HIGH EFFICIENCY DYE-SENSITIZED SOLAR CELL BASED ON TiO_2 NANOFIBER PHOTOANODE

YANG LIJUN

Ph.D

The Hong Kong Polytechnic University

2014

The Hong Kong Polytechnic University

Department of Mechanical Engineering

Fabrication and Characterization of High Efficiency Dye-sensitized Solar Cell Based on TiO_2 Nanofiber Photoanode

Yang Lijun

A thesis submitted in partial fulfillment of the requirement for the degree of Doctor of Philosophy

May 2013

CERTIFICATE OF ORIGINALITY

I hereby declare that this thesis is my own work and that, to the best of my knowledge and belief, it reproduces no material previously published or written, nor material that has been accepted for the award of any other degree or diploma, except where due acknowledgement has been made in the text.

(Signed)

Yang Lijun (Name of Student)

Abstract

Dye sensitized solar cell (DSSC) offers the advantages of low-cost, high-efficiency, and large flexibility in color, shape and transparency. However, the highest power conversion efficiency to-date is 15% for a small size device, which is still too low to be considered as a commercially viable technology. The power conversion efficiency of the photovoltaic device can be expressed as the product of three factors - the light absorption efficiency, the charge injection efficiency, and the charge collection efficiency. Improvement in any of these factors alone, or in combination, could certainly improve the performance of the DSSC device.

In this study, the one-dimensional nanostructure made out of TiO_2 nanofibers has been adopted as the photoanode of the DSSC, which provides several advantages. The one-dimensional nanofiber configuration provides a direct path for transport and collection of electrons. In addition, a large surface-to-volume ratio that favors dye adsorption can be attained as the TiO_2 nanofiber is composed of closely packed anatase single crystallites with sizes less than 10 nm. In consequence, a high efficiency of 7.14% has been obtained in our DSSC device using a TiO_2 nanofiber photoanode.

To further improve the efficiency of the DSSC based on TiO_2 nanofiber photoanode, two different novel scattering configurations have been introduced, in the photoanode to improve the light harvesting efficiency. A high efficiency of 8.71% and 9.28% has been achieved, respectively, with the polydispersed-size TiO_2 nanoparticles and the large-diameter TiO_2 nanofibers as the scattering layer.

Other than trapping the incident light, another improvement has been made on light harvesting by adopting the dye cocktail approach. A novel design of core-shell photoanode where a thin-shell of infrared dye is deposited on the core of sensitized TiO_2 nanofiber has been developed. Specifically, the ruthenium-based dye (N719) sensitized TiO_2 nanofibers are wrapped by thin-shell of copper phthalocyanine (CuPc). In this architecture, photons are absorbed by the infrared dye and undergo charge transfer to the sensitizing dye, and subsequently to the TiO_2. This approach not only broadens the absorption spectrum, it also further suppresses the recombination of electrons and the electrolytes, which is a common limiting factor on performance of DSSC using TiO_2. The highest efficiency attained is 9.48%.

Finally, to enhance the charge transport and collection efficiency, multiwall carbon nanotube is incorporated in the TiO_2 nanorods, which make up the

photoanode. The multiwall carbon nanotubes inside the nanorods can effectively transport and collect photogenerated electrons and reduce the recombination, both of which improve the efficiency of the device. The maximum efficiency achieved is 10.24% accompanied with a high fill factor of 74%.

Publications

Journals:

[1] Lijun Yang, Wallace Woon-Fong Leung. Electrospun TiO_2 nanorods with carbon nanotubes for efficient electron collection in Dye-Sensitized Solar Cells. *Advanced Materials*, 25(2013) 1792

[2] Lijun Yang, Wallace Woon-Fong Leung. Application of a bilayer TiO_2 nanofiber photoanode for optimization of Dye-Sensitized Solar Cells. *Advanced Materials*, 23(2011)4559

[3] Lijun Yang, Wallace Woon-Fong Leung. Improvement of Light Harvesting in Dye Sensitized Solar Cell Based on Cascade Charge Transfer, *Nanoscale*, 5(2013), 7493-7498

[4] Lijun Yang, Wallace Woon-Fong Leung. A Novel Scattering Layer composed of Electrosprayed Polydispersed-size Nanocrystallite TiO_2 for High Efficiency Dye Sensitized Solar Cell, *RSC Advances*, 3(2013), 25707-25710

[5] Lijun Yang, Wallace Woon-Fong Leung. Optimizing Scattering Layer for Efficient Dye Sensitized Solar Cells Based on TiO_2 Nanofiber, submitted for publication.

US Patent Applications:

[1] Wallace Woon-Fong Leung, Lijun Yang, Bilayer Dye Sensitized Solar Cell and Fabrication Method Thereof. US2013/0074913 A1

[2] Wallace Woon-Fong Leung, Lijun Yang, Dye- Sensitized Solar Cell based on indirect charge transfer. US20130298981 A1

[3] Wallace Woon-Fong Leung, Lijun Yang. Electrospun TiO_2 nanorods with carbon nanotubes for efficient electron collection in Dye-Sensitized Solar Cells.

Conference

2011 Lijun Yang, Wallace Woon-Fong Leung. “Application of a bilayer TiO_2 nanofiber photoanode for optimization of Dye-Sensitized Solar Cells” MRS Fall 2011, Boston, MA, 2011.

2012 Lijun Yang and Wallace WF Leung, “Enhancing Performance of Dye Sensitized Solar Cell using a Bilayer Nanofiber Configuration” Int. Mech. Eng. Congress Exposition, Houston, TX, Nov 12, 2012, IMECE2012-86242.

2013 Lijun Yang and Wallace WF Leung, “Electrospun TiO2 Nanorod with Carbon Nanotube for Efficient Electron Collection in Dye Sensitized Solar Cell”, Int. Mech. Eng. Congress Exposition, San Diego, CA, Nov 19, 2013, IMECE2013-65486

Acknowledgements

I have to admit that the acknowledgements part is difficult for me to start and I have finally finished it at last. Along with writing my thesis, I realize that I have owed a lot to my colleagues and collaborators. I hope that I can take this opportunity to express my heartfelt thanks to each of them, regardless of whether they could see this by chance. I cannot accomplish my study without their encouragement and support.

First of all, I want to thank my supervisor Professor Wallace Leung for giving me the opportunity to study in the Hong Kong Polytechnic University. He has always been kind and patient to me. I still remember at the beginning of my research, I cannot fabricate any nanofiber. However, he did not blame on me; instead he supported and encouraged me in the due course. His perseverance and passion in research guided me through the difficulties that I have encountered in my study, and I certainly have picked up this virtue that would accompany me in my future endeavor.

I have to thank Dr. Chuanjun Huang for his kind advice when I first entered the new field of DSSC several years ago. I also want to thank Dr. Yuanhao Wang for his selfless discussions and assistances in my research during my hurdles. I want to express my sincere thanks to Mr. Yiu-Kwok Au from Applied Biology and Chemical Technology, who has helped me in carrying out measurement of the absorption and reflectance spectrum on the photoanode.

I would like to express my thanks to my colleagues, Zongrong Wang, Xiaochen Ren, Tracy Lam, Enna Ha and Min Guo, who gave me lots of help in my experiments. Many thanks also go to my research group mates, Carina, Eva, Harry and Kenneth. I cannot forget the “happy days” when we discussed and debated on issues together.

Finally, I sincerely thank my beloved parents for bringing me up and sharing their relentless love to me. I have to thank my sister Liping for her understanding and support during my study in Hong Kong. Last but not least, none of this would be possible without the support and encouragement from my husband Jingchuan Wang.

Table of contents

List of Figures

List of Tables

List of Abbreviations

AM: air mass

CB: conduction band

CT: charge transfer

CNT: carbon nanotube

DSSC: dye sensitized solar cell

EIS: electrochemical impedance spectra

EQE: external quantum efficiency

ET: electron transfer

FF: fill factor

FTO: fluorine doped tin oxide glass

FRET: Förster resonance energy transfer

HOMO: highest occupied molecular orbital

HTM: hole transport material

ITO: indium doped tin oxide glass

J_{sc}: short circuit current density

PCE: power conversion efficiency

PL: photoluminescence

PMII: 1-methy-3-propylimidazolium iodide

PVP: polyvinylpyrrolidone

LUMO: lowest unoccupied molecular orbital

LHE: light harvesting efficiency

MWCNT: multiwall carbon nanotube

VB: valence band

V_{oc}: open circuit voltage

TBP: 4-tert-butylpyridine

TIP: titanium isopropoxide

Chapter 1

Introduction

In an effort to preserve the global environment and ensure sustainable economic growth, developing clean alternatives to current power generation methods is extremely important. Among all the available technologies to produce clean and renewable energy, photovoltaic devices (PV), for which electricity is generated directly from sunlight, is a promising solution for the alternative energy sources. Given the earth receives an annual average insolation of 1.2×10^{17} W, covering just 0.13% of the earth's surface with solar cells with an efficiency of 10% would satisfy our daily needs[1, 2]. However, the cost of production using existing well commercialized silicon-based photovoltaic technologies are too high to be competitive with conventional power generation, such as from hydrocarbons. Since the report on a low-cost and high-efficiency dye sensitized solar cell (DSSC) appeared in 1991, it has attracted intense interest as a promising substitute for conventional silicon-based solar cell[3-5]. A record high efficiency of 15% for small solar cells has been achieved recently[6]. Many theoretical and experimental researches have been carried out with an attempt to further improve the performance of the DSSC for successful commercialization. However, these efficiencies are much below that of the multi-crystalline silicon solar cell, which stands at about 20%.

Therefore, it is imperative to enhance the efficiency of DSSC in order to bring this photovoltaic technology closer to commercial target. In the next few sections, we will introduce the background and also provide a review of the relevant literatures.

1.1 Photovoltaic Energy Conversion

Photovoltaic energy conversion is the direct production of electrical energy in the form of voltage and current from electromagnetic energy, such as light. There are four basic steps needed for photovoltaic energy conversion:

(1) Light absorption which cause a transition in the absorber from the ground state to an excited state;

(2) Conversion of the excited state into a free negative- and- positive charge carrier pair;

(3) Resultant free negative charge carrier moves toward a positive electrode (cathode) outside the cell or device, while the resultant free positive charge carrier moves oppositely to the negative electrode (anode) outside the cell or device.

After arriving at the anode in the cell the energetic, photogenerated, negative charged electrons leave the anode travelling through an external electrical circuit towards the cathode. Along this path, they lose their electrical energy by carrying out work. In the cell, the charge carriers (e.g. ions) carry the negative charge to the anode thus “completing” the circuit. At the anode, the ions give up the free electrons and all the returned electrons complete the (4th) step of photovoltaic energy conversion.

(4) Combining with a supply of negative-charge carrier or electron, the absorber is returned back to the ground state.

In some materials (the absorber), the excited state may be a photogenerated free electron-hole pair, in which case step 1 and 2 are combined. In other materials, the excited state may be an exciton, in which case step 1 and 2 are distinctly separated[7].

1.2 Solar Cell

1.2.1 Background

M. A. Green has grouped various photovoltaic solar cells in three major categories (Fig 1.1)[8] based on the nature of the materials, maximum power conversion efficiency and associated cost of electric power generation. The first generation solar cells use materials of the highest purity, such as single-crystal silicon. The maximum efficiency obtained to-date is from the first generation solar cells. However, the cost per watt is also the highest too because of the high labor and energy cost for material processing. The cost for power conversion is presently about US$1 per watt, however, it depends highly on the price of the silicon materials.

The second generation solar cells are based on low energy, thin-film technologies such as electroplating and vapor deposition. The advantages of these solar cells are (a) easy to manufacture allowing a significant reduction of the fabrication cost to less than $1 per watt, (b) extensive applications with attractive appearance, and (c) possibilities of using flexible substrates. Unfortunately, due to difficulty in preparing materials without defects the power conversion efficiency is lower when compared with the first-generation solar cells. Examples of most efficient thin-film system are made of multi-crystalline or amorphous Si, CdTe and CdInGaSe (CIGS). The efficiency of amorphous Si is lower than that of single-crystal Si, yet it has an advantage of a lower temperature coefficient for power loss, and it is only slightly cheaper than that of single crystal Si primarily because it requires expensive equipment for manufacturing. The highest efficiency of CdTe for a laboratory unit is 16.7% and for a module efficiency is 10.9% [9]. The disadvantages of the CdTe thin-film solar cells are the toxicity, lack of raw materials for fabrication, temperature-dependent efficiency, and only average tolerance for light intensity. The CIGS systems can achieve high efficiencies (19.4% in the laboratory, and 16.7% in sub-modules) and they are durable with low material cost[10]. However, the manufacturing cost of this type of solar cell is expensive due to the complicated fabrication processes.

According to Shockley and Queisser calculation, the thermodynamic efficiency limit is 31% for single-junction solar cell. Suppose absorption of an individual photon results in the formation of a single electron-hole pair and all of the photon energy beyond the energy band-gap is lost in form of heat. This limitation can be overcome by utilizing various types of the third-generation solar cells, such as dye sensitized solar cell (DSSC), polymer organic- buck hetero-junction and quantum dots. In principle, sunlight can be converted into electricity at efficiency near the Carnot cycle limit of 95%. The objective for the third-generation solar cells is to generate electricity with a competitive price, say, less than $0.5 per watt. If the photovoltaic devices which are produced by techniques that allow facile mass production, the impact on economics can be enormous rendering photovoltaic technology one of the most cost-effective options for future green-and renewable energy production.

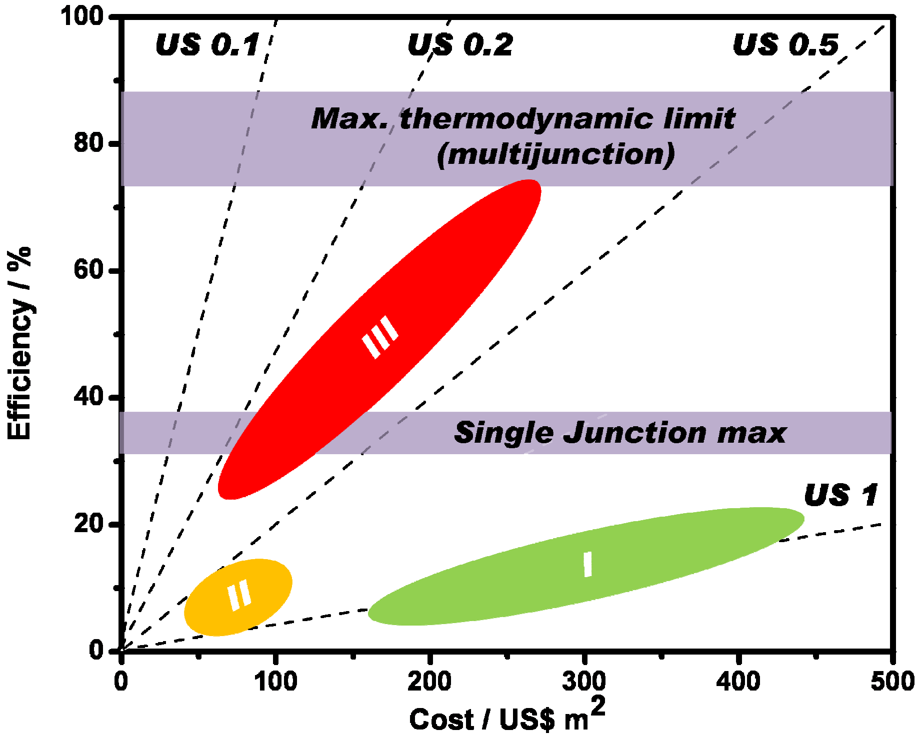

Fig 1.1 Classification of solar cell into three categories, based on the nature of materials used and associated cost of electric power generation

1.2.2 Operating principle of solar cell based on p-n junction

In a bulk crystalline semiconductor, the highest occupied molecular orbital (HOMO) and lowest unoccupied molecular orbital (LUMO) of constitute atoms/ molecules converge into valence and conduction band, respectively. In the absence of dopants, the Fermi level of the semiconductor lies in the middle of the separation gap between the valence band and conduction band. Upon doping with electron donors (n-type semiconductor) rendering the material electron-rich, the corresponding Fermi level moves closer to the conduction band. Similarly, doping with electron-acceptors (p-type semiconductor) would deplete the electron and the Fermi level will move closer to the valence band. Excitation of the semiconductor with energy higher than the energy band gap lead to generation of free charge carriers, i.e., electron-and-hole pairs. In a configuration consisting of both n-type and p-type semiconductors, charge separation occurs due to bending of the bands in the depletion layer (Fig.1.2).

Upon illumination, additional carriers are generated, and the single Fermi level splits into two quasi-Fermi levels in the p-type and n-type region. These quasi-Fermi levels are split. Close to the electrode both quasi-Fermi levels collapse toward the majority quasi-Fermi level, where they are reconnected. This shift of the Fermi level represents the open-circuit voltage (V_{oc}, Fig 1.2). Such separation of the charge carriers allows selective collection at the collector electrode and a net conversion of sunlight to electric power [2, 8, 11, 12].

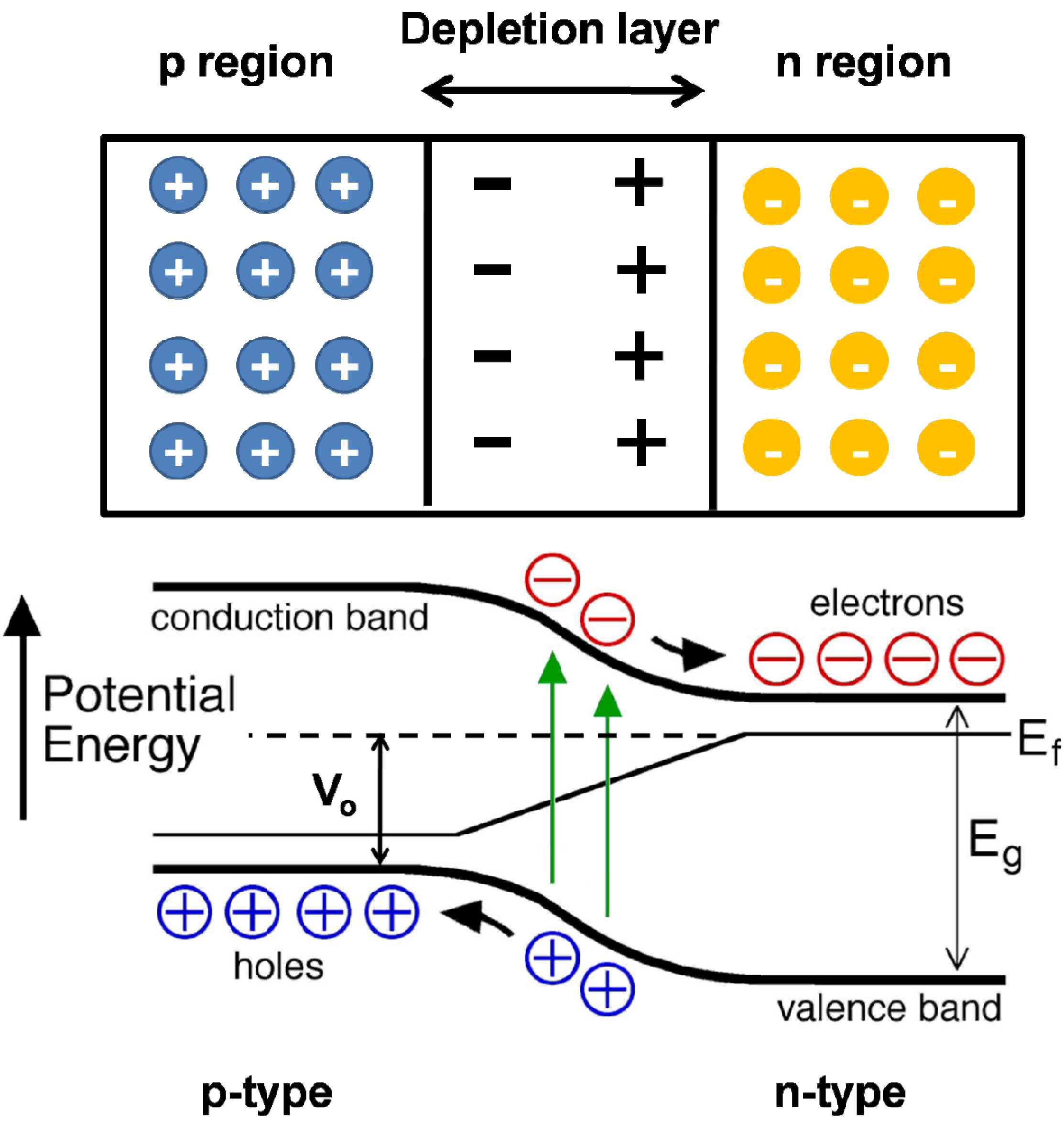

Fig 1.2 Energy diagram of p-n junction solar cell

1.3 Dye Sensitized Solar Cell

1.3.1 Background and structure of DSSC

DSSC can be seen as a technology between the second and third generation of solar cells, which has the potential to become the third-generation photovoltaic device based on nanostructure configuration.

The history of DSSC can be traced back to 1887, Moser observed the first case of dye sensitized semiconductor electrode when using the dye erythrosin on silver halide electrode[13]. Not until 1960s, researchers finally understood the operating mechanism and fabricated the first-generation DSSC based on zinc oxide [14-16]. However, the power conversion efficiency of this prototype DSSC was way too low due to the limited light absorption. For the next couple of years, a lot of efforts were put into the basic research, selecting the photoelectrode materials, optimizing the dye with a high molar extinction coefficient. All these efforts finally led to the announcement in 1990’s of the sensitized nanocrystalline photovoltaic device with a conversion efficiency of 7.1 -7.9 % under solar illumination and 12% in diffuse daylight[17]. This non-conventional solar technology has attracted intense interest as a promising substitute for conventional silicon-based solar cell due to its low-cost, environmental compatibility and high efficiency. DSSC performs also better than other photovoltaic devices under diffuse light conditions and at higher temperature. Moreover, it offers the design flexibility on color, shape and transparency. To-date, the power conversion efficiency of over 12% has been achieved for the device that contains liquid electrolyte, whereas the counter-part, solid state, reaches an overall efficiency of 15%.

The basic structure of a typical DSSC is composed of a sensitized mesoporous wide band-gap semiconductor, i.e., the sensitized photoanode, a counter electrode and an electrolyte [1, 3, 18]. The photoanode is the key component in DSSC, which captures the photons and transport them to the substrate. Generally the photoanode utilizes the fluorine-doped tin oxide (FTO) glass as the substrate coated with a layer of mesoporous TiO_2 (10 ～ 20μm), subsequently it is sensitized with an appropriate dye. There are many different wide band-gap semiconductors, such as ZnO, and SnO_2 etc., that can be used in the photoanode system. Among these, TiO_2 still shows the highest efficiency [19-21]. The electrolyte is divided into three types according to the viscosity: liquid, gel and solid state. The liquid electrolyte is widely used and intensively studied owing to its fast ion diffusion and low viscosity. Due to concerns on solvent leakage and long-term stability of liquid electrolyte, solid state electrolyte has been developed as a replacement. The solid state-electrolyte, which is also called hole transport materials (HTM), through which holes transfer from the dye to the metallic counter electrode by hopping. One problem of the solid-state electrolyte is that it is difficult for the electrolyte to penetrate deeply into the photoanode, which limits the practical thickness of the photoanode. The gel-state electrolyte is between liquid and solid-state electrolyte, which shows lower performance than that of liquid state electrolyte. This is attributed to limited mobility of the redox couple in the gel electrolyte[22]. To balance the charge and regenerate the key components, the oxide species needs to be reduced by electron flowing through the external circuit returning back to the counter electrode. Typically, in liquid-based DSSC device, counter electrode is made of FTO glass coated with a thin film of catalyst, such as platinum and carbonaceous materials, etc. Usually, platinum (Pt) coated FTO is used as the counter electrode because Pt shows excellent chemical stability and low over-potential for the I_3^- reduction reaction. While in solid-state DSSC device, metallic counter electrode is directly deposited on photoanode in form of a thin layer. In most cases, gold and silver are adopted as the counter electrode in solid-state DSSC.

1.3.2 Operating principle of DSSC

DSSC is different from the conventional p-n junction photovoltaic devices in that it separates the function of light absorption from charge carrier transport. The operating principle of DSSC is shown in Fig.1.3. Upon illumination, the surface anchored dyes are sensitized to the excited state (S*) by light absorption at the interface, and an electron-hole pair is generated with electrons subsequently injected into the conduction band of the semiconductor (usually TiO_2) while the holes, at least initially, remain on the sensitizers. The dye ground state (S) is then regenerated by electron donation from the redox system to the oxidized state of the sensitizer (S^+). The recovery of redox system is realized by transporting holes to the counter electrode by diffusing or hopping (depending on the transporting mediator, i.e. the liquid electrolyte, or hole transport materials). The entire process is completed by electron transport through the external circuit and the device generates electric power from sunlight without chemical transformation. As evident, the dye sensitized TiO_2 system has mainly two functions: the dye absorbs light upon illumination and charge carriers are generated and separated in TiO_2.

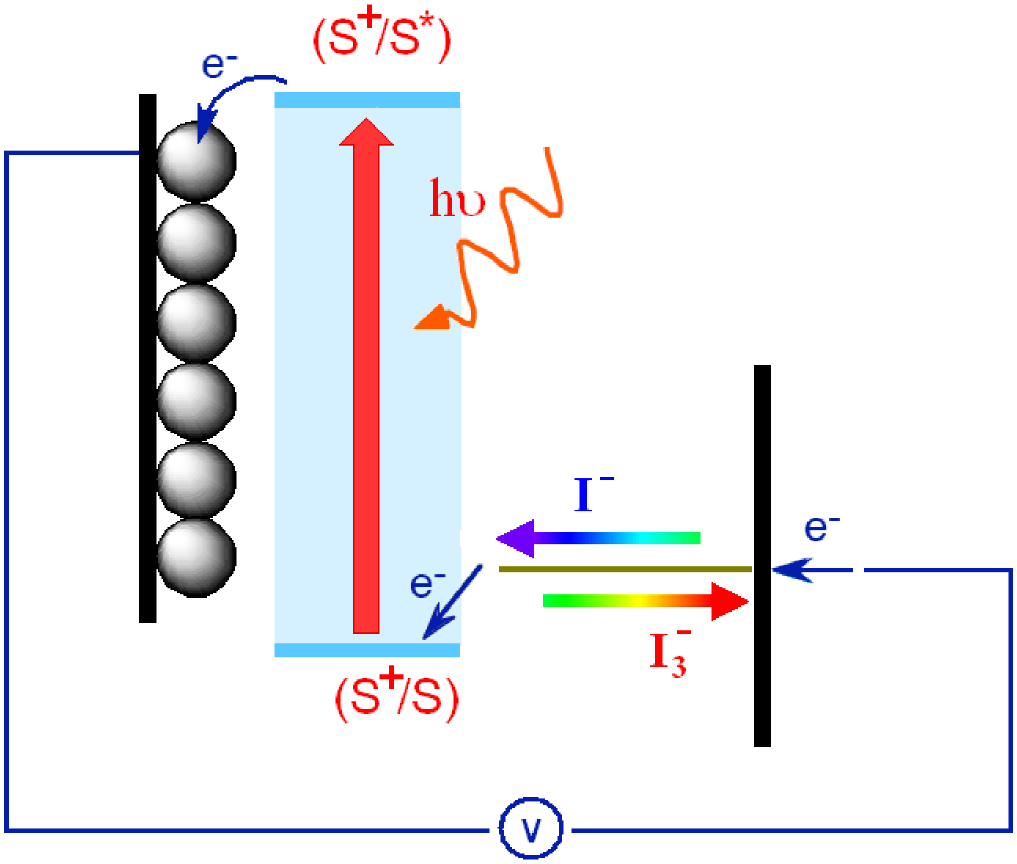

Fig 1.3 Principle of operation of the nanocrystalline TiO_2 dye-sensitized solar cells

1.3.3 Light absorption and charge generation

Light is absorbed in the absorber (dye) located at the semiconductor-semiconductor, or semiconductor-electrolyte hetero-junction. The light harvesting efficiency (LHE) is given by Eq 1.1

$$\mathbf{LHE(\lambda) = 1 - 10^{-\Gamma\sigma(\lambda)}} \tag{1.1}$$

where Γ is the number of moles of the sensitizer(dye) per square centimeter of projected surface area of the film. σ is the absorption cross-sectional area at the wavelength λ in units of cm^2 mol^{-1} obtained from the decadic extinction coefficient, ε (units of M^{-1} cm^{-1}). The LHE is directly determined by the surface concentration of the dyes in the film, and the molar extinction coefficient of dye. Ruthenium-based complexes are the most commonly used photosensitizers. For the liquid-based electrolyte DSSC increasing the extinction coefficient of the sensitizer is not the main issue, because the photoanode functions efficiently up to 20 μm thickness. To-date, ruthenium-based complexes, such as N3, i.e. *cis*-$RuL_2(NCS)_2$ (L_2 =4,4′-dicarboxy-2,2′-bipyridyl), and N719 (for the di-tetrabutylammonium salt of N3) are the most widely used sensitizers due to their high absorption coefficients at 518nm, respectively of 1.3×10^4 $Lmol^{-1}cm^{-1}$ and 1.33×10^4 $Lmol^{-1}cm^{-1}$ [23]. An alternative strategy might be the co-sensitized or “dye cocktail” where a sensitizer is absorbed together with another sensitizer which has a complementary absorption region at different wave length ranges [24-26].

1.3.4 Charge transfer process in DSSC

DSSC is a photovoltaic device in which several electron transfer (ET) processes are taking place concurrently either without, or with, competition [18, 27-29]. Given the highest energy conversion efficiency has been achieved by the mesoporous TiO_2 film, sensitized with a Ru-based complex dye and filled with I^-/I_3^- electrolyte, the following discussion will be focused primarily on such DSSC configuration. Fig 1.4 shows the typical time scales for the processes involved in such a DSSC device. Upon illumination, the sensitizer is excited in a few femto-seconds(fs) (Eq. 1.2) and electron is injected extremely fast from S* to the conduction band of the TiO_2 (Eq. 1.3) on the order of subpico-second(subps) time scale. The ground state of the sensitizer is regenerated subsequently by I^- in the micro-second (μs) domain (Eq. 1.4). The exchange current density for reduction of tri-iodide at the counter electrode has been measured to be 10^{-2} –10^{-1} Acm^{-2}(Eq.1.5). Recombination of electron in TiO_2 with the S^+ (Eq. 1.6) can occur in the milli-second(ms) time range. This is followed by the processes of: (i) electron transfer by diffusion across the nanocrystalline film with time scale of 5 milli-second(ms) and (ii) the redox capture the electron by the oxidized relay (back reaction, Eq. 1.7), I_3^-, within milli-seconds(ms) even seconds. The similar time scales for both processes, i.e. recombination and diffusion, induces a practical issue on achieving high conversion efficiencies in DSSC. In a simple model, an electron collection efficiency at short circuit condition can be defined as $\Phi_{col} = k_{trans} / (k_{trans} + k_{rec})$ where k_{trans} and k_{rec} are the first-order rate constants for the electron transport and the recombination, respectively, indicating that a fast electron transport in TiO_2 and a slow recombination are preferred.

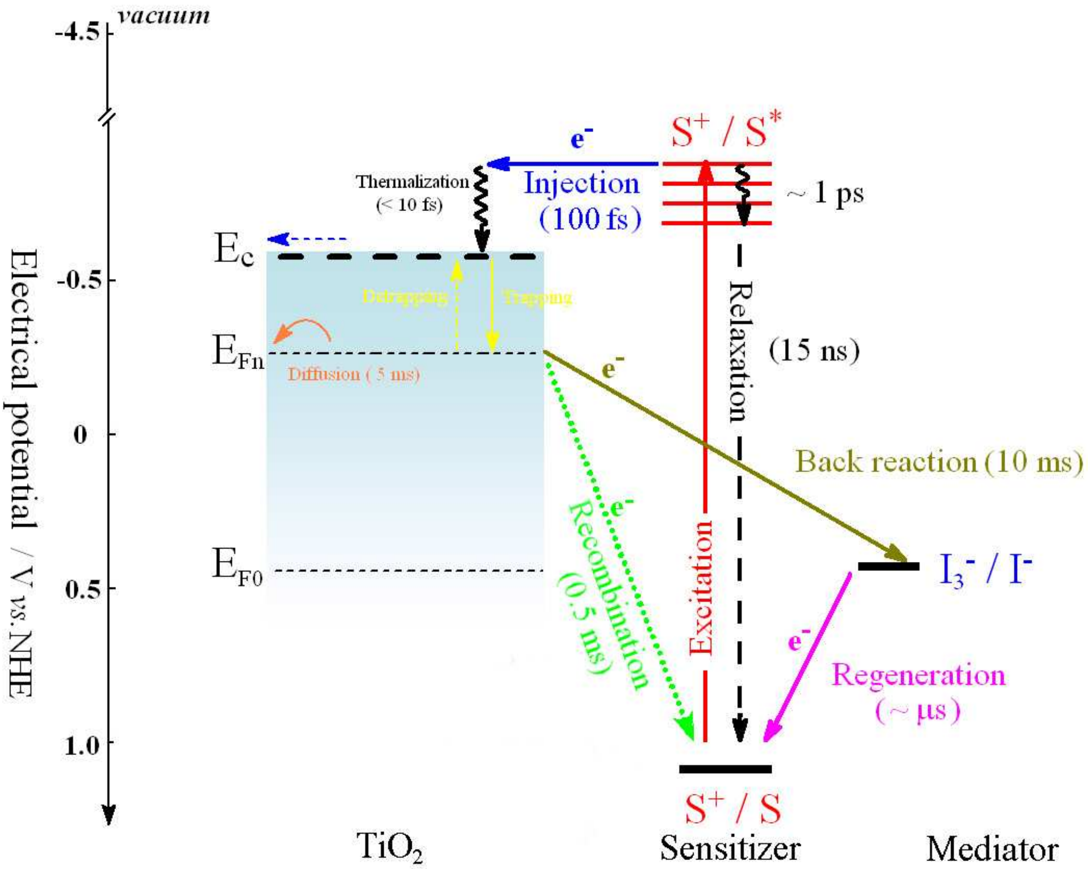

Fig 1.4 Dynamics of different electron transfer processes in the conversion of light to electric power by a DSSC. The time scales in parentheses are representative values for each process[18].

$S|TiO_2 + h\nu \rightarrow S^*|\, TiO_2$ Photoexcitation (1.2)

$S^*|\, TiO_2 \rightarrow S^+|\, TiO_2 + e^-(CBTiO_2)$ Charge injection

(1.3)

$S^{+}|TiO_2 + I^{-} \rightarrow S|TiO_2 + I^{-}_2$ Regeneration (1.4)

$I^{-}_3 + e^{-}(\text{counter electrode}) \rightarrow I^{-}$ Reduction of tri-iodide

(1.5)

$S^{+}| TiO_2 + e^{-}(TiO_2) \rightarrow S|TiO_2$ Recombination

(1.6)

$e^{-} (TiO_2) + I^{-}_3 \rightarrow I^{-}$ Back reaction (1.7)

1.4 Current status of DSSC and objectives of present thesis

Since the great discovery of the DSSC in 1990s, considerable efforts have been made over time to increase the power conversion efficiency of the device, and the best efficiency over 15% for a small size cell has been reported. It can be seen in Fig 1.5 that as a member of the third-generation photovoltaics, DSSC shows the advantages of low-cost, easy fabrication and high efficiency, which is expected to take a significant share in the fast growing photovoltaic areas[30].

The overall sunlight to electric power conversion efficiency (η) of a DSSC can be expressed as the product of the three key efficiencies: $\eta = \eta_{abs} \times \eta_{inj} \times \eta_{coll}$, where η_{abs} is the light absorption efficiency, which is the fraction of the incident photons that are absorbed by the dye. η_{inj} is the quantum yield for charge injection, which depends on the number of low lying electronic excited states below the conduction band edge of the TiO_2 and the ability of these states to undergo electron transfer with the TiO_2 in preference to other decay channel of the excited states. A good electronic coupling between the electron acceptor level of TiO_2 and the HOMO level of the dye used in the DSSC device is required for efficient electron injection into the conduction band of TiO_2. i.e. separation of electrons in CB of TiO2 and holes in the HOMO of dyes. The energetic of the charge injection step, i.e. the driving force, can be determined by considering the HOMO level of the dye relative to the conduction band of the semiconductor, i.e., TiO_2. A moderate driving force of 200mV ensures the excited state of election transfer to be rapid and in large amount. η_{coll} is the charge collection efficiency. In principle, improving at least one of these physical parameters while keeping others essentially unaffected can increase the power conversion efficiency.

Anatase nanocrystalline TiO_2 is a well known semiconductor material for DSSC photoanode. However, electron transport in nanoparticle-based photoanode relies primarily on the trap-limited diffusion process, which is an inefficient mechanism that limits the power conversion efficiency of the device[31]. One promising solution is to provide a more direct pathway for electron transport by replacing the nanoparticles with one-dimensional nanomaterials, such as nanowires, nanorod, nanotubes, nanoforest, or nanofibers [32-36]. However, these one-dimensional nanostructure photoanodes sacrifice some dye loading capacity; the performance of these photoanodes cannot compete with the photoanode made of nanoparticles. In this thesis, the mesoporous TiO_2 is replaced by electrospun TiO_2 nanofiber as the construction material for the DSSC photoanode. The one-dimensional nanostructure photoanodes have the advantage of direct electron transport. Further, the electrospun TiO_2 nanofiber would not sacrifice the dye loading capacity as the nanofibers are composed of numerous densely packed nanocrystals with size less than 10nm. Moreover, considerable efforts have been taken in the present investigation to further improve the light harvesting efficiency and charge collection efficiency based on the TiO_2 nanofiber photoanode.

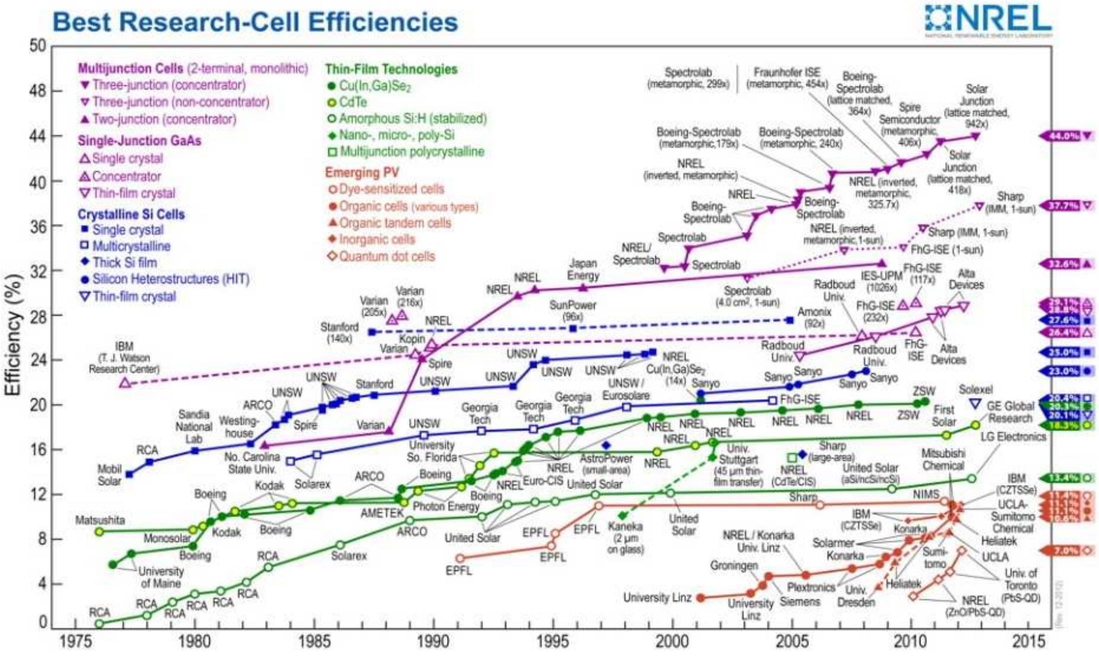

Fig 1.5 The best research-cell efficiency around the world

1.4.1 Improving light harvesting efficiency

Much effort has been devoted to enhance the light harvesting efficiency. One promising solution is to increase the surface area of the photoanode. The key breakthrough for DSSC in 1991 was utilizing mesoporous TiO_2 photoanode, which has a high surface area to absorb sufficient monolayer of dye molecules[4]. An alternative for improving light harvesting is to develop new dyes and dyes cocktail/ co-sensitized with strong and broad absorption spectrum [37-39]. Besides, another approach to improve the light harvesting efficiency is to incorporate a light scattering layer in the photoande to trap more light in the device [40-44]. Incorporating a scattering layer in the device is an easy but cost-effective method to improve light harvesting. Hore *et al* reported that by adding a reflector layer on the photoanode, the power conversion efficiency of DSSC has been improved from 3.8% to 6.8%[43]. In this thesis, two methods have been proposed to improve the light harvesting efficiency. In chapter 4, two types of novel scattering layers are introduced in the photoanode to improve the light harvesting efficiency via extending light path in the device. In chapter 5, a novel design of a core-shell photoanode is presented where a thin-shell of infrared dye, copper phthalocyanine (CuPc), is deposited on the core composed of N719 sensitized TiO_2 nanofiber. In addition to broadening the absorption spectrum on solar energy, this core-shell configuration photoanode further suppresses the recombination process.

1.4.2 Improving charge collection efficiency

Fast recombination and/or slow charge carrier diffusion result in lower charge injection and collection efficiency. Various methods have been carried out to effectively transfer electrons in the conduction band of TiO_2 in preference to other decay channels, for example modified surface of TiO_2 with insulating oxides or using high band-gap semiconductors, post-treatment with aqueous $TiCl_4$ solution[45-47]. Recently, another effective approach is to incorporate carbon-based materials, such as carbon nanotube, graphite in the photoanode to provide an effective, dedicated highway for electron transport and collection. Dang *et al* using single-walled carbon nanotube (SWCNT) -TiO_2 as photoanode improved the electron collection efficiency (η_{coll}), and the power efficiency has reached 10.6%[48]. Jang *et al* embeded the gaphitic thin film into TiO_2 nanoparticle photoanode to improve the electronic conductivity of the photoanode and extend the electron lifetime[49]. In chapter 6, the multiwall carbon nanotube (MWCNT) is incorporated into the one-dimensional TiO_2 nanorod to enhance the charge transport and collection efficiency. This approach can effectively collect and transport photogenerated electrons and reduce the recombination thereby improving the efficiency of the device.

Chapter 2

Experimental Methods

After introducing the background and working principle of the DSSC in the previous chapter, the basic materials and the test techniques as used in this study are presented and discussed in this chapter. The morphology and crystal structure characterization methods, such as SEM, TEM, XRD are described. Moreover, details on the set-up and theories of spectroscopic methods, such as photovolatic current- voltage (*I*-*V*) characterization, external quantum efficiency (EQE), absorption and reflectance spectra, photoluminescence (PL), etc. are also briefly discussed in this chapter.

2.1 Materials and Reagents

The requirements of the substrate for DSSC are low sheet resistance, especially independent of temperature variation; and high transparency to the solar radiation. Typical sheet resistance of the substrate used needs to be in range of 5 to 15 ohm/sq. Both indium-doped tin oxide (ITO) and fluorine-doped tin oxide (FTO) have been used as substrate for the photovoltaic devices.

Indeed, ITO glass is the most used substrate in photovoltaic devices. However, the thermal stability of ITO glass is not ideal, which can reduce the conversion efficiency of the device. Hence, FTO glass is preferred as the substrate for DSSC application.

FTO glasses with sheet resistance of 15ohm/sq were used as the substrate for the photoanode, which were cleaned using the following procedure: sequential ultrasonic cleaning in deionized (DI) water with detergent, DI water, acetone, 2-propanol for 5 min at each step at 40^{o}C, and the acetone and 2-propanol procedures are repeated. After cleaning, the FTO glasses were dried with nitrogen and subsequently placed in an UV-Ozone chamber for 15 min. The detailed procedure can be seen in the flowchart in Fig 2.1.

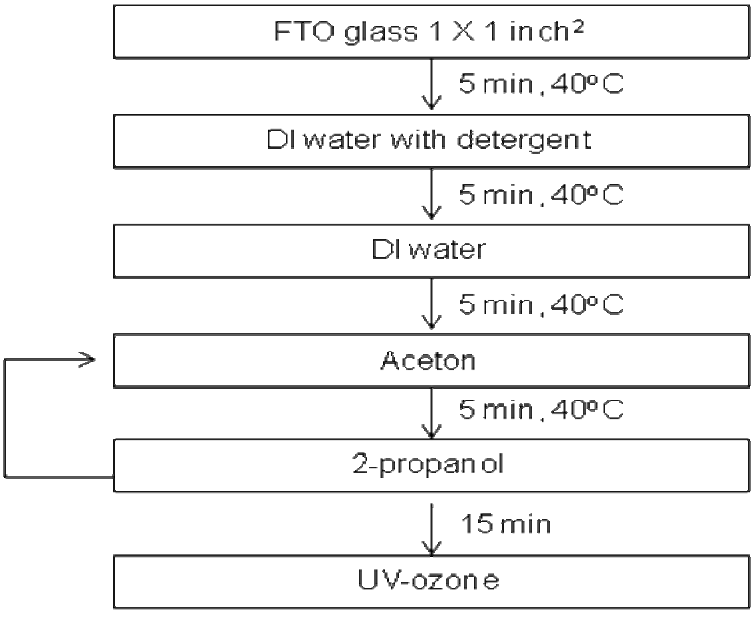

Fig 2.1 Flow chart of cleaning FTO glass

The materials used in the experiments are listed in Table 2.1.

Table 2.1 Experimental chemicals

Name		Manufactory
titanium isopropoxide	TIP	Sigma Aldrich
polyvinylpyrrolidone	PVP	Sigma Aldrich
acetic acid	HAc	Sigma Aldrich
titanium tetrachloride	$TiCl_4$	Fluka
iodine	I_2	Fluka
lithium iodine	LiI	Fluka
4-tert-butyl pyridine	TBP	Sigma Aldrich
1-methy-3-propylimidazolium iodide	PMII	Sigma Aldrich
ruthenium(II) based dye	N719	Sigma Aldrich
copper phthalocyanine	CuPc	Sigma Aldrich
multiwall carbon nanotube	MWCNT	Sigma Aldrich

2.2 Morphology and crystal structure characterization

The morphology of nanostructure photoanodes were characterized by scanning electron microscopy (SEM, JEOL Model JSM-6490) and transmission electron microscopy (TEM, JEOL 2100F). These equipments were also equipped with an energy dispersive X-ray spectroscopy (EDS) detector to carry out the X-ray analysis of elements. The crystal forms of the TiO_2 nanofiber under different calcination temperatures were investigated by X-Ray diffraction (XRD). In this work, the XRD was performed by Rigaku 9KW Smartlab using Cu kα (λ=0.1540nm) radition. The thickness of the photoanode was measured by a surface profiler (TENCOR P-10).

2.3 Spectroscopic Measurement

2.3.1 UV-visble absorption and reflectance spectra

The absorption spectrum of the test photoanodes were measured by an Agilent Varian Cary 4000UV/VIS/NIR spectrophotometer. Reflectance of the test photoanodes and different scattering-layer configurations (to be discussed later) was measured using a Cary spectrometer was equipped with an integrating sphere.

2.3.2 Photoluminescence spectrum

Photoluminescence (PL) data was measured using an Edinburgh FLSP920 spectrophotometer with an incidence-and-detection angle of 45° at room temperature. The emission spectrum was measured at an excitation using a 325-nm monochromatic filter and an increment of 1nm was adopted for data collection.

2.3.3 Raman spectrum

Raman spectroscopy is generally used in chemistry, since vibrational information is specific to the chemical bonds and symmetry of molecules. In this study, Raman spectroscopy RM3000 (Renishaw) was used to analyze multiwall carbon nanotubes (MMWCNT) in TiO_2 nanofibers.

2.3.4 XPS spectrum

X-ray photoelectron spectroscopy (XPS) is a powerful surface analysis technique, which provides elemental information about a surface as well as chemical state information [50-53]. A sample material is bombarded by mono-energetic soft X-rays, resulting in electrons being ejected. Emitted photoelectrons from the sample material are collected as a function of their energies from which binding energies can be calculated by the Einstein equation:

$$\mathbf{E_b} = h\nu - \mathbf{E_k} - \Phi \tag{2.1}$$

Where E_b is the binding energy of the electron, E_k is the kinetic energy and Φ is the work function of the spectrometer. On a finer scale it is also probable to identify the chemical state of the elements present from small variations in the determined kinetic energies.

The relative concentrations can be obtained with the sensitivity of 0.1-1% for a monolayer (around 10^{15} atoms/cm^2) from the measured photoelectron intensities. The intensity I_A of a photoelectron peak of element A is given by

$$I_A = I_{RX}\,\sigma_A\, f(E_k)\int_0^\infty C_A(Z)\exp\left(-Z/(\lambda_A \sin\alpha)\right)dz \qquad (2.2)$$

where I_{RX} is the intensity of the incident X-rays, σ_A the cross section of emission of a photoelectron from an inner core shell of A, $f(E_k)$ the detection efficiency of the spectrometer for a photoelectron with a kinetic energy E_k, C_A (z) the concentration of element A as a function of the depth z, λ_A the inelastic mean free path of a photoelectron emitted by A and α the take-off angle of the photoelectron with respect to the surface of the sample. In a homogeneous matrix, the concentration of C_A can be approximated by the relation:

$$C_A = \frac{\left(\frac{I_A}{S_A}\right)}{\sum_{i=0}^{n}\left(\frac{I_i}{S_i}\right)} \qquad (2.3)$$

where S_i is the relative atomic sensitivity factor. Typically, the XPS probes 2-20 atomic layers (3-10 nm) deep for a solid sample. The energy of the photoelectron depends on the angle (with respect to the surface) of the measurement. The escape depth z of the photoelectron depends on its inelastic mean free path length λ as well as on its emission angle α with respect to the surface. The sampling depth can therefore be varied by making use of the equation:

$$z = \lambda \sin \alpha \tag{2.4}$$

The lateral resolution of this technique is approximately 2-10 μm.

XPS measurements can provide a semi-quantitative elemental analysis of surfaces, as well as chemical state analysis for vacuum-compatible materials, which cover with a diversity of materials from biological to metallurgical samples. Due to the very small emission cross-sectional area and the corresponding long analysis times, this technique is not applicable to hydrogen and helium.

2.3.5 Electrochemical impedance spectroscopy

Electrochemical impedance spectroscopy (EIS) can be used to investigate the electron transport properties in electrochemical devices. In EIS, the potential applied to a system is disturbed by a small sine wave modulation and the resulting sinusoidal current response is recorded as a function of modulation frequency. The impedance is defined as the frequency domain ratio of the voltage to the current and is a complex value. For the resistor (R), the impedance is a real value, which is independent of the modulation frequency.

The capacitors (C) and inductors (L) both generate imaginary impedance, whose value change with frequency. The impedance spectrum of a real system, i.e., the impedance measured in a wide range of frequencies, can be described in forms of an equivalent circuit consisting of series and parallel connected elements R, C, L, and W (Warburg element which describes diffusion processes). EIS is a useful method to investigate a complete DSSC system including DSSC counter electrode and redox electrolyte [54, 55]. From measurements of EIS, the following parameters can be deduced: series resistance, charge transfer resistance of the counter electrode, diffusion resistance of the electrolyte, resistance of electron transport, and recombination in the photoanode.

In this thesis, EIS measurement was carried out with a computer assisted potentiostat (Princeton 2273). The frequency was typically in the range of 10 mHz-100 KHz and the magnitude of the modulation signal was 10 mV.

2.4 Photovoltaic characterization and analysis

2.4.1 Basics of photovoltaic

2.4.1.1The solar resource and Air Mass

The solar spectrum is a mixture of sunlight with different wavelengths λ, including ultraviolet, visible-light and the infrared regions. According to the black-body radiation, the energy density per wavelength de_λ/dλ can be described as a function of λ by Eq.2.5.

$$\frac{de_\gamma(\lambda)}{d\lambda} = \frac{2hc_0 d\Omega}{\lambda^5} \frac{1}{\exp\left({hc_0}/{\lambda k_B T} - 1\right)} \qquad (2.5)$$

where dΩ is solid angle element, C_0 is the velocity of light in vacuum, k_B is the Boltzmann constant, and h is the Planck constant, respectively. When taking $d^2e_\gamma/d\lambda^2=0$, the maximum value of $de_\gamma/d\lambda$ is at a wavelength

$$\lambda_{max} = \frac{hc_0}{4.965k_BT} = 0.2497\frac{\mu meV}{k_BT} \qquad (2.6)$$

The power density at the sun's surface is 62 MW m^{-2} and it attenuates to 1353 W m^{-2} at the point just outside the Earth's atmosphere since the solid angle subtended by the sun, Ω_S, is as small as 6.8×10^{-5} sr. Once passing through the atmosphere, the spectrum is partially reduced by the absorption of O_2, O_3 in the ultraviolet region; and water vapor, CO_2, and methane in the infrared region. The attenuation is described by the "Air Mass" factor since the absorption increases with the mass of air through which the radiation passes. For a thickness of l_0 of the atmosphere, the path length l through the atmosphere for radiation at an incident angle α relative to the normal to the earth's surface is described by

$$l = \frac{l_0}{\cos\alpha} \qquad (2.7)$$

The Air Mass factor is the ratio of l/l_0. The spectrum outside the atmosphere is expressed as AM0 and that on the surface of the earth for perpendicular incidence as AM1. The standard spectrum for moderate weather is AM1.5 which means a solar incident angle of 48^o relative to the surface normal and gives an average irradiance of 1,000 W m^{-2}. Fig 2.2 shows the comparison between the spectrum of a 5900 ^oK black body and those of AM0 and AM1.5. The actual irradiation changes with position of the sun, climates, seasons, and time. Averaging over a year, the global average energy current density changes from less than 100 Wm^{-2} at high latitude areas to approximately 300 Wm^{-2} in Saudi Arabia. It is slightly more than 100 Wm^{-2} in central Europe, where the amount of energy incident to a normal surface in a year is about 1000 $kWhm^{-2}$ and is also known as 1000 sun-hours per year.

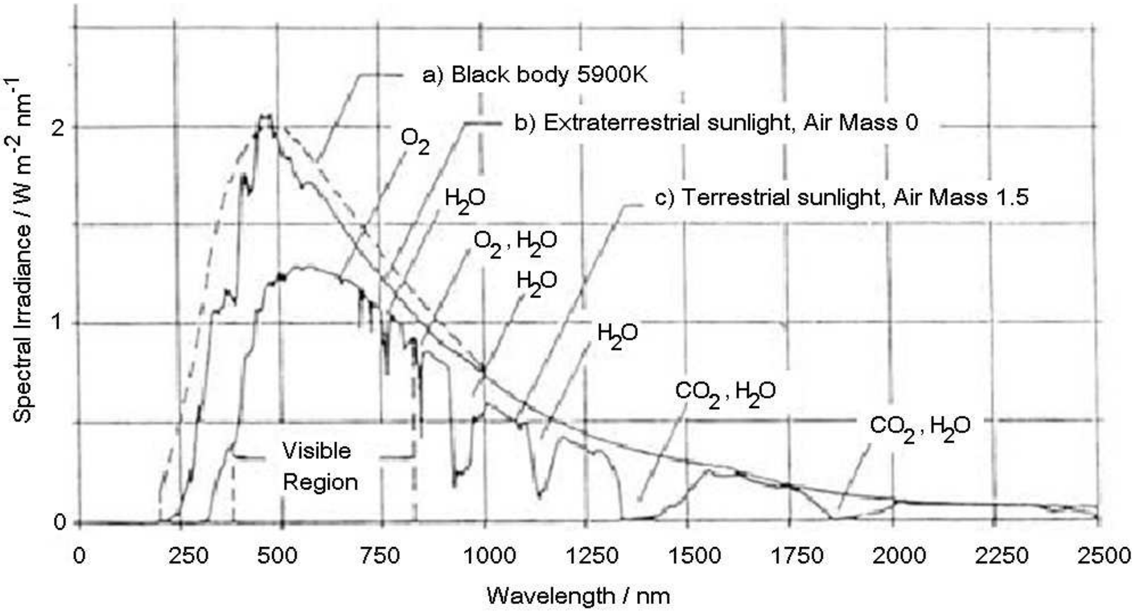

Fig 2.2 Spectra of a) Black body 5900K (attenuated by a factor of 6×10^5 in intensity), b) AM0 and c) AM1.5

2.4.1.2 Photovoltaic Current- Voltage Characterization

Standard current-voltage (I-V) measurement of a DSSC determines the current voltage response of the device, i.e. I-V characteristics, in the dark and under different light intensity conditions. In the dark condition, the applied voltage, i.e. the bias, on the device generates a current that flows in the opposite direction to that of the photocurrent. This reverse current is referred as the dark current. For an ideal diode, the dark current, I_{dark}, is related to the voltage (V) by Eq. 2.8

$$I_{dark} = I_s \left(e^{qV/k_BT} - 1\right) \tag{2.8}$$

where I_s is the saturation current of the diode (typically 10^{-7}-10^{-9} A), V is the voltage applied on the terminals of the device and q is the electronic charge, 1.6 x 10^{-19} coulomb. Under illumination condition, the I-V characteristics follow:

$$\mathbf{I = I_{ph} - I_{dark} = I_{ph} - I_s\left(e^{qV/k_B T} - 1\right) = I_{ph} - I_s\left(e^{V/V_T} - 1\right)} \tag{2.9}$$

Where I_{ph} is the photocurrent that depends on the light intensity and V_T is referred to as the thermal voltage that equals k_BT/q. For non-ideal devices, an ideality factor, m, is used to modify the weak dependence of dark current on voltage.

$$\mathbf{I = I_{ph} - I_s\left(e^{V/mV_T} - 1\right)} \tag{2.10}$$

An experimental *I-V* or *J-V* (current density-voltage) curve is shown in Fig 2.3. The following parameters can be derived from the I-V/ J-V curve:

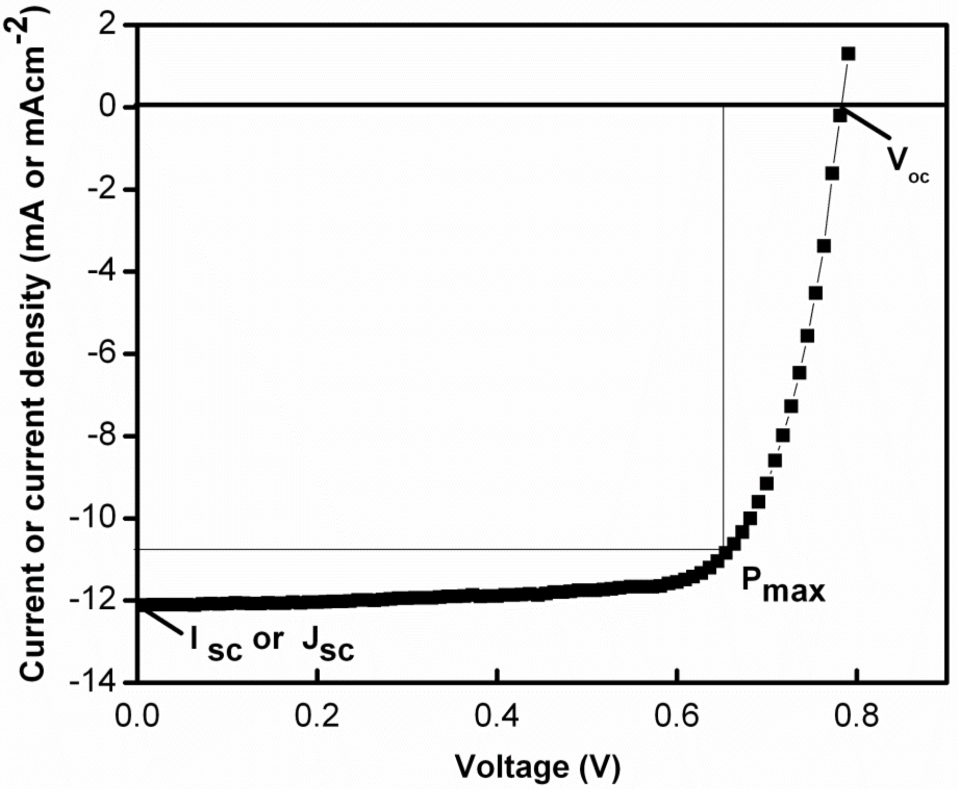

Fig 2.3 Typical I-V/ J-V curve in the experiment

In this work, the current density-voltage (I-V) characterization curves were measured by a power meter Keithley 2400 digital source meter under illumination from an AM1.5G 100 mWcm^{-2} solar simulator ABET SUN 2000 (Fig 2.4) with power density calibrated by a silicon reference cell (NIST).

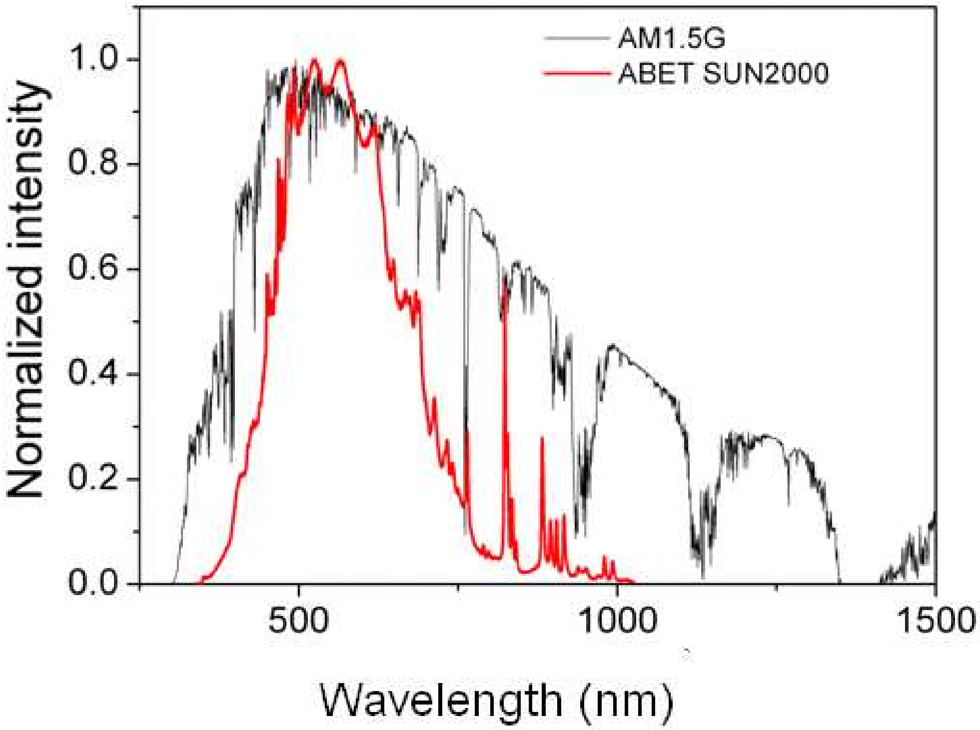

Fig 2.4 Solar simulator (ABET SUN 2000) spectrum comparing with the standard AM1.5G

Open-circuit voltage (V_{oc})

The V_{oc} is measured when there is no external load connected, i.e. under the open circuit condition. In this condition, there is no external current flow between the two terminals of the device, i.e. I = 0 and V =V_{oc}. From Eq.2.10

$$\mathbf{I} = \mathbf{I_{ph}} - \mathbf{I}_s\left(e^{V/mV_T} - 1\right) \tag{2.11}$$

$$\mathbf{V_{oc}} = \mathbf{mV_T} \ln\left[\left(\frac{\mathbf{I_{ph}}}{\mathbf{I_s}}\right] + \mathbf{1}\right) \cong \mathbf{mV_T}\,\mathbf{ln}\left[\left(\frac{\mathbf{I_{ph}}}{\mathbf{I_s}}\right]\right) \tag{2.12}$$

As seen in Eq. 2.12, V_{oc} is proportional to the thermal voltage V_T which in turn depends on the temperature, and V_{oc} also increases logarithmically with the photocurrent, I_{ph}, that depends on the light intensity.

Short-circuit current (I_{sc})

I_{sc} is measured at the condition when the applied voltage equals zero, i.e. V=0. From Eq. 2.10,

$$\mathbf{I_{sc} = I_{ph}} \tag{2.13}$$

I_{sc} increases linearly with the photocurrent and the light intensity.

Fill Factor (FF)

The power is simply the product of I and V, which geometry-wise is represented by the area of the rectangle with width V and height I in Fig. 2.3. Along the I-V curve, one can determine the maximum area corresponding also to the maximum power point, P_{max}, as labeled by the dot in Fig 2.3. At this point, the device generates the highest power output with the voltage, V_m and current, I_m. FF is defined as the ratio

$$\mathbf{FF = \frac{V_m I_m}{V_{oc} I_{sc}}} \tag{2.14}$$

Typical FF of DSSC ranges from 0.6 to 0.8 depending on the individual device and illumination intensity. It increases with decreasing light intensity. It is also affected by the series resistance, R_s, arising from the internal resistance and resistive contacts of the device, as well as parallel resistance, R_{sh}, from the leakage of the current. Fig 2.5 illustrates a simplified equivalent circuit for a DSSC system in which R_s and R_{sh} are both present. For an efficient solar cell, a small R_s but a large R_{sh} are required since a large R_s and a small R_{sh} decrease the FF dramatically.

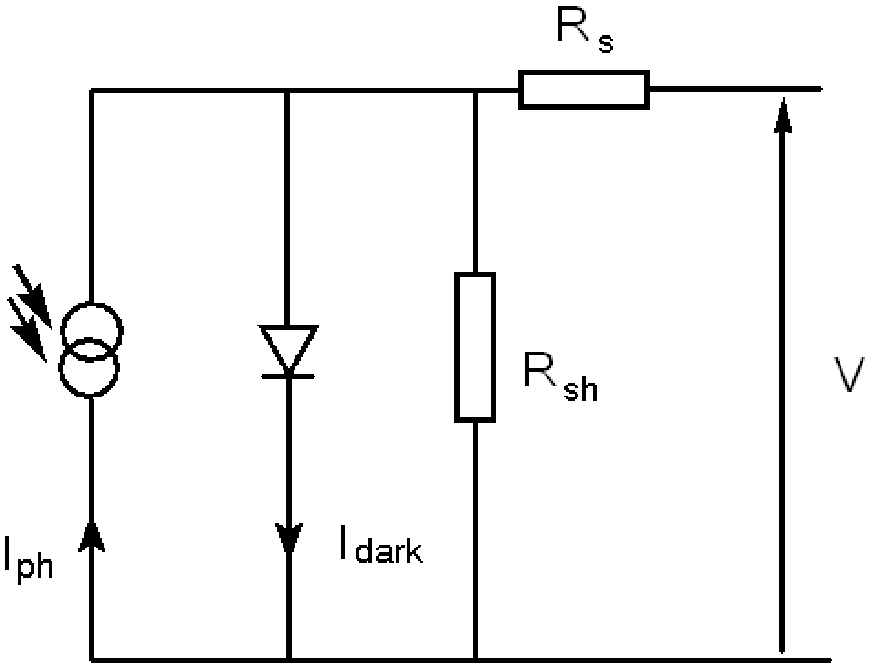

Fig 2.5 Simplified equivalent circuit for DSSC. Series and shunt resistances are taken into account.

Power conversion efficiency (PCE, η)

The power conversion efficiency, η, of the device is one of the most important parameter that is associated with the performance of the device. It is defined as the ratio of the maximum power output, P_{max}, to the power of the incident sunlight, P_{in}.

$$\eta = \frac{V_m I_m}{P_{in}} = \frac{V_{oc} I_{SC} FF}{P_{in}} \tag{2.15}$$

P_{in} is an important experimental parameter. In order to compare different results, “standard test condition” was used across the board for all the devices in this study. The standard condition includes AM 1.5 spectrum illumination with an incident power density of 100 mW cm^{-2} and a test temperature of 298 K.

2.4.1.3 External Quantum Efficiency (EQE)

External Quantum Efficiency (EQE) is the ratio of the number of charge carriers collected by the solar cell to the number of photons of a given energy (or specifically wavelength, λ) irradiated on the solar cell (incident photons).

$$\mathrm{EQE}\ (\lambda) = \frac{\text{electrons}}{\text{photons}\ (\lambda)}$$

The EQE should not be confused with internal quantum efficiency (IQE), which is the ratio of charge carriers generated by solar cells to the photons actually absorbed by the active materials after considering the reflection and absorption lost by the front electrode. Due to either EQE or IQE are dependent on both the absorption of photons and collection of charge carriers; they can be used to characterize the charge collection efficiency of photovoltaic devices.

In this study, the EQE values were measured with an EQE system equipped with a xenon lamp (Oriel 66902, 300 W), a monochrometor (Newport 66902), a Si detector (Oriel 76175_71580) and a dual-channel power meter (Newport 2931_C).

Chapter 3

Fabrication and Characterization of Dye Sensitized Solar Cell Based on TiO_2 Nanofiber Photoanode

3.1 Fabrication of TiO_2 nanofiber by electrospinning

3.1.1 Introduction

Electrospinning is one of the simplest techniques to produce the one-dimensional nanostructure materials – nanofibers. Nanofibers have been intensively researched recently due to their unique properties and intriguing applications in many areas [56, 57]. In the past several decades, electrospinning has been successfully applied to fabricate nanofibers from a broad range of organic polymers[57]. Recently, it has also been extended to generate inorganic nanofibers, such as Al_2O_3, SnO_2, and TiO2 etc. [58, 59]. Among these inorganic nanofibers, TiO_2 has attracted much interest because it can be widely used in catalytic devices, sensors, super-capacitors and dye sensitized solar cells. Preparation of TiO_2 nanofibers by electrospinning mainly involves the following key steps: (1) prepare a titanium sol-gel precursor, and then mix it with a suitable polymer to get the solution to reach an appropriate viscosity; (2)

electrospin the solution to obtain polymer/ TiO_2 composite nanofibers; (3) calcinate the composite nanofiber to remove the organic phase to yield TiO_2 nanofiber.

The physical properties of the electrospun nanofibers, such as the fiber shape, diameter, and uniformity are often influenced by the solution properties and processing parameters, such as viscosity, surface tension, applied electric field strength, and flight time of fiber from the positive electrode to ground, etc[60]. In this chapter, we investigate the effect of some processing parameters on the formation and morphology of electrospun TiO_2 nanofibers, including: (1) the solution property: viscosity of solution; (2) the equipment parameters: the applied voltage and the distance between electrode and collector which control the time of flight; and (3) post heat treatment: calcination temperature.

3.1.2 Fabrication and characterization of electrospun TiO_2 nanofiber

TiO_2 nanofibers were prepared by combining sol-gel and electrospinning techniques. The sol-gel precursor for electrospinning was made from polyvinylpyrrolidone (PVP), titanium isopropoxide (TIP), acetic acid and ethanol. In this work, the nozzle-less electrospinning setup is adopted instead of the traditional syringe approach.

Traditional electrospinning setup consists of a high voltage power supplied spinneret, a syringe pump and a grounded collector plate (Fig.2.1 a), which has been described in the literatures. In our tests, a novel nozzle-less electrospinning setup (Nanospider) was used as schematically represented in (Fig.2.1 b). A simple rotary electrode substitutes for the spinneret and syringe pump. The rotating electrode, half submerged in a bath of solution, carries the solution in form of a thin layer or film. The film is highly charged as it is in contact with the rotating electrode and is exposed to a strong electric field formed between the positive rotary electrode and the ground collector. When the voltage is sufficiently large and the film sufficiently thin, the charged film becomes unstable in the intense electric field with a numerous electrospinning jets generated over the electrode surface. As the jets carrying the fiber “fly” over to the ground collector, the neighboring positive charges deposited on the fiber repel against each other thus stretching the fiber to an even thinner diameter during its flight to the ground collector. This process continues until the fiber diameter gets smaller to tens and hundreds of nanometers depending on the distance between the rotating electrode and ground collector as well as the applied voltage. Comparing with conventional single-nozzle or multi-nozzles electrospinning with the spinning heads distributed artificially, the main advantages of nozzle-less electrospinning is that the numbers of jets are much greater and the locations of the jets are set up naturally in their optimal positions. This translates to advantages of producing better uniformity in the nanofiber web, fast production (at least 10 times faster), and easy-to-clean process.

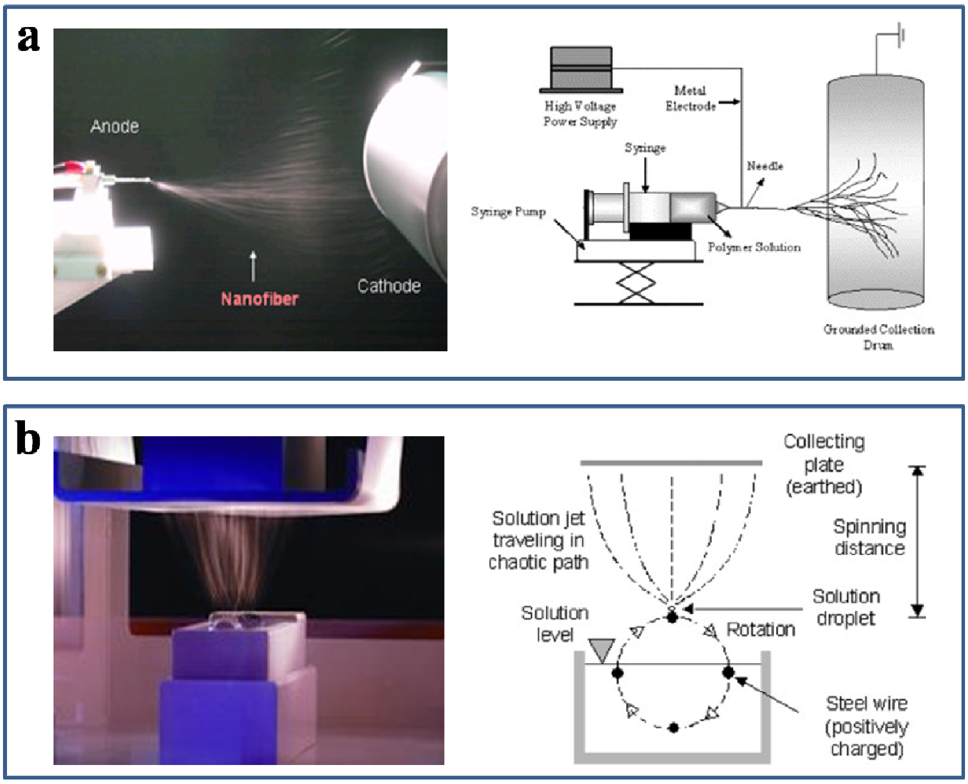

Fig.3.1 Schematic setup for electrospinning: a traditional electrospinning setup, b nozzle -less electrospinning setup

First, we added TIP to an alcohol solution containing PVP as precursor. Acetic acid was also added to stabilize the solution and control the hydrolysis reaction of the sol-gel precursor. The prepared precursor was subsequently placed in the feed trough of the nozzle-less electrospinning device. An electric potential of 70kV was applied to the rotating electrode, which was spaced 19 cm from the stationary collector. Then TiO_2/PVP composite fibers were fabricated by electrospinning process. The resulting composite fibers were left exposed to air with humidity/moisture for about 5 hours to allow complete hydrolysis before sending the sample to calcination. TiO_2 nanofibers were obtained after calcinating the samples at 450°C for 2 hours.

In order to investigate the effect parameters on morphology of TiO_2 nanofibers, different molecular weight (M_w =10,000, 360,000, and 1,300,000 g mol^{-1}) PVP and precursor compositions were studied. Details of the precursor composition for electrospun in our experiment are shown in Table 3.1.

Table 3.1 Solution composition for electrospun

Samples	M_w of PVP /$gmol^{-1}$	Concentration of PVP (%)	Concentration of TIP(%)
1-1	10,000	2.5	6.7
1-2		3.5	6.7
1-3		5	5
1-4		5	10
2-1	360,000	2.5	6.7
2-2		3.5	6.7
2-3		5	5
2-4		5	10
3-1		2.5	6.7

3-2	1,300,000	3.5	6.7
3-3		5	5
3-4		5	10

To investigate the effect of calcination temperature on TiO_2 phase, the TiO_2/PVP composite nanofibers were calcinated at 450 ^{o}C, 550 ^{o}C and 650 ^{o}C respectively, for 2 hours.

Figs. 3.2 to 3.4 show the images from the Scanning Electron Microscopy (SEM) on the different morphologies of TiO_2 morphology prepared using different molecular weight of PVP. The molecular weight of polymer affects the formation and morphology of the electrospun nanofibers. Fig 3.2 shows SEM images of electrospun TiO_2 with lower molecular weight (LM_w, M_w =10,000 gmol^{-1}) of PVP at different solution composition. Instead of getting nanofibers (with fibrous morphology), both micro-network and nanoparticles were obtained in the tests. It reveals that non-fibrous structure can be fabricated using the LM_w of PVP. Fig 3.3 and 3.4 are respectively SEM images of electrospun TiO_2 with middle (MM_w, M_w =360,000 gmol^{-1}) and higher molecular weight (HM_w, M_w =1,300,000 gmol^{-1}) of PVP. Unlike the previous case with LM_w PVP, morphology of nanofibers has been obtained when using these two types (MM_w and HM_w) of PVP. Based on these trials, different morphology and nanostructure of TiO_2 can be obtained by adopting appropriate

M_w of PVP.

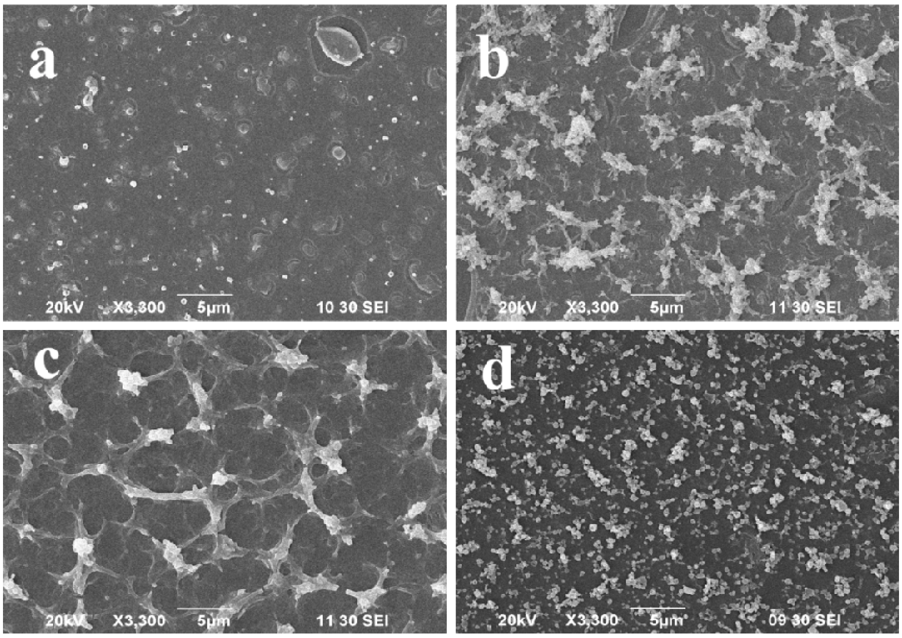

Fig.3.2 SEM imagines of electrospun TiO_2 with LM_w PVP at different solution composition: a. 2.5%PVP+6.7%TIP, b. 3.5%PVP+6.7%TIP, c. 5%PVP+ 5%TIP, d.5%PVP+10%TIP

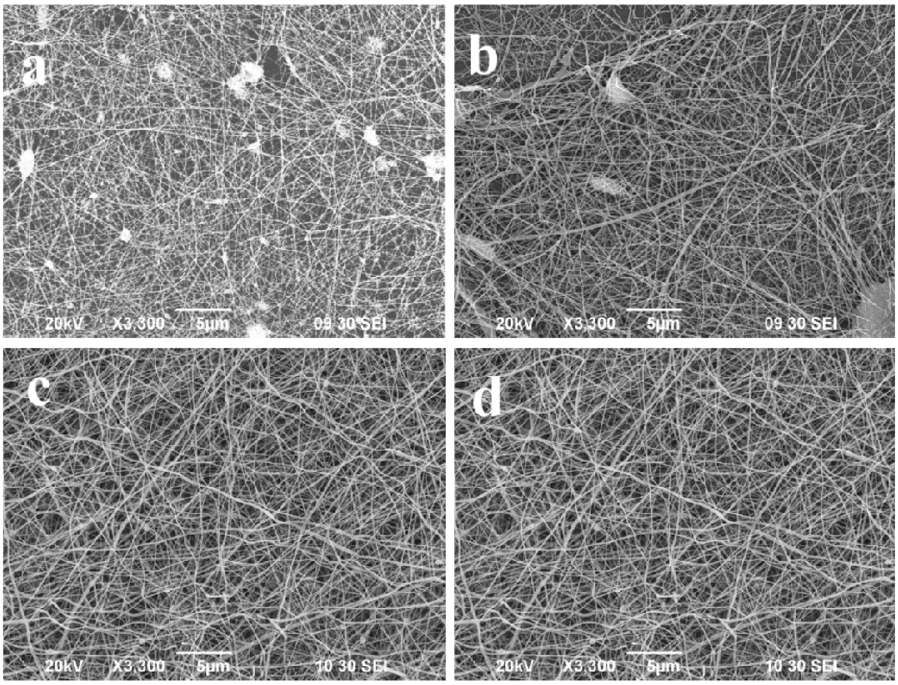

Fig 3.3 SEM imagines of electrospun TiO_2 with MM_w PVP at different solution composition: a. 2.5%PVP+6.7%TIP, b. 3.5%PVP+6.7%TIP, c. 5%PVP+ 5%TIP, d. 5%PVP+10%TIP

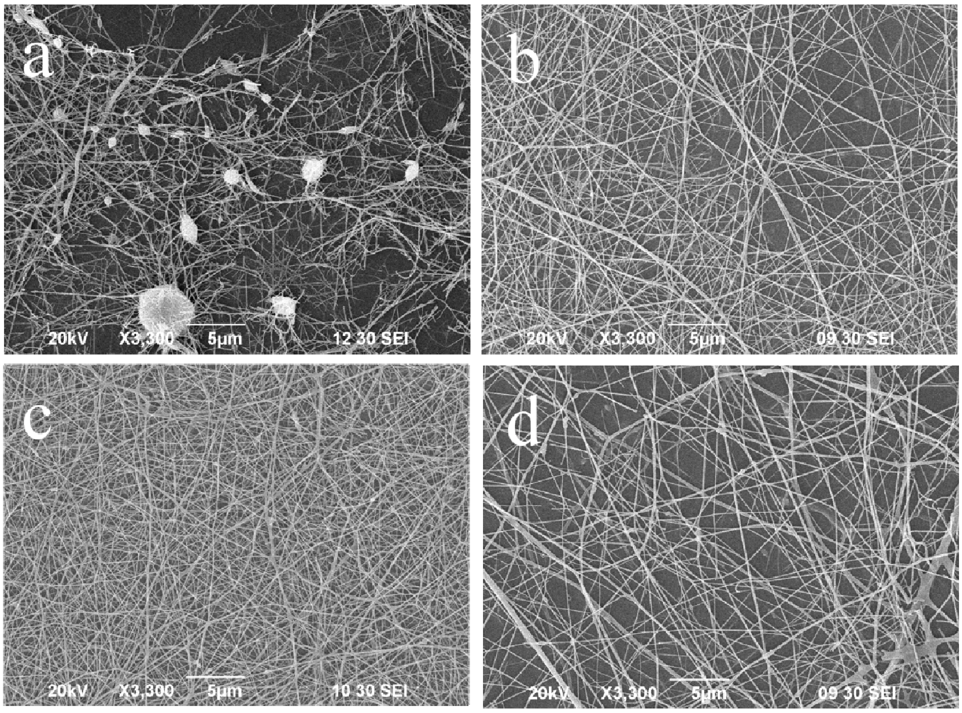

Fig 3.4 SEM imagines of electrospun TiO_2 with HM_w PVP at different solution composition: a. 2.5%PVP+6.7%TIP, b.3.5%PVP+6.7%TIP, c. 5%PVP+ 5%TIP, d.5%PVP+10%TIP

The molecular weight of the polymer used in the precursor step affects the viscosity of the solution and subsequently affects the morphology of electrospun nanostructure[61]. According to Huggins (Eq.3.1) and Mark-Houwink-Sakurada (Eq.3.2) equation[62, 63]

$$\eta_{sp}(c) = \eta c + k_H(\eta c)^2 + \cdots \tag{3.1}$$

$$\eta = KM^a \tag{3.2}$$

$\eta_{sp}(c)$ is the specific viscosity, η is the intrinsic viscosity, c is the polymer concentration, K_H is the Huggins coefficient, M is the molecular weight of the polymer, K and a are two constants, both of which depend on temperature and solvent. Therefore, the molecular weight and concentration of the polymer are major parameters affecting viscosity of the solution. There is a minimal required viscosity on the solution for electrospinning, below which electrospinning is not possible. Unfortunately, the viscosity of the solution using lower LM_w PVP has not reached that minimal requirement for electrospinning nanofibers (Fig.3.2). On the other hand, increasing M_w of PVP increases the viscosity of the solution, which favors formation of nanofibers (Fig 3.3 and 3.4).

According to Huggins Equation (Eq.3.1), concentration of the polymer also affects the viscosity of the solution, which in turn affects the morphology of the nanofibers. Fig 3.3 shows the SEM images of electrospun TiO_2 with MM_w PVP from the concentration of 2.5% to 5%. Beads formed when the PVP concentration was relatively low (2.5%). As PVP concentration increased (3.5%), beads became larger and the shape changed from spherical to spindle-like. When the PVP concentration increased to an appropriate concentration, beads disappeared. Fig 3.4 follows the same behavior.

Formation of beads could be attributed to the lower solution viscosity that cannot suppress surface tension resulting in the solution breaking up into various forms of beads and not continuous jets. In contrary, higher solution viscosity supports the jets with continuous elongation of fibers avoiding breakup of liquid jet by surface tension. Therefore, to fabricate smooth TiO_2 nanofibers, PVP concentration should be higher than 2.5% for the HM_w PVP; and higher than 3.5% for the MM_w PVP. On the other hand, too high in viscosity “gels” up the solution and prevents instability of the liquid film carried by the exposed rotating electrode. This undesirable situation also deters formation of nanofibers.

Table 3.2 shows the average diameter of TiO_2 nanofibers obtained with different solution composition. The diameter of electrospun TiO_2 nanofibers obtained ranged from 60 to 120nm with both MM_w and HM_w PVP. The diameter of TiO_2 nanofibers increased with increasing PVP, or TIP concentration, while the concentration of TIP has greater effect on TiO_2 nanofibers diameter. Moreover, the diameter of TiO_2 nanofibers fabricated by HM_w of PVP is slightly larger than those fabricated by MM_w PVP. Based on these observations, the diameter of TiO_2 nanofibers can be controlled easily by appropriately tuning the composition of the precursor solution.

Table 3.2 Morphology of electrospun TiO_2 with different composition of solution

M_w of PVP/ $gmol^{-1}$	Composition of solution	Morphology of TiO_2
10,000	2.5% PVP + 6.7%TIP	Film-like
	3.5% PVP + 6.7%TIP	Micro-network
	5% PVP + 5%TIP	Micro-network
	5%PVP+10% TIP	Nanoparticles with diameter about 250 nm
360,000	2.5% PVP +6.7%TIP	Nanofibers with diameter about 65 nm
	3.5% PVP +6.7%TIP	Nanofibers with diameter about 85 nm
	5% PVP + 5%TIP	Nanofibers with diameter about 61 nm
	5% PVP +10%TIP	Nanofibers with diameter about 100 nm
1,300,000	2.5% PVP +6.7%TIP	Nanofibers with diameter about 78 nm
	3.5% PVP +6.7%TIP	Nanofibers with diameter about 89 nm
	5% PVP +5%TIP	Nanofibers with diameter about 65 nm
	5%PVP +10%TIP	Nanofibers with diameter about 120 nm

Fig 3.5 shows the effect of distance between the rotary electrode and collector on the morphology of TiO_2 nanofibers. In Fig 3.5 a, the voltage applied was 70kV and the distance between the collector and the rotary electrode was 19 cm, while in Fig 3.5 b the applied voltage was 35kV and the distance was 10 cm. In both cases, the strength of electric fields was almost the same. Diameter of TiO_2 nanofibers in Figs. 3.5 a, b is, respectively, approximately 89 and 135 nm, which means the longer is the separation distance between the electrodes the

smaller is diameter of the nanofibers. Longer distance provides more time of flight for solvent to evaporate. More importantly, the positive charges deposited on the fiber (after leaving the rotating electrode) also have more time to repel against each other, thus stretching the fiber to an even smaller diameter.

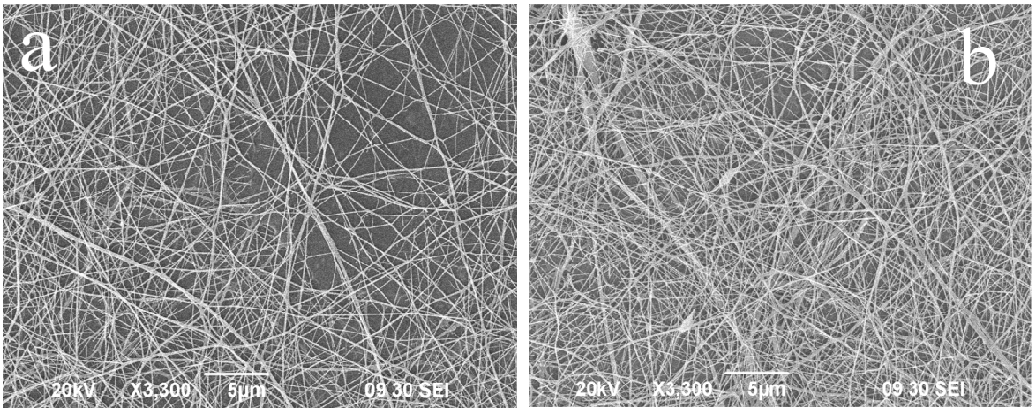

Fig 3.5 SEM imagines of electrospun TiO_2 nanofibers under different distance: a. 19 cm, b. 10 cm

Fig 3.6 is the XRD patterns of TiO_2 nanofibers, respectively, before calcination and after calcinating at different temperature: 450 ^oC, 550 ^oC and 650 ^oC. It can be seen that there is no sharp peaks appeared before calcination due to its amorphous structure. TiO_2 nanofibers showed peak of anatase when calcinated at 450 ^oC. When the calcination temperature increased to 550 ^oC, more peaks appeared and both anatase and rutile phases were observed in the pattern. As the calcinated temperature was further increased to 650 ^oC, more rutile phase can be clearly observed in the XRD pattern.

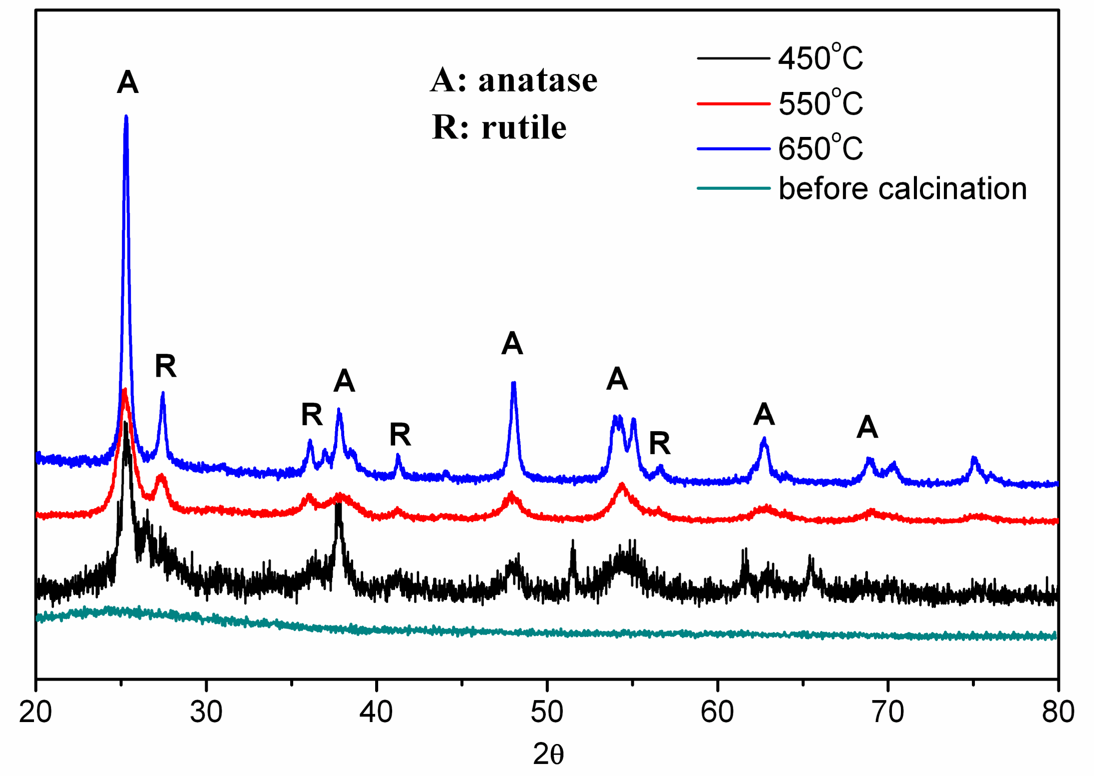

Fig 3.6 XRD pattern of TiO_2 nanofibers before calcination and at different calcination temperature: 450 °C, 550 °C and 650 °C

3.1.3 Conclusion

Different morphologies and nanostructures of TiO_2, such as nanofibers, nanoparticles and mirco-networks, can be obtained using nozzle-less electrospinning process. The molecular weight of PVP and the solution concentration have a significant effect on the morphology of the electrospun TiO_2. Electrospun solution with LM_w PVP resulted in formation of nanoparticles or micro-network due to insufficient viscosity. On the other hand, nanofibers formation was observed using MM_w and HM_w PVP. Increasing either concentration of PVP, or TIP, will increase the diameter of TiO_2 nanofibers. Moreover for each molecular weight of PVP, there is a minimum concentration needed to stabilize the fibrous structure and also a maximum concentration that the solution cannot be used for electrospinning due to excess viscosity leading to solution gel-up.

PVP/TiO_2 composite nanofiber revealed an amorphous structure and it was converted into crystalline TiO_2 phase (anatase and rutile phase) through subsequent calcination process. Anatase phase appeared after being calcined at 450° C. On the other hand, anatase and rutile mixed phases were both observed after calcined at 650° C.

3.2 Fabrication of TiO_2 nanofiber photoanode

Based on the results shown in Table 3.2, increasing the concentration of PVP, or TIP, will increase the diameter of TiO_2 nanofiber. The smaller is the diameter, the higher is the surface area, therefore, TiO_2 nanofiber with smaller diameter is adopted to fabricate DSSC device in order to adsorb sufficient dye molecules. Based on this, the composition of the precursor solution was adjusted to 4g of TIP, 3.5g of PVP with Mw of 1,300,000 $gmol^{-1}$, and 2g of acetic acid in 100mL ethanol. In following chapters, the TiO_2 nanofiber was fabricated with this optimized composition for the electrospinning precursor solution.

Fig 3.7 shows a schematic diagram of fabrication procedure for TiO_2 nanofiber photoanode. TiO_2/PVP composite nanofibers were first electrospun on FTO glass from precursor solution. The thickness of nanofiber layer was controlled by electrospinning time. TiO_2 nanofiber film was obtained after calcining at 450 °C for 2 hrs, and the film was peeled off from the FTO glass and subsequently transferred to another FTO glass pre-coated with an ultra-thin adhesive layer made of TiO_2 paste. The photoanode was obtained after calcinated again at 450 °C for 2 h. The prepared TiO_2 nanofiber photoanode was first treated with an aqueous solution of $TiCl_4$ (40mM) at 60°C for 15 min. After treatment, the film was washed with ethanol and dried in vacuum at 80 ^{o}C for a half hour, and subsequently it was immersed in a dye solution containing 0.3 mM N719 in absolute ethanol at 55°C for 24 h.

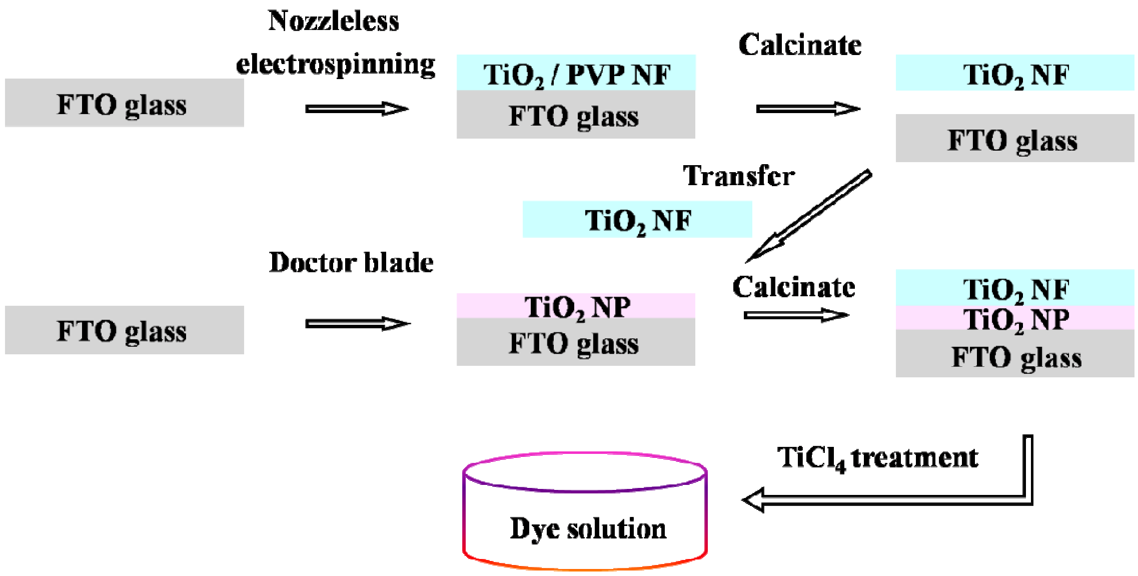

Fig 3.7 Fabrication procedure for TiO_2 nanofiber photoanode

Fig 3.8 a and b show the SEM morphology of photoanode based on electrospun TiO_2 nanofiber before-and-after sensitized with the dye N719. It is noted that the photoanodes in Fig 3.8 were treated with aqueous solution of $TiCl_4$.

It can be seen that the average diameter of electrospun TiO_2 nanofibers was about 60nm, which could be used as the suitable photoanode materials. Fig 3.8 c and d are the Transmission Electron Microscopy (TEM) and high-resolution TEM (HRTEM) images of the electrospun TiO_2 nanofiber before sensitized. The HRTEM image reveals that the TiO_2 nanofiber was composed of closely packed single crystallites with sizes less than 10 nm. It indicates that the electrospun TiO_2 nanofiber has a high surface area, which favors the adsorption of the dye molecules.

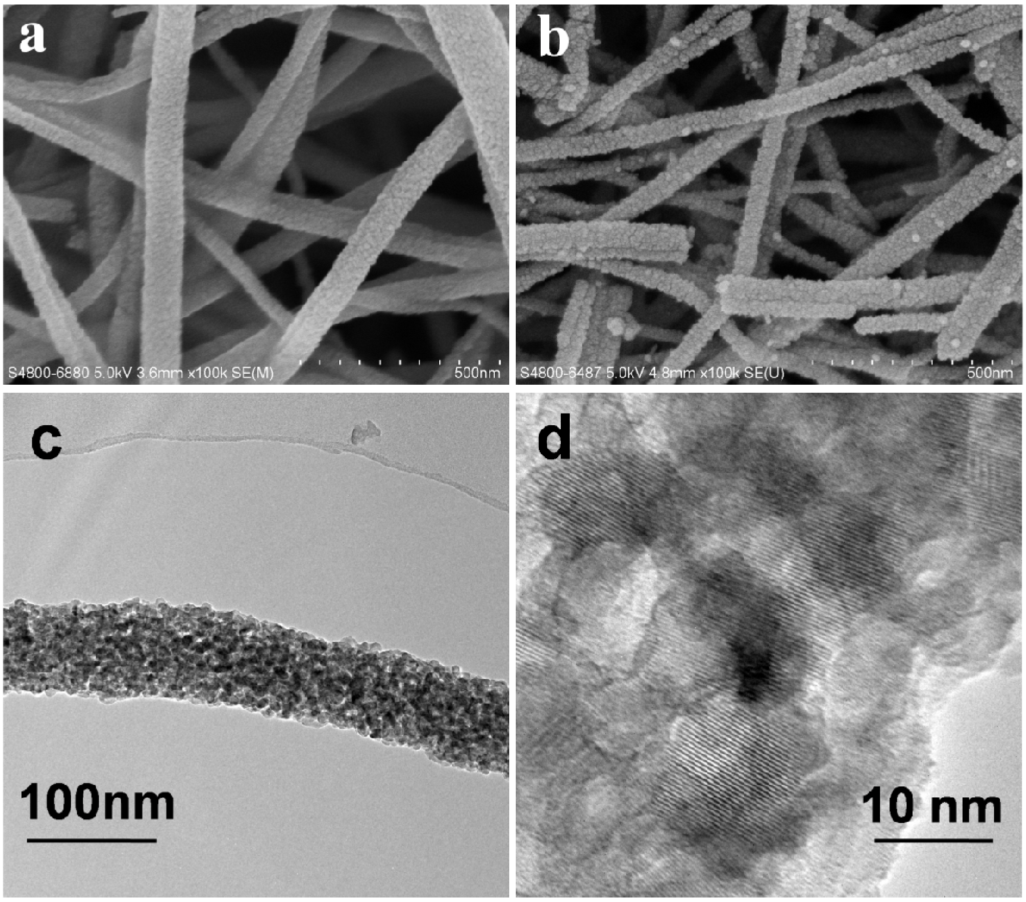

Fig 3.8 SEM and TEM images of TiO_2 nanofiber for the photoanode: a SEM image of TiO_2 nanofiber before sensitized with N719, b. SEM image of TiO_2 nanofiber after sensitized with N719, c. TEM image of TiO_2 nanofiber, d. HRTEM image of TiO_2 nanofiber

3.3 Characterization of DSSC device based on TiO_2 nanofiber photoanode

3.3.1 DSSC device assembly

The soaked photoanodes were washed with absolute ethanol to remove the “unanchored” dye molecules and subsequently they were dried in vacuum at room temperature. Platinum (Pt)-sputtered FTO glass was used as the counter electrode. The counter electrode and dye-anchored photoanode were assembled into a sandwich structure with surlyn (DuPont, 25 μm) by clip. The internal space of the device was filled with the liquid electrolyte, which was composed of 0.6 M 1-methy-3-propylimidazolium iodide (PMII), 0.05 M LiI, 0.05 M I_2, and 0.5 M 4-tert-butyl pyridine (TBP) in acetonitrile.

3.3.2 Photovoltaic properties characterization

Fig 3.9 shows the photocurrent density-voltage (J-V) curves of DSSC devices with different thickness TiO_2 nanofiber photoanode. The related photovoltaic parameters are listed in Table 3.3. From Table 3.3, it can be seen that both PCE and J_{sc} increase with increasing thickness of the photoanode, however, both of them decrease with further increase in thickness. The highest PCE and corresponding J_{sc} are achieved when the thickness of the photoanode is at 9.2 μm. This optimum is a result of the competing effects between light harvesting from the adsorbed dyes and the charge recombination in the photoanode, both of which are affected by the thickness of the photoanode. Increasing the thickness of the photoanode will increase the amount of dye absorbed in the photoanode thereby enhance the light harvesting efficiency. On the other hand, increase the thickness of the photoanode will also increase the electron diffusion length thus increase the recombination rate that lead to the reduced efficiency. Therefore, there is an optimized thickness that balances the light harvesting and charge recombination process.

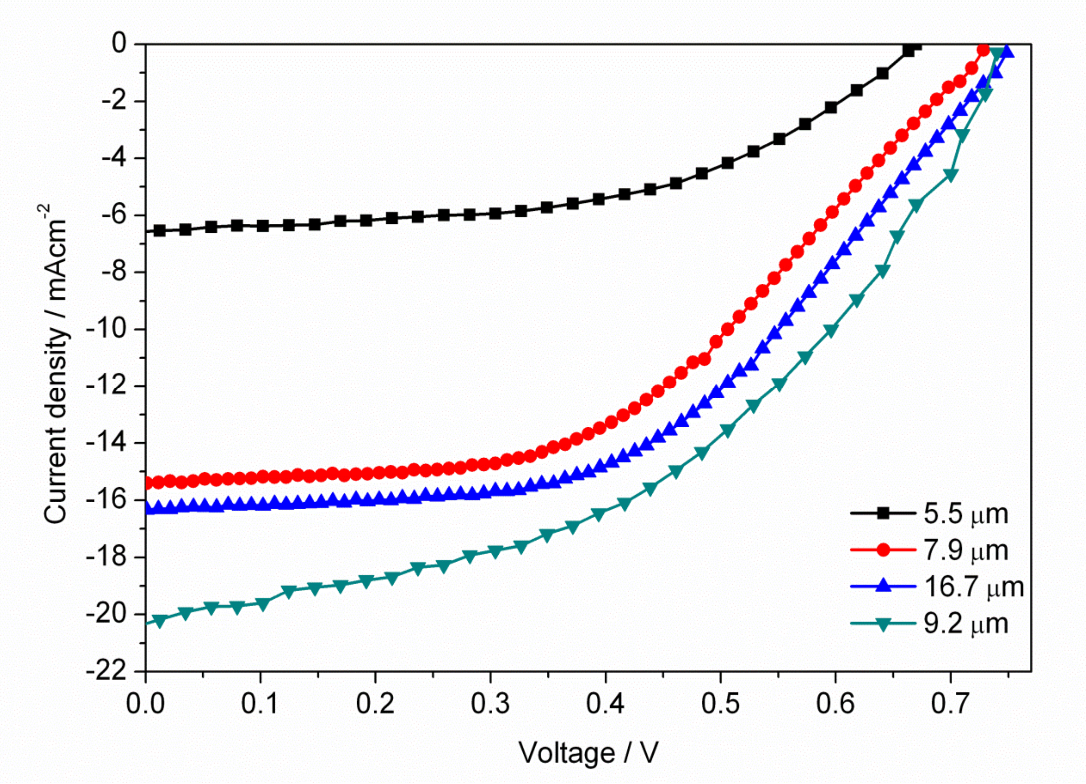

Fig 3.9 J-V curves of DSSC devices based on TiO_2 nanofiber photoanode with different thickness

Table 3.3 Photovoltaic parameters of DSSC with different thickness TiO_2 nanofiber photoanode

Thickness/ μm	Voc / V	J_{sc}/ mAcm^{-2}	FF/ %	PCE / %
5.5	0.67	6.5	52	2.50
7.9	0.73	15.4	50	5.63
9.2	0.74	20.1	48	7.14
16.7	0.74	16.3	51	6.18

Fig 3.10 is the EQE spectra of DSSC device with TiO_2 nanofiber photoanode with the optimized thickness. The peak of the EQE spectra is right at the absorption range of dye N719 (450-550nm).

Furthermore, from the J-V curves the V_{oc} and FF of all the devices were almost the same with exception of the device with 5.5μm photoanode. This indicates that the thickness of the photoanode does not affect the V_{oc} and FF of the DSSC device within a certain range of photoanode thickness (8 – 17 μm) that was considered.

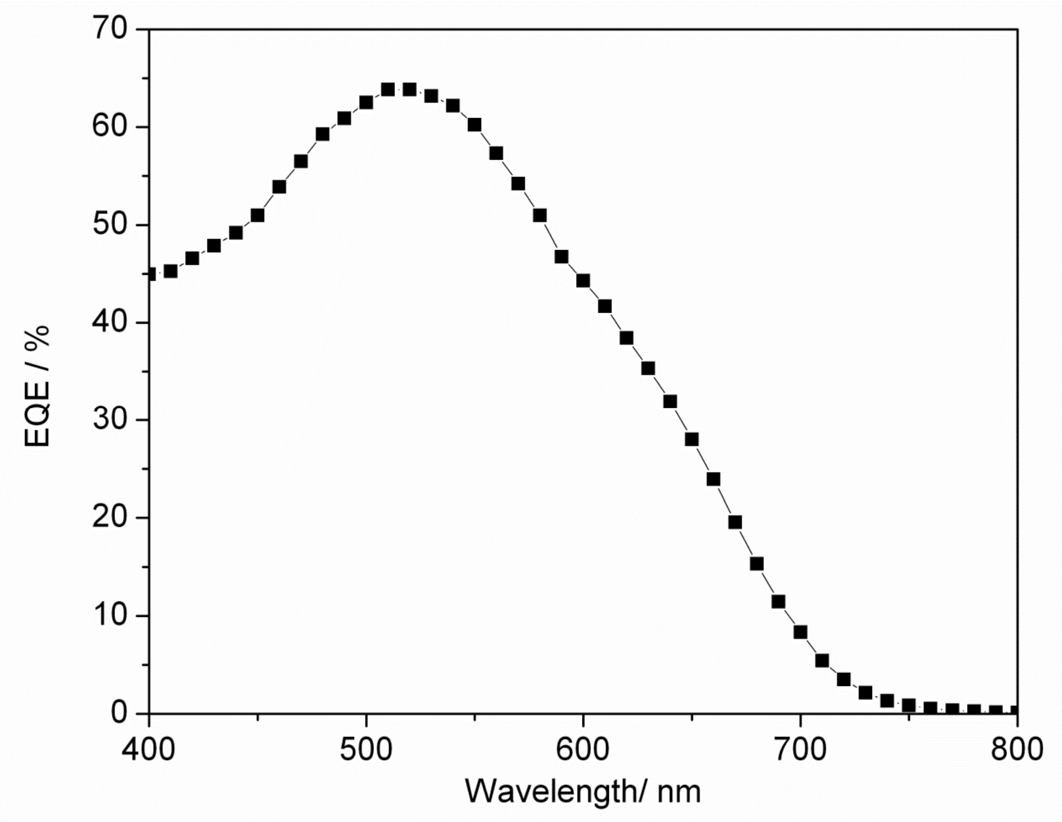

Fig 3.10 EQE spectra of DSSC device with TiO_2 nanofiber photoanode

Chapter 4

Improved Light Harvesting Efficiency in Dye Sensitized Solar Cell Based on Novel Scattering Layers

4.1 Introduction

As discussed in chapter 1, the overall sunlight-to-electric-power conversion process of a DSSC can be summarized as the combination of light harvesting efficiency, charge carriers transport and collection efficiency. Considerable efforts have been made to increase the light harvesting efficiency, such as increasing the surface area of the semiconductor to improve the dye loading ability[4]; developing new dyes, or dye mixture, with stronger absorption coefficient and broader absorption spectrum[24, 26, 39]. A different approach to improve light harvesting is to introduce a light scattering layer in the photoanode thereby extending the light path in the device. It is known that introducing the scattering layer is a simple and effective way to improve the light harvesting. Extensive research have been made to understand the scattering effect based on Mie and Lorentz theory, and the results reveal that an effective scattering layer is usually composed of large size nanoparticles greater than 100 nm[41, 43, 64]. However, this approach sacrifices the dye-loading capacity of the photoanode, thereby limiting the performance improvement of the device. Therefore, in this chapter, two types of novel scattering layers are introduced to overcome this problem with the intent to improve the light harvesting efficiency of DSSC.

4.2 A novel scattering layer composed of one-dimensional electrospun TiO_2 nanofiber

4.2.1 Fabrication and characterization of DSSC with TiO_2 nanofiber scattering layer

One promising well-practiced method to improve the PCE of DSSC is to use a one-dimensional nanostructure photoanode, such as nanofiber, nanowire or nanotube as these have excellent electron transport property to effectively transfer and collect photo-generated electrons. However, researchers pay much less attention to their optical properties, such as the light scattering effect, which is actually quite important. Application of TiO_2 nanofiber as the scattering layer in DSSC to improve the light harvesting of the device has been reported [65-67]. Another advantage in the use of nanofiber is that the nanofiber mat in the photoanode exhibits higher porosity and permeability than those of the nanoparticles. As such, electrolyte with higher viscosity can be used.

In the present study, an innovative nanofiber photoanode with scattering layer was investigated. Both smaller- and bigger-diameter TiO_2 nanofibers were incorporated in this novel photoanode. Both sizes of nanofibers were readily fabricated in a one-step process by the simple and cost-effective nozzle-less electrospinning. The new photoanode consists of two layers of TiO_2 nanofibers with different diameters: approximately 60 and 100 nm, respectively. The smaller-diameter nanofiber (SNF) layer with high surface-to-volume ratio is used to adsorb, in its maximum capacity, dye molecules and transport directly photogenerated electrons released from the excited dyes; while the bigger-diameter nanofiber (BNF) layer functions as (a) a light scattering layer to extend the light path in the device, (b) a dye absorption layer for light harvest, and (c) a medium with high porosity to facilitate electrolyte diffusion for sensitized dye regeneration in the photoanode. Therefore, the bilayer composite nanostructure photoanode can offer a combination of favorable properties for DSSC namely, dye-loading, light-harvesting, and fast electron-transport properties. With the bilayer photoanode, the performance of the DSSC device can be improved from 7.14% (i.e. photoanode without scattering layer) to 8.40% (i.e. photoanode with an optimal scattering layer), which represents a 17% increase.

Fig 4.1 shows the schematic diagram of fabrication procedure for TiO_2 nanofiber photoanode with the scattering layer. Bilayer TiO_2/PVP composite nanofiber with different diameter was first electrospun on FTO glass. The diameter of the TiO_2 nanofiber and the thickness of the layer (SNF and BNF) were controlled by the processing parameters: applied voltage, rotating electrode separation distance, and electrospinning time. For a given electrode separation distance, decreasing the applied voltage can increase the diameter of the nanofiber, and extending the electrospinning time can increase the thickness of the nanofiber layer. The TiO_2 nanofiber layer with different diameter was electrospun as described and then calcined at 450 ^{o}C[35]. Subsequently the bilayer TiO_2 nanofiber was peeled off from the FTO glass and transferred to another FTO glass with an ultrathin TiO_2 nanoparticle layer, which functions both as hole-blocking and bonding/adhesive layer. The new composite photoanode was calcinated again at 450 °C for 2 hrs, pre-conditioned with an aqueous solution of $TiCl_4$, and finally sensitized with dye solution (i.e. N719) to yield the bilayer photoanode for the new DSSC. It is notable that this fabrication procedure is simple, efficient and cost-effective as it is carried out in air and does not require high vacuum condition. Furthermore, the bilayer photonode was fabricated in one step avoiding adhesion issues between different layers, which can be a serious issue.

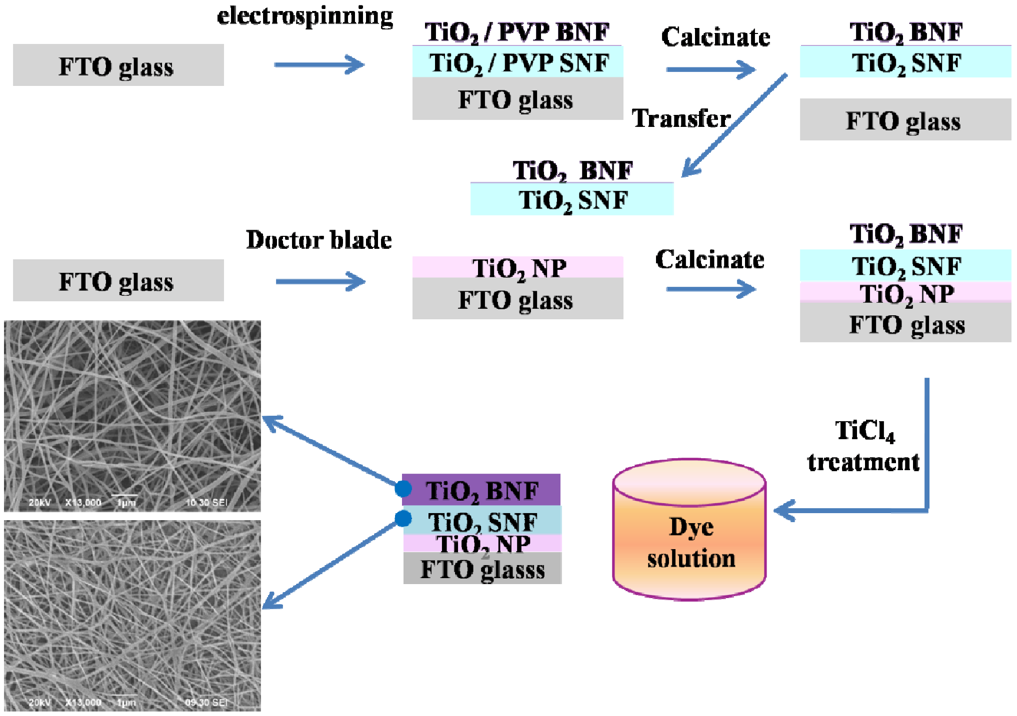

Fig 4.1. Schematic diagram of fabrication procedure and SEM images of the TiO_2 nanofibers photoanode with the scattering layer

Fig 4.1 show images of the SNF and BNF from the SEM. As can be seen, the electrospun nanofibers are randomly distributed in the layers with diameter of approximately 60 nm and 100 nm, respectively, which are confirmed by TEM images in Figs. 4.2a and 4.2c. Both TEM and HRTEM images shown respectively in Figs. 4.2b and 4.2d indicate that TiO_2 nanofiber was composed of closely packed anatase single grains with sizes less than 10 nm, which was further verified by the Selected Area Electron Diffraction (SAED) patterns (insert in Fig 4.2a). Small TiO_2 grains show large surface-to-volume ratio, which favors dye adsorption. The amount of the dye adsorbed in the TiO_2 photoanode was measured for three different configurations each with a layer thickness of 3 μm): bilayer (SNF+BNF), single layer (SNF), and the referee nanoparticles layer with particle diameter about 13 nm. Dye loading ability on the TiO_2 photoanode was quantified by desorbing the dye from the photoanode surface in 0.1M NaOH solution (water: ethanol=1:1) and subsequently the absorption spectrum of the solution was measured. The amount of dye adsorbed in these three configurations was determined to be 2.43×10^{-3}, 3.56×10^{-3} and 2.84×10^{-3} mol cm^{-3}, respectively. This results reassure that the bilayer photoanode, superficially packed with large quantities of nanoscale crystallites, have excellent dye loading capacity, which was comparable to that of the photoanode made of 13-nm nanoparticles.

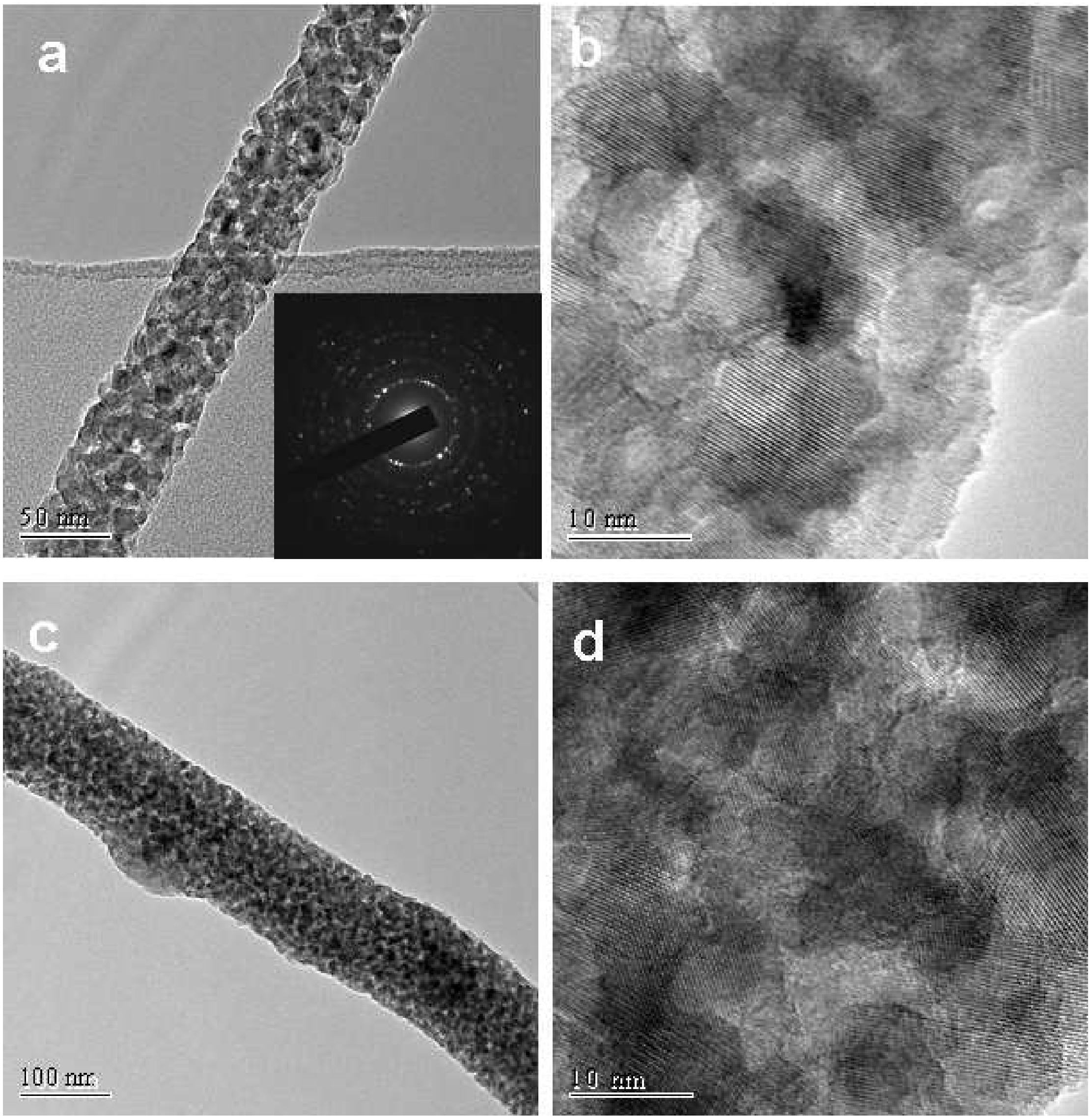

Fig 4.2 a. TEM image of SNF and corresponding SAED pattern, b. HRTEM image of SNF, c. TEM image of BNF, d. HRTEM image of BNF

Fig 4.3 shows the J-V characteristics for DSSC devices with and without the one-dimensional scattering layer photoanodes and the solar cell characteristics are summarized in Table 4.1.

Table 4. 1. Characteristics of Different DSSC Photoanode Configurations

Structure	Thickness/ μm	Voc / V	J_{sc}/ mAcm^{-2}	FF/ %	PCE / %
without sacttering layer	5.5	0.67	6.5	52	2.50
	7.9	0.73	15.4	50	5.63
	9.2	0.74	20.1	48	7.14
	16.7	0.74	16.3	51	6.18
with scattering layer	5.4	0.72	9.6	63	4.30
	7.2	0.72	14.0	65	6.78
	8.9	0.71	22.5	60	8.40
	17.6	0.73	12.6	63	5.80

The J-V curves show that the photoanode with a scattering layer DSSC has higher photocurrent density compared to the photoanode without a scattering layer. To optimize light harvesting and electron transport, the dependence of PCE and J_{sc} on thickness of the both single-layer and bilayer TiO_2 photoanode were investigated wherein the thickness of different photoanode configurations was measured by a surface profiler (TENCOR P-10). Fig 4.4 indicates that both PCE and J_{sc} increase with increased thickness of the photoanode at small thickness and ultimately decrease with further increasing in thickness. The best performance of the DSSC, as measured by highest PCE and corresponding J_{sc}, is achieved when the thickness of the bilayer photoanode is 8.9 μm. This optimum is a result of balancing the competing effects between light harvesting from the adsorbed dyes and the charge recombination in the device, both of which are affected by the thickness of the photoanode. The best PCE achieved by the bilayer photoanode DSSC is 8.40% with J_{sc} at 22.5 mAcm^{-2}, while the performance of the single-layer photoanode device with approximately the same thickness (9.2 μm) has a PCE of only 7.14% with the corresponding J_{sc} at 20.1 mAcm^{-2}. This represents an improvements of both PCE and J_{sc}, respectively, of 18% and 12%. The improved performance is primarily due to the enhancement in the J_{sc} and FF. The increased J_{sc} may be related to the enhancement of light harvesting efficiency by the BNF scattering layer in the photoanode. Comparing the transmission spectrum in Fig 4.5 and EQE spectrum in Fig 4.6 between the bilayer and single-layer of TiO_2 nanofiber photoanodes provide further supporting evidence. As shown in Fig 4.5, the scattering layer (BNF) exhibits lower transmission than that of SNF layer at the visible wavelength range (400-700nm), indicating less optical loss in the scattering layer which benefits light harvesting. The EQE spectra of the device with the photoanode incorporating the scattering layer reveals that a significant increase, as much as 17%, over the wavelength range between 450 and 550 nm. The enhancement in EQE is attributed to the light trapping effect of the BNF scattering layer.

The performance of the DSSC device with BNF photoanode was also measured (with the optimized photoanode thickness, which was ahout 9 μm). The J-V curve shown in Fig 4.7. The PCE was just about 2.36%, which is much lower than that of the device made of SNF or bilayer(BNF+SNF) photoanode.

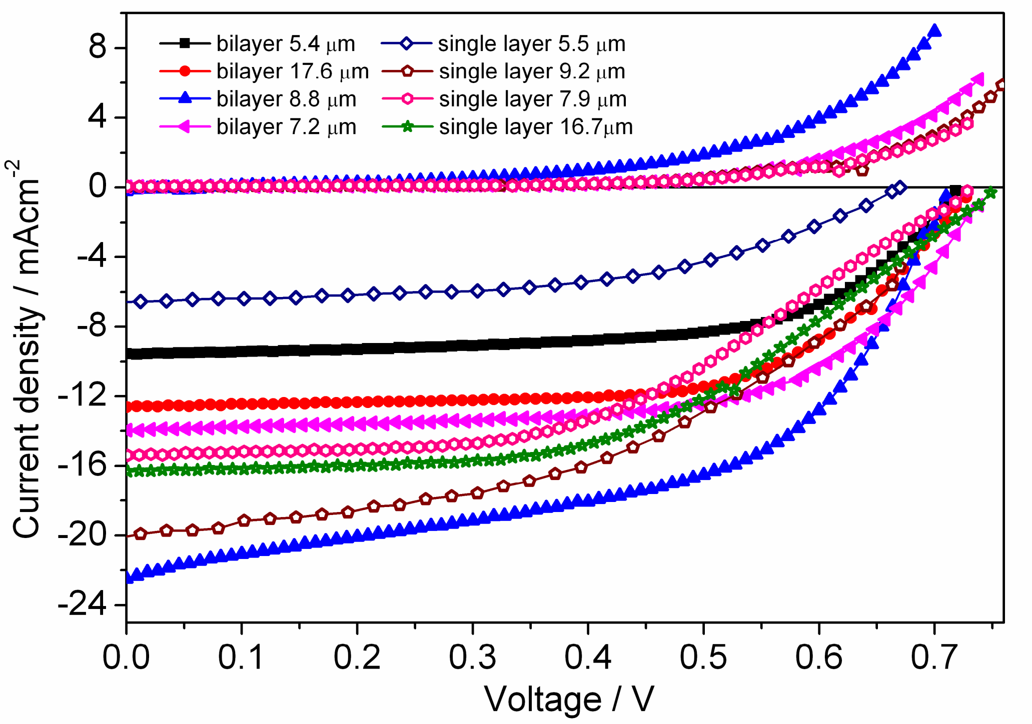

Fig 4.3 J-V curve of DSSC with and without scattering layer photoanode as function of photoanode thickness

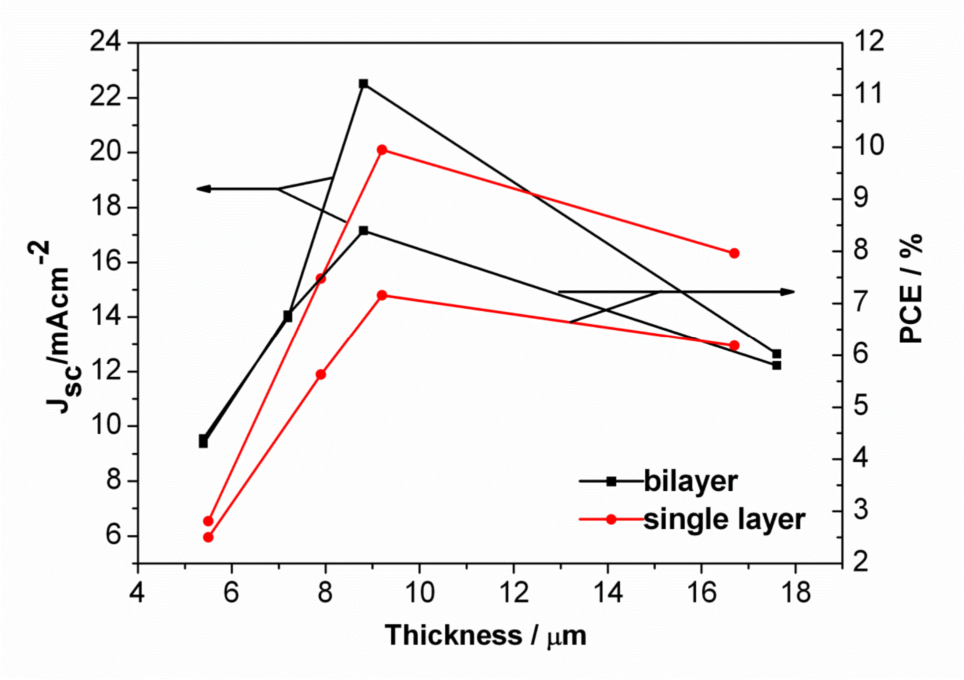

Fig 4.4 J_{sc} and PCE as function of photoanode thickness for respectively with and without scattering layer photoanode DSSC.

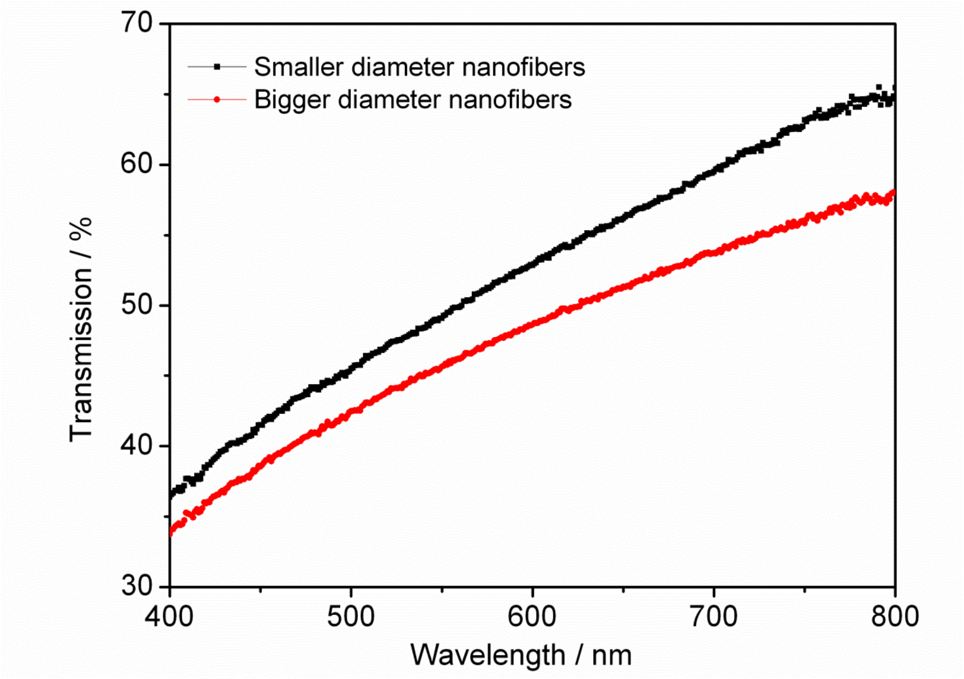

Fig 4.5 UV-Visible transmission spectra of smaller diameter nanofiber layer and bigger diameter nanofiber layer with the same thickness

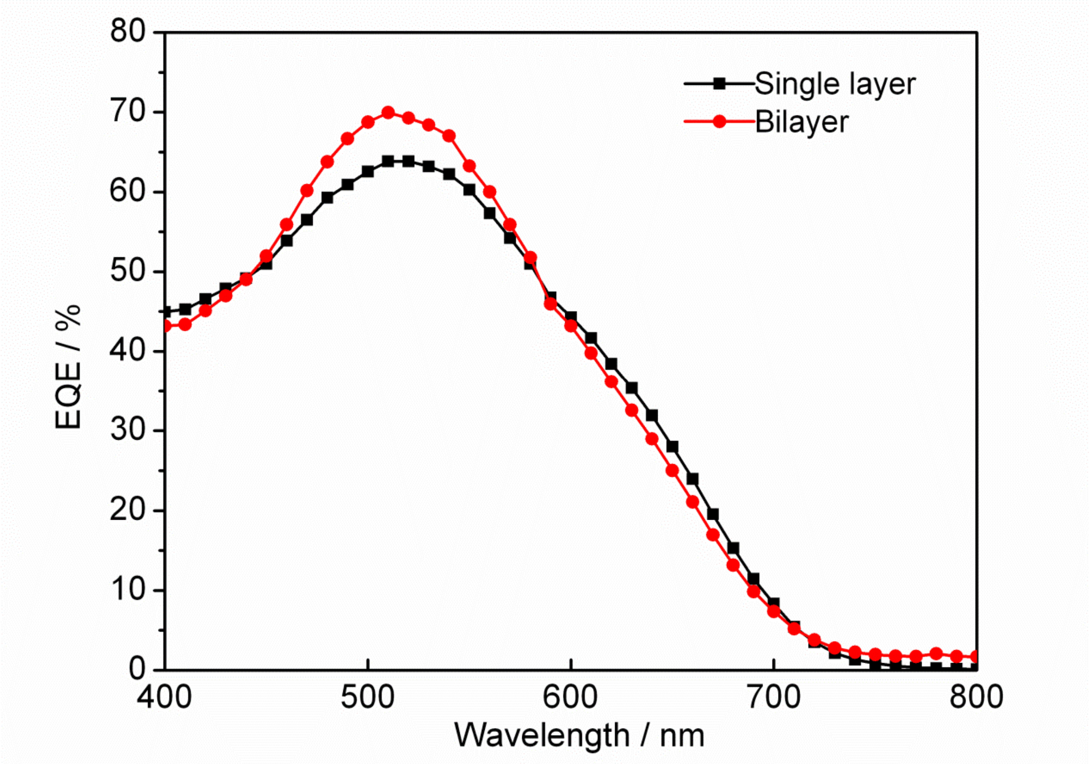

Fig 4.6 EQE spectra of single-layer and bilayer photoanode DSSC devices

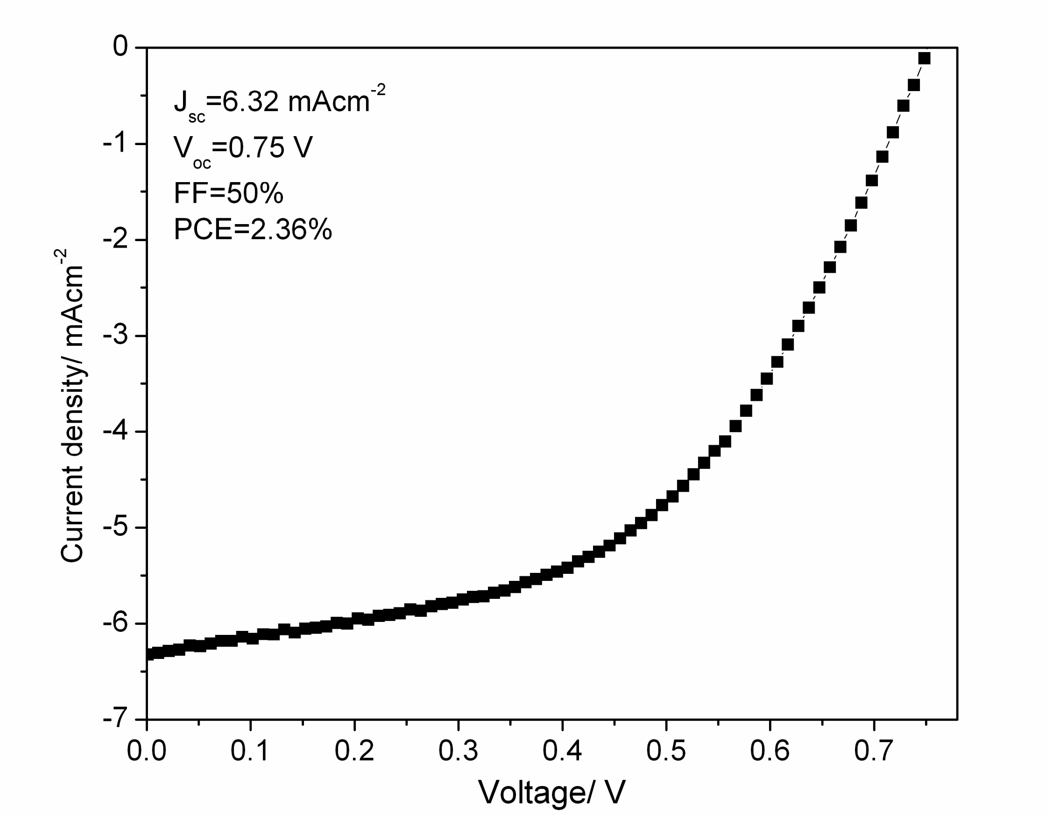

Fig 4.7 J-V curve of the DSSC device fabricated by the BNF

The enhancement of PCE of the device with TiO_2 nanofibers photoanode incorporating a scattering layer can be explained by following effects. First, the photon absorption is enhanced due to the nanofiber morphology as it is packed with highly crystalline-shaped TiO_2 grains which provide large surface area for increased dye-loading capacity for light harvesting. Second, nanofibers provide the direct pathway for transport and collection of photogenerated electrons throughout the photoanode. Third, the scattering layer adjacent to the SNF layer works as the light trapping mechanism improving the light harvesting of the device without compromising the dye loading capacity and electron transport properties.

In summary, an innovative bilayer TiO_2 nanofibers photoanode, fabricated primarily by nozzless-electrospinning technique, can significantly improve the performance of the DSSC. The transmission spectra demonstrate that the bilayer nanostructure photoanode can trap more light in the device. By optimizing the thickness of the photoanode with a scattering layer, the photocurrent density was significantly increased and the highest PCE that could be reached was 8.40%. Furthermore, the FF and thereby the conversion efficiency of our bilayer photoanode DSSC device have been improved by more than 20% as compared with the single-layer photoanode device. The nozzleless-electrospinning process was adopted to fabricate readily the required bilayer nanostructure, which can be applied to the new DSSC.

4.2.2 Optimizing TiO_2 nanofiber scattering layer for DSSC photoanode

A one-dimensional nanostructure scattering layer, composed of electrospun TiO_2 nanofibers with bigger-diameter, has been introduced in-situ on top of the photoanode made of smaller-diameter TiO_2 nanofibers to extend the light path, thereby improving the power conversion efficiency of dye sensitized solar cell. Different configurations have been investigated to achieve optimal design for the photoanode. Light trapping effect by the scattering layer was found to be related to the thickness of the photoanode. The thicker is the photoanode the weaker is the scattering effect. Furthermore, the thickness of the scattering layer in relation to the total thickness of the photoanode needs to be optimized balancing the dye-loading capacity of smaller diameter nanofibers and the light-trapping capacity of bigger diameter nanofibers.

To address this issue, a scattering layer made of approximately 100 nm diameter TiO_2 nanofiber was directly introduced on a TiO_2 nanofiber photoanode to form a bilayer structure. The effect of the scattering layer thickness in proportion to the total thickness of the bilayer photoanode on the performance of the device was systematically investigated. This is under the premise that higher efficiency can be achieved upon understanding and quantifying the competitive effects influencing performance of the device.

Incorporating a scattering layer can extend the light path in the DSSC device; unfortunately, this would also sacrifice the dye-loading capacity. Therefore, it is necessary to balance the light-scattering and dye-loading effects to obtain the optimal photoanode design. Indeed, upon systematically optimizing the dye-loading and light-trapping capacities, a high PCE of 9.28% can be ultimately achieved.

The configuration of photoanode with scattering layer can be seen in Fig 4.8 a. The bigger diameter nanofiber scattering layer was deposited in-situ on the smaller diameter nanofiber to form the photoanode. The smaller diameter nanofiber layer functioned both as dye loading and electron transport. Despite with different diameters, both TiO_2 nanofibers in the photoanode were composed of densely packed crystallized TiO_2 grains with nanoscale size that can be seen from the transmission electron microscopy (TEM) image in Fig 4.2. The ratio of scattering layer thickness to that of the photoanode can be expressed as r $\left(r = \frac{\text{thickness of scattering layer}}{\text{thickness of photoanode}}\right)$. In this work, various photoanode configurations have been fabricated with r from 1/8 to 1/4. The thickness of the scattering layer was controlled by the electrospinning time at lower applied voltage (55kV), and the relationship between thickness of electrospun TiO_2 nanofiber layers with the two different diameters and electrospinning time can be seen in Fig 4.8 b. For a given nanofiber diameter, the total thickness first increases linearly with electrospinning time and then subsequently with a diminishing return behavior. According to the relationship for the bigger diameter nanofiber as depicted in Fig 4.8 b, the photoanode with a desired scattering-layer thickness can be readily produced.

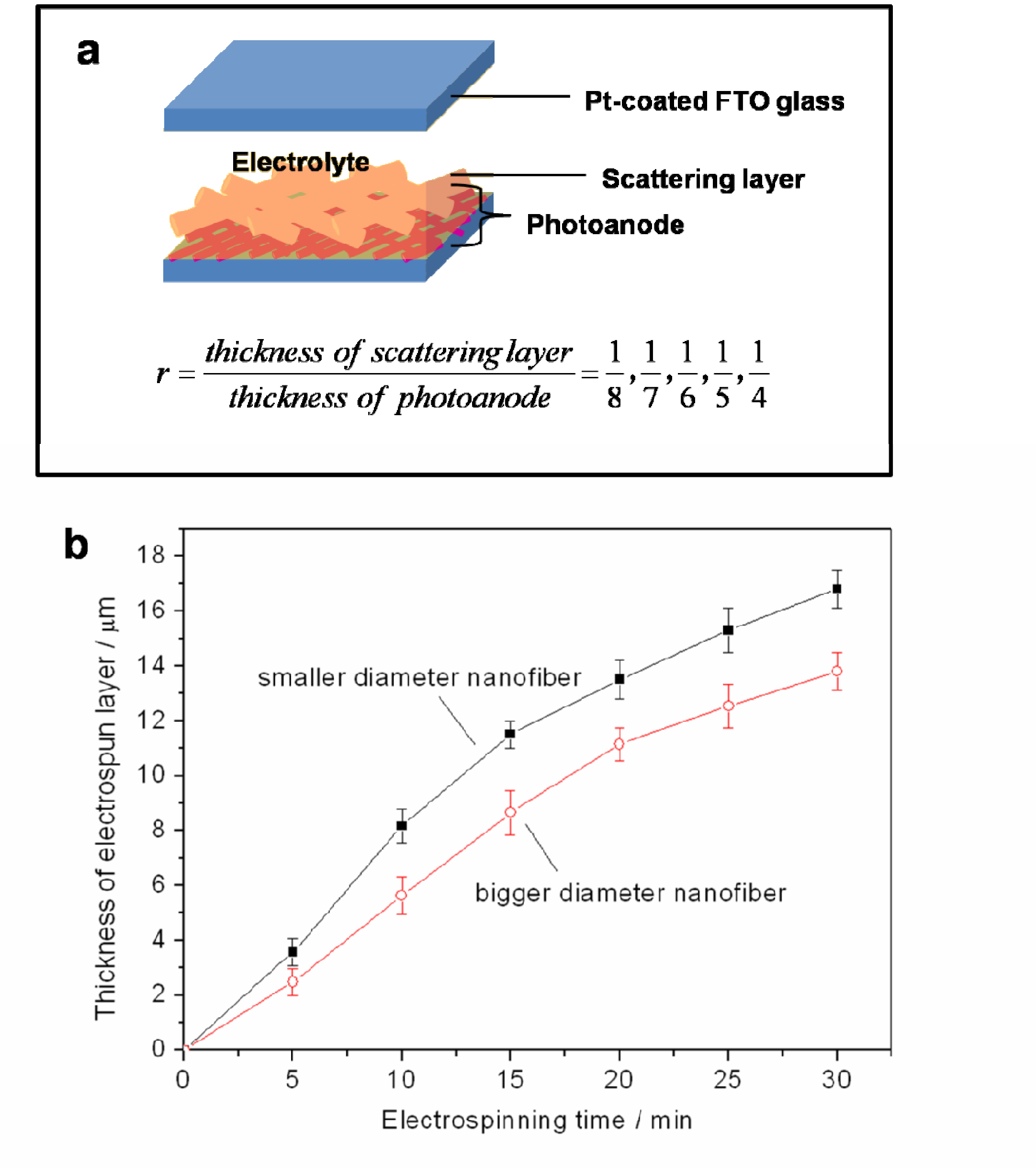

Fig 4.8 a. A schematic of the DSSC bilayer photoanode with different scattering layer ratio r; b. the relationship between electrospinning time and thickness of electrospun nanofiber with smaller and bigger diameter

The photovoltaic properties for a thin and thick photoanode, respectively, each with different ratios of the scattering layer, have been carried out in our study. The thin photoanode has a total thickness of approximately 5.5±0.2μm, while the thick photoanode has a total thickness of approximately 8.9±0.5μm. The photovoltaic properties of the referee devices without a scattering layer were also measured for comparison.

Fig. 4.9a shows the effect of the ratio of scattering layer, *r*, on the PCE for both sets of devices. The photovoltaic parameters are listed in details in Table 4.2. It is evident that the devices with thicker photoanode display higher PCE than the ones with thinner photoanode for the same ratio *r*, which suggests that the photoanode thickness is an important parameter for a DSSC. The thicker photoanode has a higher light-harvesting capability due to higher dye loading. Moreover, it can be seen from Fig. 4.9 for both sets (thin and thick photoanode) of devices that as the ratio, *r*, of the scattering layer in the photoanode increases, the PCE also increases until a maximum is achieved. Beyond the maximum, further increase in *r* results in a reduction of the PCE. Increasing the ratio of scattering layer implied increasing the thickness of the scattering layer, light path was extended hence PCE was enhanced. Yang *et al* demonstrated the same effect, increased thickness of scattering layer lead to enhanced reflectance[68]. However, increasing the ratio of scattering layer beyond a certain point results in reduction on the thickness of nanofiber with smaller diameter as the total thickness is kept constant. It is known that the smaller diameter nanofiber has larger surface area and is best used for dye loading in the photoanode. Therefore, the performance of the solar cell (i.e. PCE) can degrade when the layer thickness, which carries out the dye-loading function, is being reduced.

It is worthy to note that the thick photoanode with *r* = 1/8 exhibits even lower PCE than that of the photoanode without a scattering layer (see top curve in Fig. 4.9a at *r*=1/8). In this case, instead of improving performance of the device, introducing the scattering layer actually brings somewhat a surprisingly negative outcome. It is because for the configuration when *r* equal to 1/8, the thickness of the scattering layer was just about 1μm, in a photoanode with a total thickness of 8.7 μm, which is way too thin to function as an effective scattering layer. Furthermore, comparing with the photoanode without a scattering layer, it sacrificed the dye loading capacity resulting in poorer performance.

Fig. 4.9 b further highlights the difference in PCE as a percentage of the original with and without a scattering layer. For the devices with a thin photoanode (total thickness = 5.5 ± 0.2μm), the improvement of PCE (i.e. ΔPCE), above-and-beyond the device without scattering layer, is much higher than that of the thick photoanode devices (total thickness = 8.9 ± 0.5μm photoanode) for all values of *r*. By adding a scattering layer, the maximum performance improvement for the thin photoanode with *r* equal to 1/6 reaches 112%.

It is obvious from Fig. 4.9 b that the effect of introducing a scattering layer is much weaker for the case with a thick photoanode as the average enhancement in PCE (i.e. ΔPCE) was approximately 20%. This is because for a thicker photoanode, most of the incoming light is absorbed anyway, adding a scattering layer would increase dramatically the PCE. However, for the thin photoanode, the amount of transmitted light through a thin photoanode is not negligible, and such loss can be recovered or salvaged by the introduced scattering layer on top of the thin photoanode. Therefore, adding a scattering layer on a thinner photoanode can effectively improve the performance of the device.

Furthermore, for the thin photoanode the performance improvement (△PCE) varies strongly with the ratio of scattering layer *r*. When *r* is increased from 1/8 to 1/6, △PCE increases from 32% to 112%. However, for the thick photoanode variation of △PCE with *r* is much reduced. This suggests an optical compensation is necessary for a DSSC with a thin photoanode.

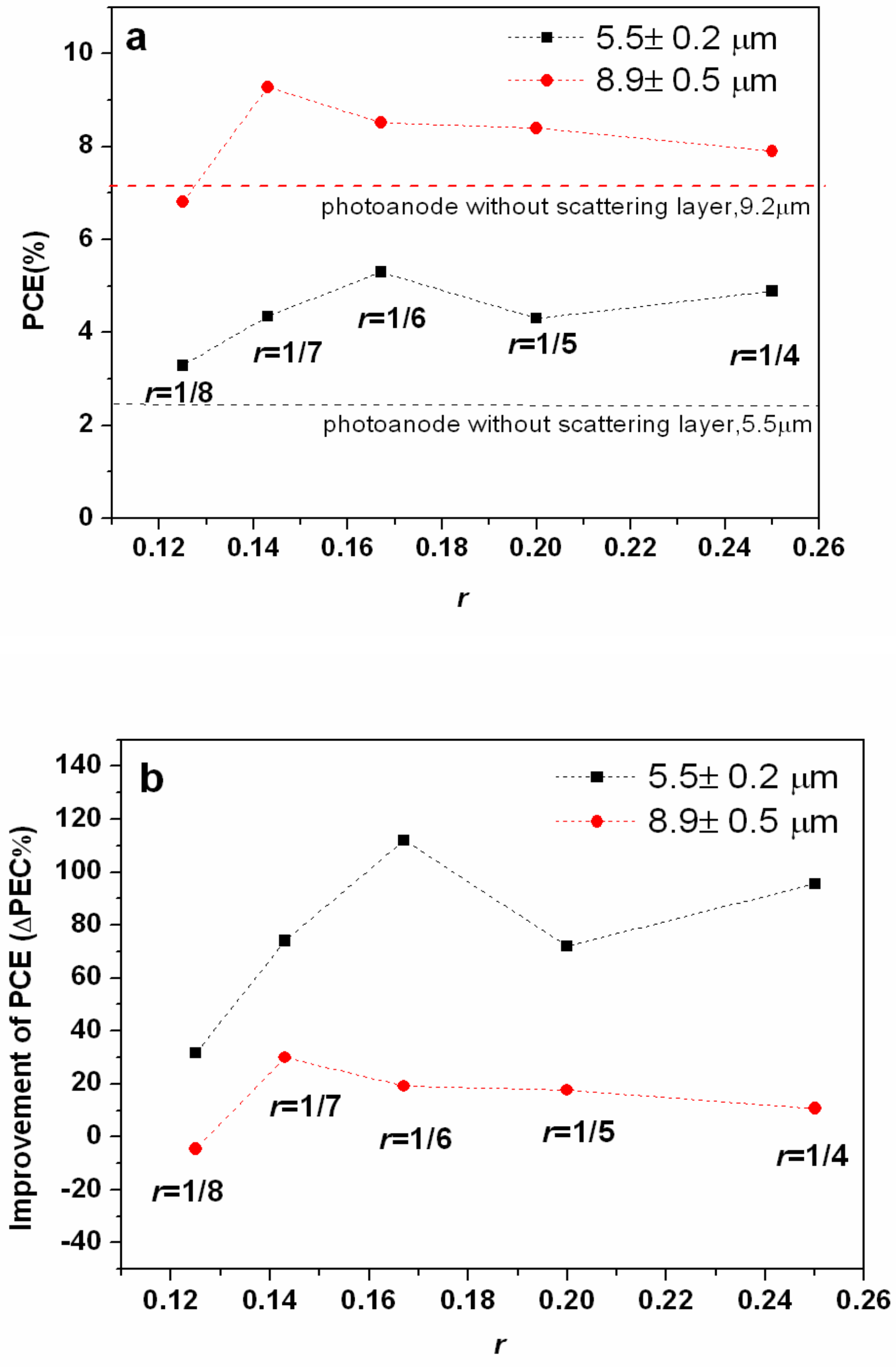

Fig.4.9 a. The effect of ratio of scattering layer on performance of both sets of devices; b. The effect of ratio of scattering layer on improvement performance (ΔPCE%) of both sets of devices compare with photoanode without scattering layer

The performance of the DSSC devices with a scattering layer together with the baseline without a scattering layer is tabulated in Table 4.2. From Table 4.2, it is found that the open-circuit voltage (V_{oc}) is almost the same (0.74 ± 0.03V) in all the configurations of photoanode devices considered, indicating that the ratio of scattering layer has insignificant effect on the V_{oc} of the device.

The short-circuit current density (J_{sc}) exhibits similar trend as with the PCE (as seen in Fig 4. 9 a). The highest J_{sc} (23.03 mAcm^{-2}) is obtained when r equals to 1/7 corresponding to the photoanode with thickness of 9.3µm. Fig 4. 10 compare the external quantum efficiency (EQE) as a function of excitation wavelength for the thicker photoanode DSSC devices with /without scattering layer. The EQE spectrum examines the light response of a photovoltaic device, which is directly related to the J_{sc}. From Fig 4. 10, it can be seen that the highest EQE value obtained is when r =1/7. Introding the scattering layer in the photoanodes (r=1/7-1/4) produce higher EQE values than the single layer photoanode device due to the light trapping effect, while for the device with r equal to 1/8, the EQE value is lower than that without scattering layer, which is consistent with the result of J_{sc}.

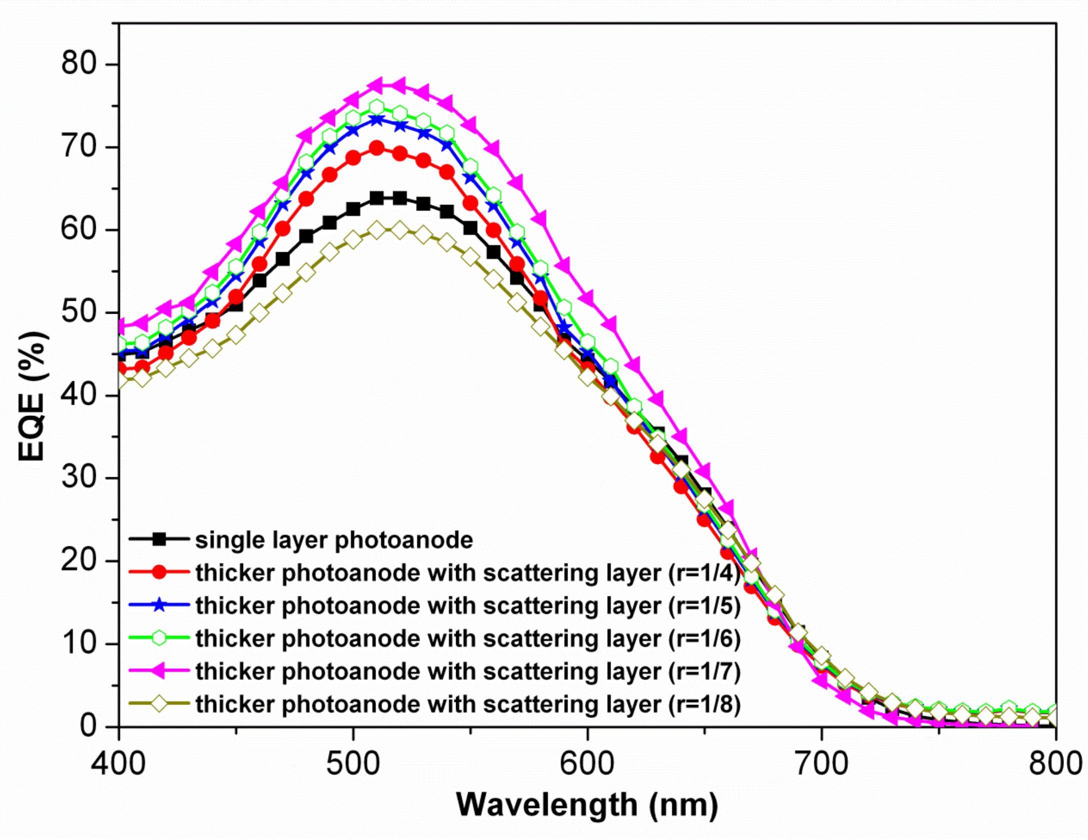

Fig 4. 10 EQE spectrum of thicker photoanode (8.9 ± 0.5μm) devices with/without scattering layer

Fig 4.11 reveals the reflectance spectrum for two photoanodes, respectively, with and without a scattering layer with the same thickness of photoanode prior to being sensitized. The spectrum shows that the reflectance of incident light in the range of 300-800 nm for the photoanode with scattering layer is higher than that of the photoanode without scattering layer, confirming enhancement of light trapping effect by introducing the scattering layer. Obviously, the reflectance of just the scattering layer by itself is expected to be higher; however, in actuality this is not terribly greater than the case of the photoanode with a scattering layer (*r*=1/4) as seen in Fig 4.11 showing the benefit of having a scattering layer in the photoanode. Increasing the ratio *r* can increase the reflectance.

Table 4.2 Characteristics of Different DSSC Photoanode Configurations

Structure	Thickness/μm	J_{sc}/ mAcm^{-2}	V_{oc} / V	FF/ %	PCE/%
Single layer	5.5	6.50	0.67	52	2.50
	9.2	20.10	0.74	48	7.14
r =1/4	5.2	10.10	0.77	63	4.89
	8.4	16.46	0.75	62	7.60
r =1/5	5.4	9.60	0.72	63	4.30
	8.9	22.50	0.71	60	8.40
r =1/6	5.4	11.39	0.75	62	5.30
	8.7	18.48	0.73	66	8.51
r =1/7	5.2	8.93	0.76	64	4.35
	9.3	23.03	0.73	55	9.28
r =1/8	5.7	6.68	0.75	63	3.29
	8.7	16.79	0.74	55	6.81

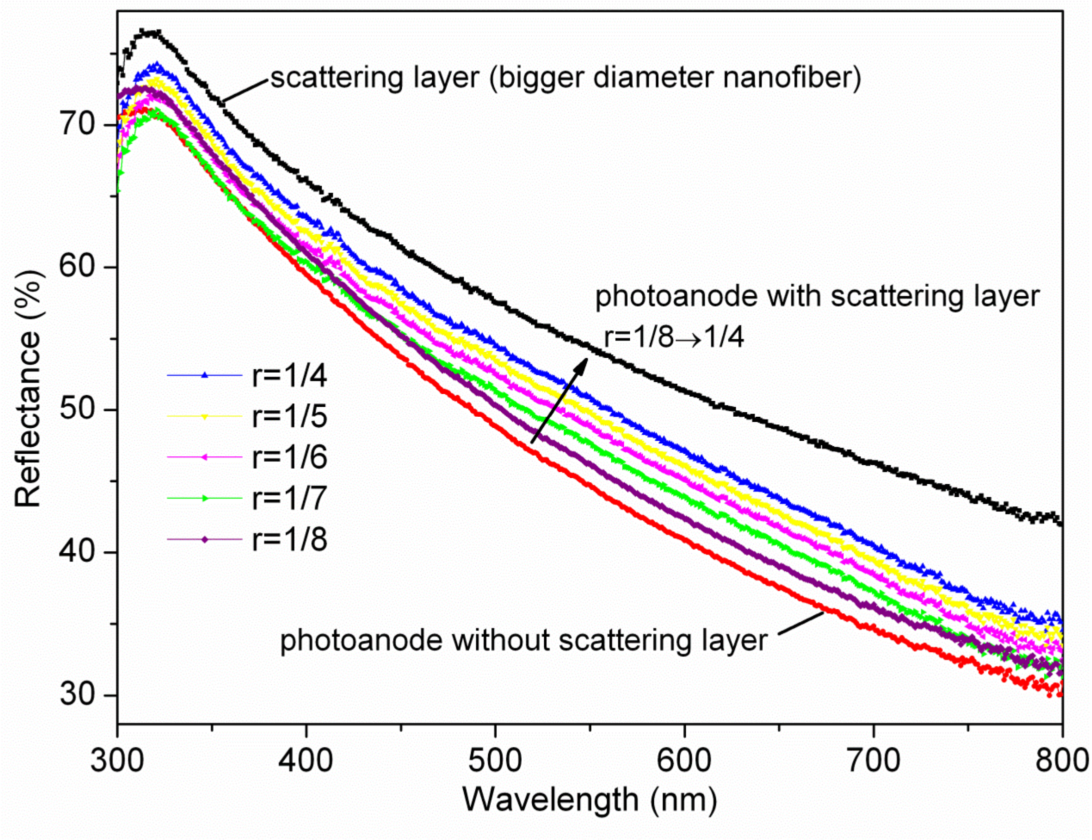

Fig.4.11 The reflectance spectrum for scattering layer, photoanode with scattering layer and without scattering layer

Although a thicker scattering layer enhances the light trapping effect; however, this sacrifices the dye-loading capacity of the photoanode due to the lower surface area of the scattering layer which is made of bigger diameter nanofiber. Fig 4.12 confirms this point. As *r* is increased from 1/8 to 1/4, the dye-loading capacity of the photoanode is decreased from 27.0×10^{4} to 19.63×10^{-4} mol-cm^{-3}, which represents a 27% reduction. It is obvious that to achieve enhanced scattering effect with introduction of a bigger-diameter nanofiber layer is offset by a loss of surface area for dye adsorption that results in poor light-harvesting efficiency. Therefore, the ratio of the scattering layer in a photoanode should be optimized to balance the dye-loading capacity and light-scattering effect.

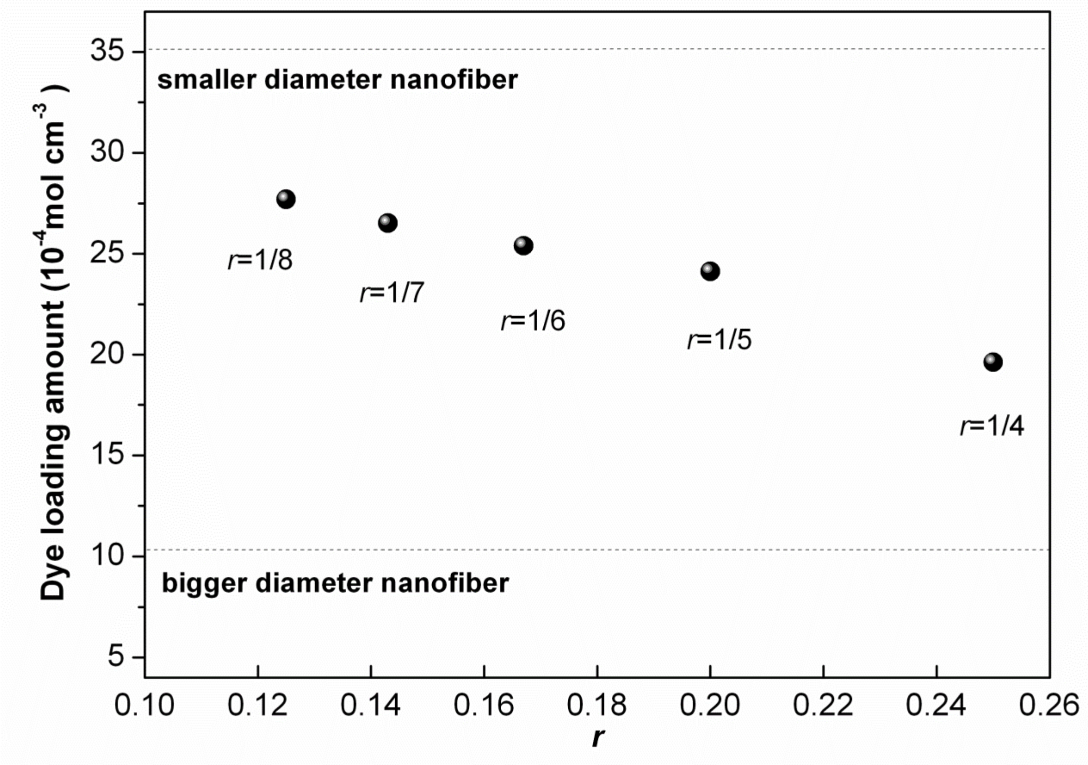

Fig 4.12 The relationship between dye loading amount and ratio of scattering layer (*r*) in the photoanode

In conclusion, the bigger diameter TiO_2 nanofiber was employed as an effective scattering layer to extend the light path in DSSC device. Systematic study on the effect of this scattering layer on performance of the device revealed that the light-trapping effect was related to the thickness of the photoanode. The light-trapping effect was more for a thicker photoanode. Moreover, the ratio of the scattering layer in the photoanode played an important part on the performance of the device. Increasing the ratio will increase the light trapping but sacrifice the dye-loading capacity in the photoanode. Optimizing the ratio of the scattering layer in the photoanode can be achieved by balancing the functions of the dye loading capacity and light-scattering effect. With the optimized ratio of scattering layer of 1/7 and 1/6 for the thick (8.9±0.5 μm) and thin (5.5±0.2 μm) photoanodes, respectively, the devices have the best performance with PCE of 9.28% and 5.30%. The thin photoanode (5.5±0.2 μm) benefited more from the scattering layer and a 112% increase in PCE can be realized at the optimal condition.

4.3 A Novel Scattering Layer Composed of Electrosprayed Polydispersed-size Nanocrystallite TiO_2

4.3.1 Advantages of electrosprayed scattering layer

An innovative scattering layer made of polydispersed electrosprayed nanocrystallite TiO_2 for the DSSC photoanode was developed to improve the light harvesting efficiency. This novel scattering layer has three major advantages. First, the electrosprayed TiO_2 nanoparticles were composed of nanocrystallites with diameter approximately 10 nm that did not sacrifice the dye loading capacity of the photoanode. Second, the diameter of the electrosprayed TiO_2 nanoparticle was polydispersed resulting in much lower porosity in the scattering layer, thereby improving effectively the light harvesting property of the device (Fig 4.13 a). Third, the size and distribution of the nanoparticles in the novel scattering layer can be engineered and fine-tuned easily by changing the operating parameter of electrospraying, such as the applied voltage.

4.3.2 Fabrication and characterization of DSSC with electrosprayed polydispersed-size nanocrystallite TiO_2 scattering layer

The scattering layer (polydispersed TiO_2 nanoparticles) with thickness of (2±1) μm was in situ electrosprayed on top of TiO_2 nanofiber (~60 nm) layer with thickness of (10±1) μm. First, the PVP/ TiO_2 composite nanofibers were dir ectly electrospun onto a FTO glass from a precursor solution: 1g of PVP (M_W=1,300,000, 1g), 1.2g of TIP, 1g of acetic acid and 30mL ethanol. An electric potential of 70kV was applied to the rotating electrode, which was spaced 19 cm from the collector. The resulting composite nanofiber (PVP/TiO_2) layer was exposed to air with moisture for about 5 hours to allow complete hydrolysis and subsequently was calcinated at 450°C for 2 hours. After calcination, this layer was peeled off from the original FTO glass and transferred to another FTO glass pre-coated with an ultra-thin TiO_2 paste. The TiO_2 nanofiber photoanode was obtained after calcinating again at 450°C for 2 hours. Subsequently, TiO_2 nanoparticles were electrosprayed from the same nozzle-less electrospinning setup onto the TiO_2 nanofibers photoanode from a precursor solution containing PVP (M_W=10,000, 1.5g), TIP (3g), acetic acid (2g) and ethanol (30mL). The electric potential of 50, 60 and 70 kV was applied during the electrospraying process, respectively, to study the effect of the different scattering layer configurations on the light harvesting of the DSSC device. Finally, the three samples were calcined at 450°C for 2 hours.

To compare the effectiveness of the novel scattering layer with the traditional approach, TiO_2 nanoparticles with monodispersed diameter of 200 nm was coated on a nanofiber photoanode with the same thickness of (2±1) μm. The resulting photoanode was further treated with an aqueous solution of $TiCl_4$ (40mM) at 60°C for 15 min and then sensitized in a solution of 0.3 mM Ru based dye (N719) solution in absolute ethanol at 55°C for 24 hour. The soaked photoanode was washed with absolute ethanol to remove unanchored dye molecules and subsequently dried in vacuum furnace at room temperature.

Fig 4.13 a. shows the two schematics of photoanode with the traditional and our novel scattering layer, respectively. Comparing with the traditional scattering layer, our novel scattering layer filled with polydisperesd nanoparticles exhibits lower pore volume (i.e. low light transmittance) which functions to trap more light in the dye absorption layer.

Fig.4.13 b-d shows the morphology of electrosprayed TiO_2 nanoparticles. Fig 4.13 b is a SEM image of TiO_2 nanofibers deposited with electrospray polydispersed nanoparticles. The nanofibers have average diameter of approximately 60 nm and length of at least 10 μm presenting a large length-to-diameter aspect ratio for the device. It is worthy to note that the nanoparticle layer shown in Fig 4.13 b was much thinner than what was typically adopted in our device to facilitate observation of the randomly distributed nanoparticles deposited on the surface of the nanofiber layers in the background. Fig 4.13 c and d are, respectively, the TEM and HRTEM images of the electrosprayed TiO_2 nanoparticles. These images indicate that the electrospray nanoparticles were polycrystalline and each nanoparticle was made up of TiO_2 crystallites with size approximately 10 nm. This reveals an interesting benefit that the electrosprayed nanoparticles have a large surface-to-volume ratio. Comparing with the traditional nanoparticles (diameter>100 nm) used as a scattering layer, it is of great benefit for the electrosprayed nanoparticles to serve partly for dye loading in the photoanode.

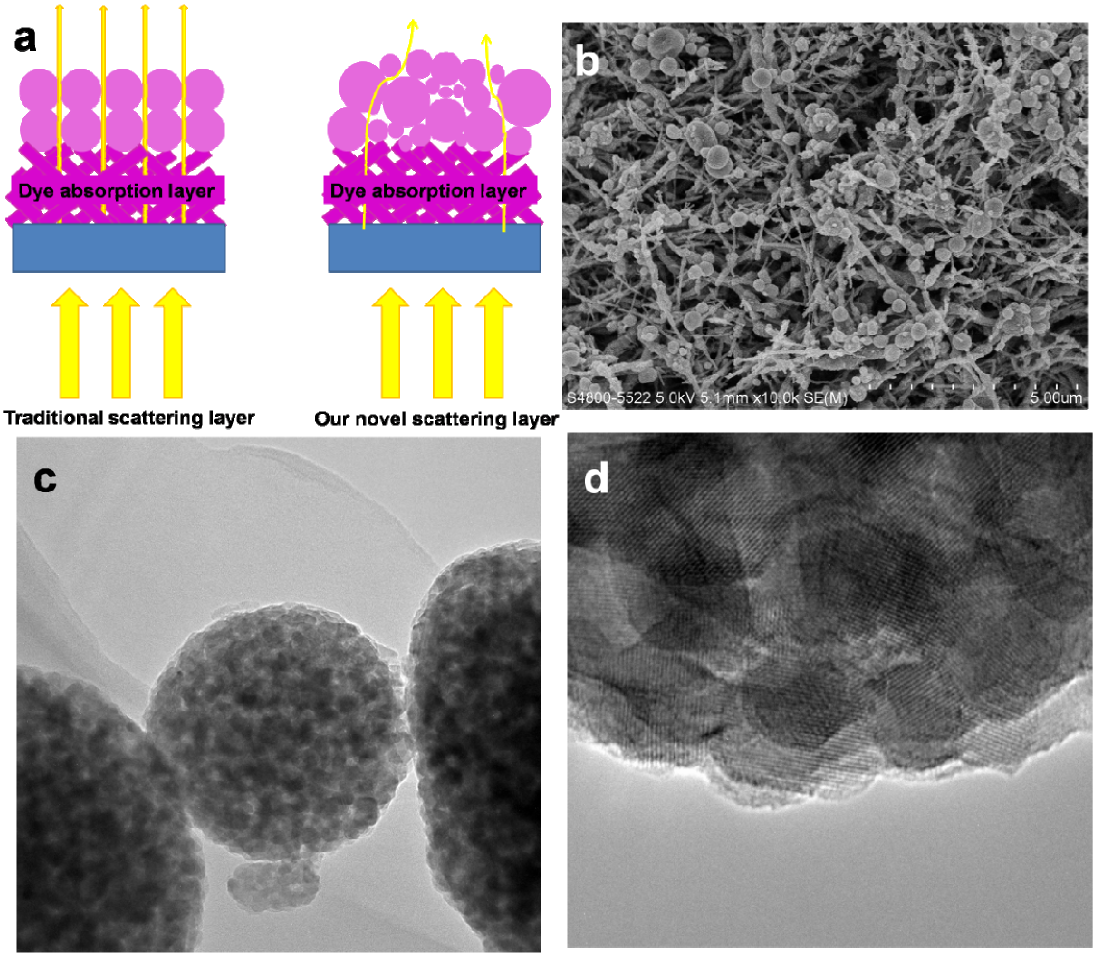

Fig.4.13 a, Schematic representation of DSSC with traditional scattering layer and the novel electrosprayed scattering layer; b, SEM image of electroaprayed TiO2 nanoparticles on nanofibers; c, TEM image of electrosprayed TiO2 nanoparticles; d, HRTEM image of electrosprayed TiO2 nanoparticle.

It is well-known that the morphology/diameter of electrospray nanoparticle depends on the operating parameters of the electrospraying, such as applied voltage, distance between electrode and collector, and the angular speed of the rotating electrode. Here, the effect of applied voltage on the morphology of electrospray nanoparticles was investigated. As mentioned earlier, the applied voltage of 50, 60 and 70 kV were adopted to produce the various sizes and size distribution of nanoparticles in the scattering layer, while the distance between the rotating electrode and the collector was maintained constant at 19cm. Fig 4.14 exhibits the measured diameter distribution of the electrosprayed TiO_2 nanoparticles at different electrospraying conditions. Of significance is that the electrosprayed particles obtained have diameter between 150 and 1000 nm that follows an approximate Gaussian distribution. The average diameter of the electrosprayed particles became larger when the applied voltage of electrospraying, thus the applied electric field, was reduced. It is known that a scattering layer consisting of larger particles can effectively reflect the incident light resulting in improved light harvesting for the solar cell. In the three test configurations, more than 40% nanoparticles have diameters greater than 400 nm for effective light scattering. The remaining balance of nanoparticles was smaller in size yet they have large surface-to-volume ratio, which lend them as good absorbents for the small dye molecules.

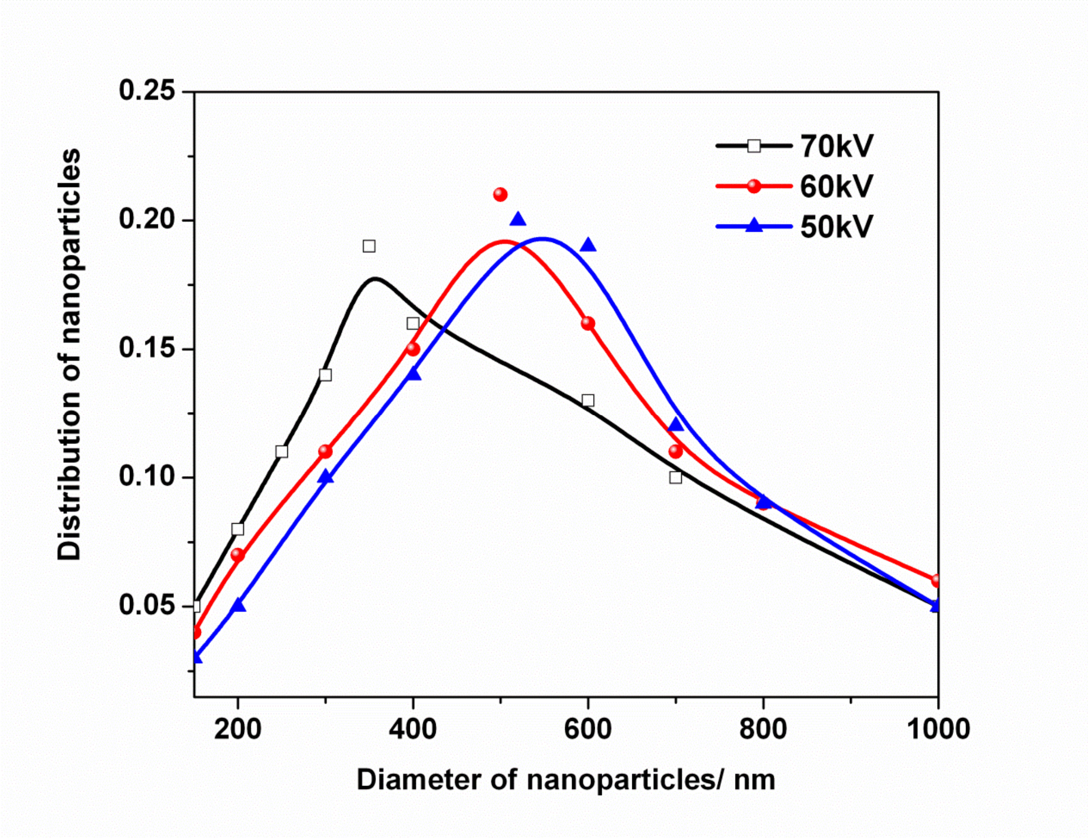

Fig 4.14 The diameter distribution of the electrosprayed TiO_2 nanoparticles under different applied voltage during electrospraying.

The amount of the dye adsorbed respectively in different electrosprayed scattering layers and the traditional scattering layer (200 nm nanoparticles) were measured. Dye loading on these scattering layers was quantified by desorbing the dye from the layers in 0.1M NaOH solution (water: ethanol=1:1) and subsequently the absorption spectra of the solutions were measured. The amount of dye adsorbed on the electrosprayed scattering layer at 70, 60 and 50 kV was determined to be 7.3×10^{-4}, 5.1×10^{-4} and 4.6×10^{-4} mol cm^{-3}, respectively; while the amount of dye adsorbed in the traditional scattering layer was much lower at 2.9×10^{-4} mol cm^{-3}. It can be seen that the electrosprayed scattering layer can absorbed at least 1.5 times of dye molecules than that of the conventional scattering layer. This indeed confirms that the novel scattering layer, superficially packed with large quantities of nano-sized crystallites, have higher dye-loading capacity. Therefore, the electrosprayed scattering layer with polydispersed sizes can function both as a light scattering layer as well as an effective dye loading layer.

The light scattering/ trapping effect of different scattering layer, prepared at different applied voltages during electrospray, can be compared based on their reflection properties. Fig 4.15 shows that the reflectance of incident light with wavelength in the range from 300 to 800 nm for different scattering layers for the same thickness prior to sensitizing with the N719 dye. From the reflection spectrum depicted in Fig 4.15, the scattering layer electrosprayed at 60 kV shows the strongest reflectance in the UV, or near UV region, with wave length between 300 and 400 nm; while the traditional scattering layer made up of 200 nm nanoparticles shows the weakest reflectance in the same wavelength range. In the visible-light wavelength between 400 and 800 nm, the electrospray scattering layer exhibits stronger light scattering property than that of traditional scattering layer. Among the three electrosprayed scattering layer configurations, the one electrosprayed at 50 kV has the best performance followed closely by the one at 60 kV. It is to be noted that the traditional scattering layer shows better light trapping property than that of nanofiber alone without a scattering layer, which also can be shown in the normalized EQE spectrum (Fig. 4.16). This confirms the effectiveness of light trapping with a scattering layer resulting in improved light utilization in the DSSC device.

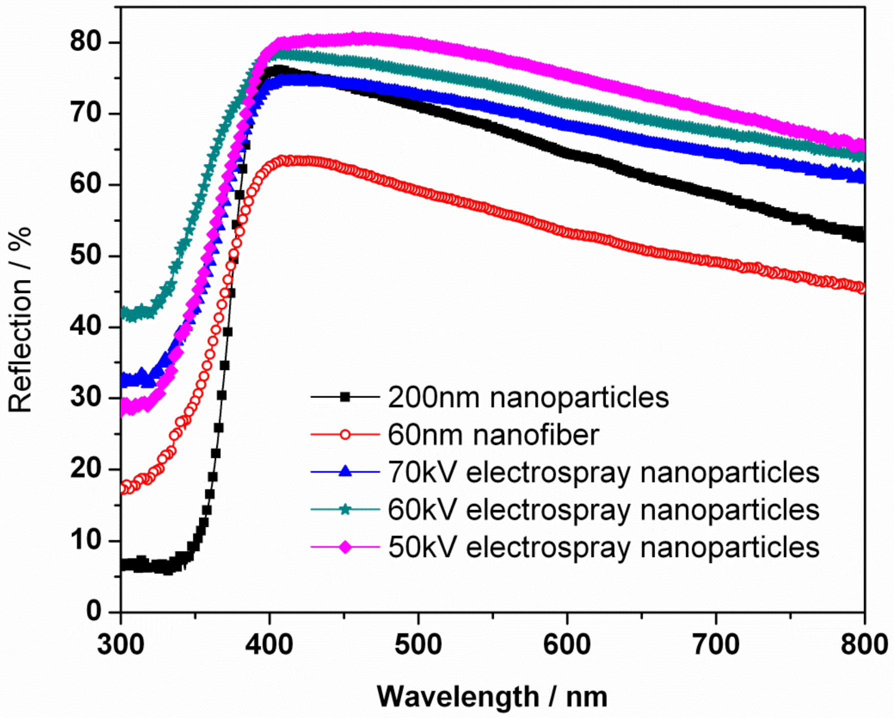

Fig 4.15 Reflectance of incident light of different scattering layers

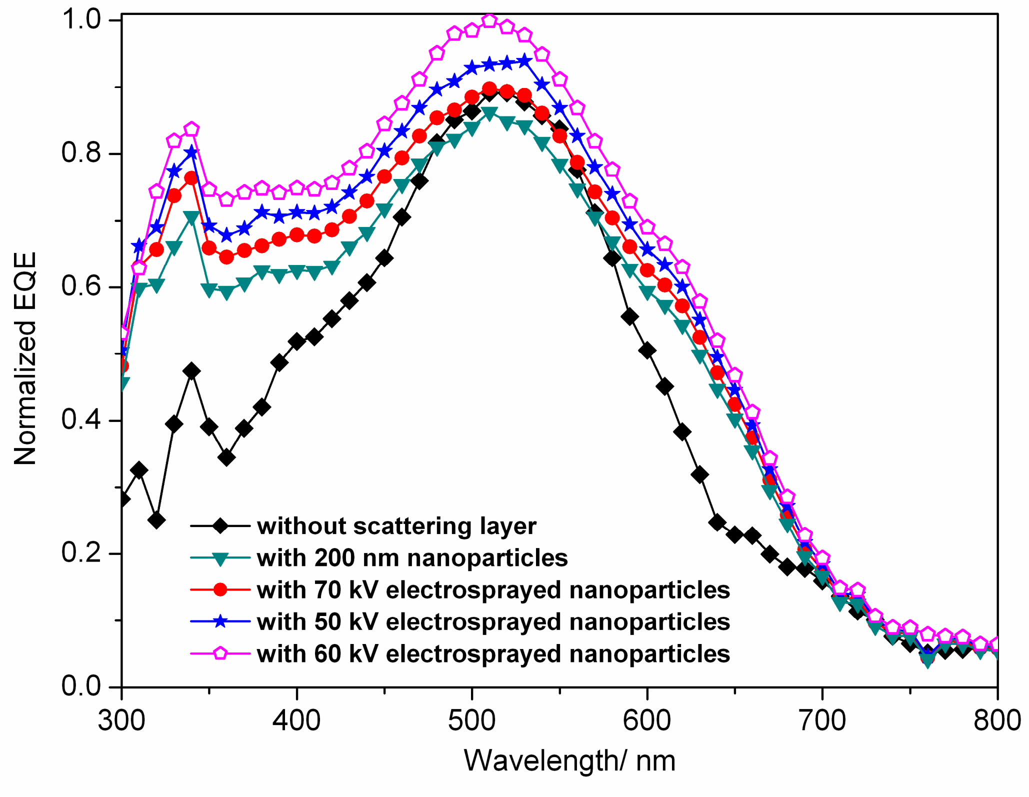

Fig 4.16 EQE spectrum of DSSC devices with and without scattering layer

Fig 4.17 shows the *J-V* characteristics of DSSC with and without an electrosprayed scattering layer. The *J-V* curve reveals that the photoanode with the scattering layer achieves higher photocurrent when compared with photoanode without a scattering layer. The enhanced photocurrent is mainly due to the enhanced light harvesting capability by including the light scattering layer. Table 4.3 shows the photovoltaic performances of DSSC with and without the electrosprayed scattering layer. The V_{oc} and FF were nearly the same for all configurations of the photoanode devices, indicating the scattering layers and their configurations have insignificant effect on the V_{oc} and FF of the device. The short-circuit current density was improved by introducing a scattering layer in the photoanode. By introducing the traditional mono-dispersed nanoparticles as the scattering layer for the DSSC device, the J_{sc} increased from 13.70 to 14.96 mAcm^{-2}, which is a 9% increase. On the other hand, the electrosprayed polydispersed nanoparticle scattering layer showed a significant improvement with J_{sc} ramping up to 17.84 mA/cm^{-2} and the corresponding PCE increasing to 8.71% when 60kV electrosprayed scattering layer was incorporated in the photoanode. These represent a significant 30% and 31% improvement in J_{sc} and PCE, respectively, when compared to the case without a scattering layer. For comparison purpose, when incorporate the 50 kV and 70 kV electrosprayed scattering layer, the improvement in J_{sc} was about 20% and 14%, respectively. Therefore, the 60kV electrosprayed nanoparticles as the scattering layer were the optimal reflector for the nanofiber photoanode. Comparing with the 50 kV electrosprayed layer, the 60kV configuration showed higher dye-loading capacity given the particle size distribution was slightly finer. On the other hand, comparing with the 70 kV electrosprayed layer, the 60 kV configurations exhibited stronger light scattering property (see Fig 4.15) as it has coarser particle size distribution (see Fig 4.14). Therefore, the dye loading capacity and light trapping ability was well balanced in the device which with the 60 kV electrosprayed scattering layer. The improvement over single nanofiber layer is well beyond that achieved with the traditional scattering layer as seen in Table 4.3. It is obvious that the present novel electrosprayed scattering layer with polydispersed TiO_2 nanoparticles outperforms the traditional scattering layer using monodispersed 200 nm nanoparticles in DSSC.

Table 4.3 Photovoltaic characteristics of DSSC photoanode with and without scattering layer

	J_{sc}/mAcm^{-2}	V_{oc} /V	FF /%	PCE /%
Without scattering layer	13.70	0.72	67	6.64
With traditional scattering layer(200nm)	14.96	0.76	63	7.17
With 50kV electrosprayed scattering layer	16.50	0.73	66	7.94
With 60kV electrosprayed scattering layer	17.84	0.75	65	8.71
With 70kV electrosprayed scattering layer	15.58	0.74	65	7.52

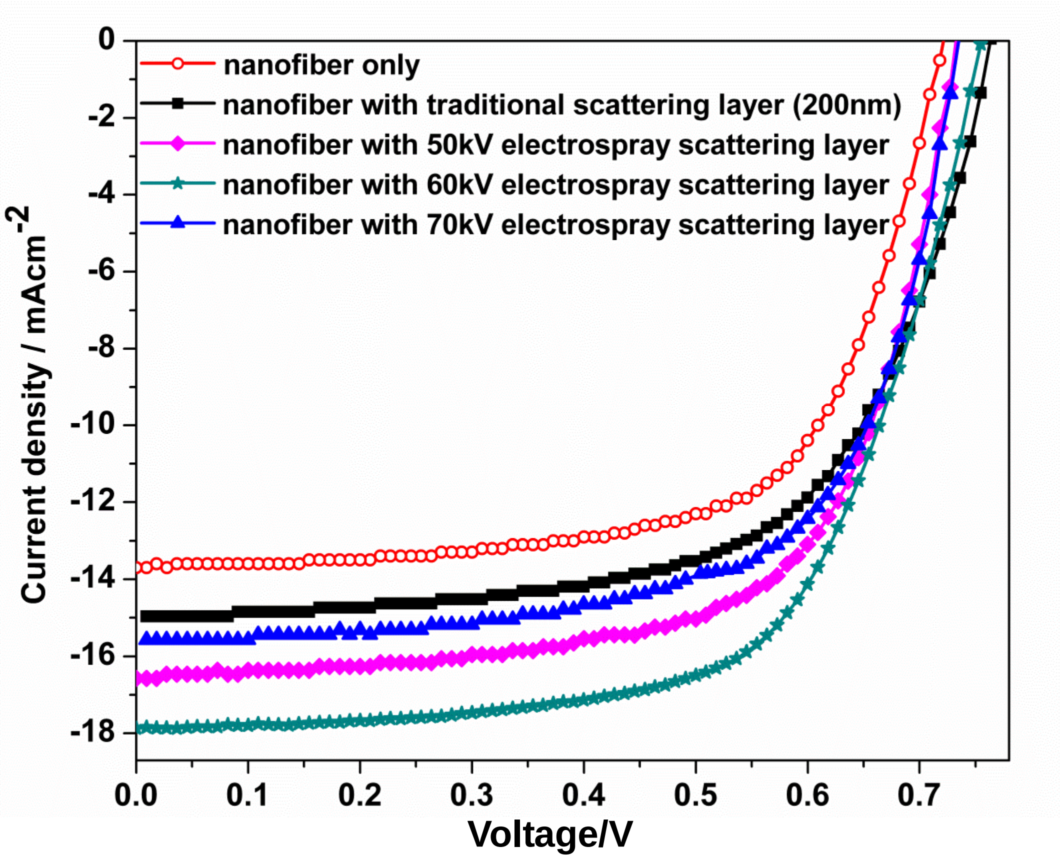

Fig 4.17 J-V curves of DSSC photoanode with and without scattering layer

In summary, electrosprayed TiO_2 nanoparticles can be applied as a novel scattering layer in DSSC to improve the performance of the device. Comparing with the traditional scattering layer, the electrosprayed nanoparticles as a novel scattering layer consisted of numerous nano-crystallites (10 nm size) packed on the nanoparticles. This provides the scattering layer with an added advantage of high dye-loading capacity. Due to the polydispersed distribution of the particle size (i.e. diameter), the porosity of the scattering layer is reduced trapping more incident light in the device. Thus, our unique scattering layer configuration with polydispersed nanoparticles with each particle composed of polycrystallites of 10nm size can extend the light path in the device without compromising the dye loading ability. A high efficiency of 8.71% can be achieved with our novel scattering layer which is 21% greater than a device with the traditional monodispersed 200 nm nanoparticles scattering layer having only 7.17% efficiency.

Chapter 5

Improvement of Light Harvesting in Dye Sensitized Solar Cell Based on Cascade Charge Transfer

5.1 Introduction

In chapter 4, the novel scattering layers were successful introduced in the photoanode to improve the light harvesting efficiency of DSSC. Given the key feature of DSSC device is to utilize photosensitizing dye that harvests light and generates excitons. To achieve high-power conversion efficiency based on iodine/ triiodine redox couple system which would be competitive with conventional silicon-based solar cells, DSSC must absorb as much as 80% of the solar spectrum with wavelength between 350 and 900 nm. It is difficult to further improve PCE of the device with traditional ruthenium-based dyes, such as N719 and N3, because of their low molar extinction coefficient (5,000-20,000$M^{-1}cm^{-1}$)[18, 69], despite they exhibit relative broad absorption spectrum. On the other hand, organic dyes, such as metallophthalocyanines (MPcs), show higher molar extinction coefficient (100,000 $M^{-1}cm^{-1}$), they have narrow absorption bandwidth [25, 70]. Complementally, dye cocktails or co-sensitization have been proposed to enhance the light absorption and extend the absorption spectrum of the device; however, hitherto there is only limited success along this direction. This is probably due to (i) inferior charge injection efficiency caused by intermolecular interactions between different dyes; and (ii) limited adsorption surface area of the photoanode for dyes adsorption. Considerable efforts have been made to solve these problems. One possible solution is to separate the adsorption sites on TiO_2, which means acquiring the appropriate location of each dye on the desired site. However, this approach is difficult to realize because of the complicated production process. Recently, Förster resonance energy transfer (FRET) was utilized in DSSC to enhance light harvesting where an unattached, highly luminescent donor dye was dissolved in the electrolyte solution to absorb high-energy photons and then efficiently transfer this energy to the anchored near-infrared acceptor dye [71-74]. Unfortunately, triiodine (I_3^-) in the electrolyte was found to quench partially the fluorescence of the donors, limiting the improvement of the performance.

In this investigation, we demonstrate that an ultra-thin layer of near-infrared dye, copper phthalocyanine (CuPc), deposited on the exterior or periphery of ruthenium based dye (N719) sensitized TiO_2 nanofibers, can harvest complementary light thereby extending the absorption spectrum of the device. Upon illumination, the excited electrons in the CuPc molecules are injected to the N719 and then passed onto the conduction band of the TiO_2 nanofibers. This broadens the absorption bandwidth of DSSC device covering nearly the entire spectrum of the visible solar irradiation[75].

5.2 Experiments

TiO_2/PVP composite nanofibers were first electrospun on FTO glass from precursor solution which contained 1.2 g of TIP, 1g of PVP (M_w=1,300,000), 1g of acetic acid and 30mL ethanol. The voltage of 70kV was applied over a collector distance of 19 cm. TiO_2 nanofibers were obtained after calcination at 450 °C for 2 h. The nanofiber mat was peeled off from the original FTO glass and got transferred to a second FTO glass already pre-coated with an ultrathin TiO_2 paste layer to improve adhesion between the FTO glass and the nanofiber photoanode. The photoanode was calcinated again at 450 °C for 2h. The TiO_2 nanofiber photoanode was subsequently treated with an aqueous solution of 40mM $TiCl_4$ at 60°C for 15 min. After treatment, the film was washed with absolute ethanol and dried in vacuum at 80 ^{o}C, and subsequently it was immersed in the solution of 0.3 mM N719 in absolute ethanol at 55°C for 24 h for dye attachment onto the nanofibers. Prior to loading into the vacuum chamber of the thermal evaporation setup, the soaked photoanode was washed with ethanol to remove “unanchored” dye.

The CuPc layer with different thickness, 20, 25, 30, 35, and 40nm, respectively, were deposited on the N719 sensitized TiO_2 nanofiber photoanode using thermal evaporation under reduced pressure of less than $1x10^{-6}$ Torr at a deposition rate of approximately 0.5 Å/s. The target surface was rotated during deposition to maintain uniformity. A 6MHz gold crystal monitor was used to determine film thickness and deposition rate.

5.3 Results and Discussion

Unlike the single dye case as discussed in Chapter 4, there are two paths for charge generation and transfer in the present system, which are depicted in Fig 5.1 a. Upon illumination, N719 molecules are excited and an electron-hole pair is created. Electrons are injected into the conduction band (CB) of TiO_2. In this novel design, CuPc absorbs the near-infrared photon and also creates an electron-hole pair, i.e. exciton. The exciton diffuses to the interface between CuPc and N719 molecules and dissociates due to the lowest unoccupied molecular orbital (LUMO) level at the interface. The electron transfers first to the LUMO of N719 and injects subsequently to the CB of TiO_2. This completes the cascade charge transfer process.

The present novel core-shell photoanode design has several advantages. First, the one-dimensional TiO_2 nanofiber maintains the fast charge transport property.

Second, the surface roughness and porosity of nanofibers film favor deposition of the primary and secondary dyes (N719 and CuPc, respectively) on the photoanode.

Third, the introduced secondary dye (CuPc) in form of an ultra-thin layer, shielding externally the N719 sensitized TiO_2 nanofiber photoanode, extends the absorption bandwidth.

Fourth, this arrangement further avoids the competition of the second dye with the first dye (N719) for the anchored sites of TiO_2, which heretofore has been a limiting factor with conventional co-sensitization.

Fifth, the two dyes are spatially and energetically organized to achieve electrons transfer from the outer- to the inner-dye layer, while holes transfer reversely from the inner- to the outer-dye layer.

Sixth, this configuration increases the separation distance between injected electrons traveling along the CB of TiO_2 and the oxidized dye species, thereby suppresses the recombination process in the device (Fig.5.1b)[37, 76]. The structures of CuPc and N719 can be seen in Fig 5.1 c.

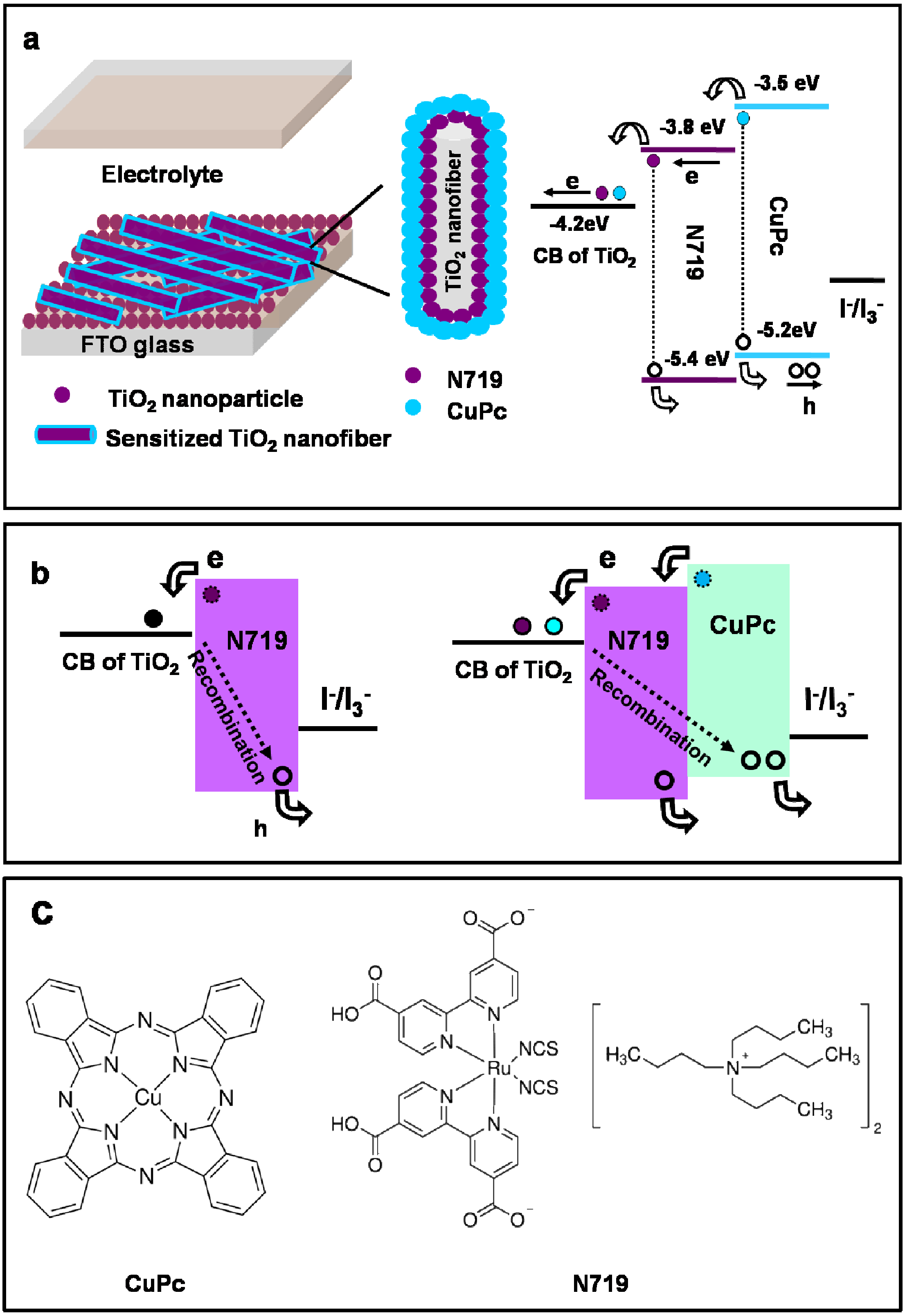

Fig 5.1 a, Schematic representation of DSSC with core-shell structure photoanode and corresponding energy diagram; b Schematic recombination process in DSSC with and without CuPc shell;c Structure of CuPc and N719

Fig 5.2 is a schematic of the thermal evaporation set up. The CuPc-shell was deposited on the N719- sensitized- TiO_2 nanofiber-core using thermal evaporation method under a reduced pressure. To maintain uniformity, the target surface (i.e. substrate) was rotated during deposition.

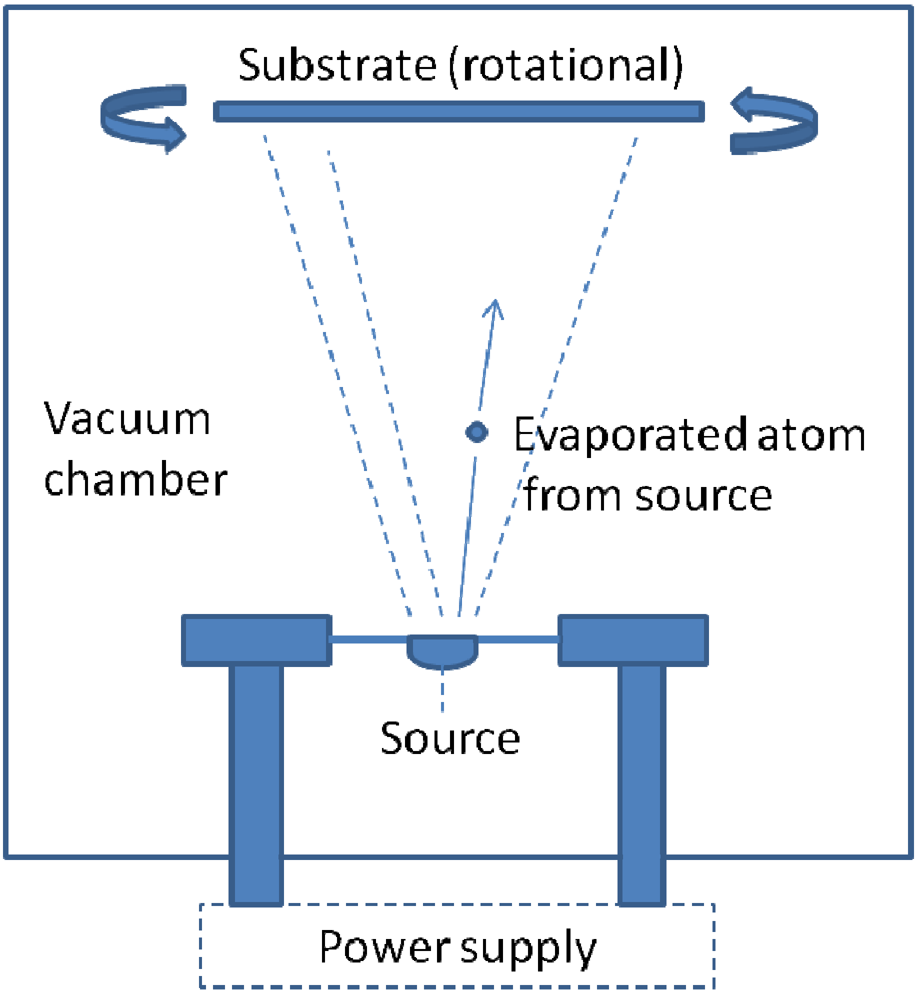

Fig 5.2 Schematic of thermal evaporation set up

Fig 5.3 a displays the morphology of N719 sensitized TiO_2 nanofiber, while Fig 5. 3 b and c display the morphology of the N719 sensitized TiO_2 nanofiber coated with 30nm CuPc. Both SEM and TEM images suggest that the CuPc is not a simply superficial film on the entire photoanode but it takes form of a shell structure covering the core made up of N719 sensitized TiO_2 nanofiber.

It is noted that the CuPc deposition cannot penetrate depth-wise across the entire nanofiber mat. Despite this, the high porosity and permeability of the TiO_2 nanofiber mat enable deposition of CuPc relatively deep into the mat, forming the core-shell structure as can be seen in Fig 5.3 d and e, which are the cross-sectional SEM of TiO_2 nanofiber film (around 15μm) coated with 30 nm CuPc and a line scanning element mapping of this film. In Fig 5.3 e, carbon is selected to represent CuPc ($C_{32}H_{16}CuN_8$) while titanium represents TiO_2 nanofiber, respectively. From the line scanning element mapping, it can be seen that in the upper layer (about first 5μm), the concentration of carbon is relative high and it decrease further down into the nanofiber film. This indicates that the deposited CuPc can penetrate deeply (as much as 2/3) into the TiO_2 nanofiber mat.

This novel core-shell photoanode is different from the traditional approaches that were made up of two different semiconductors, or semiconductor-insulator configuration, to reduce the recombination process.

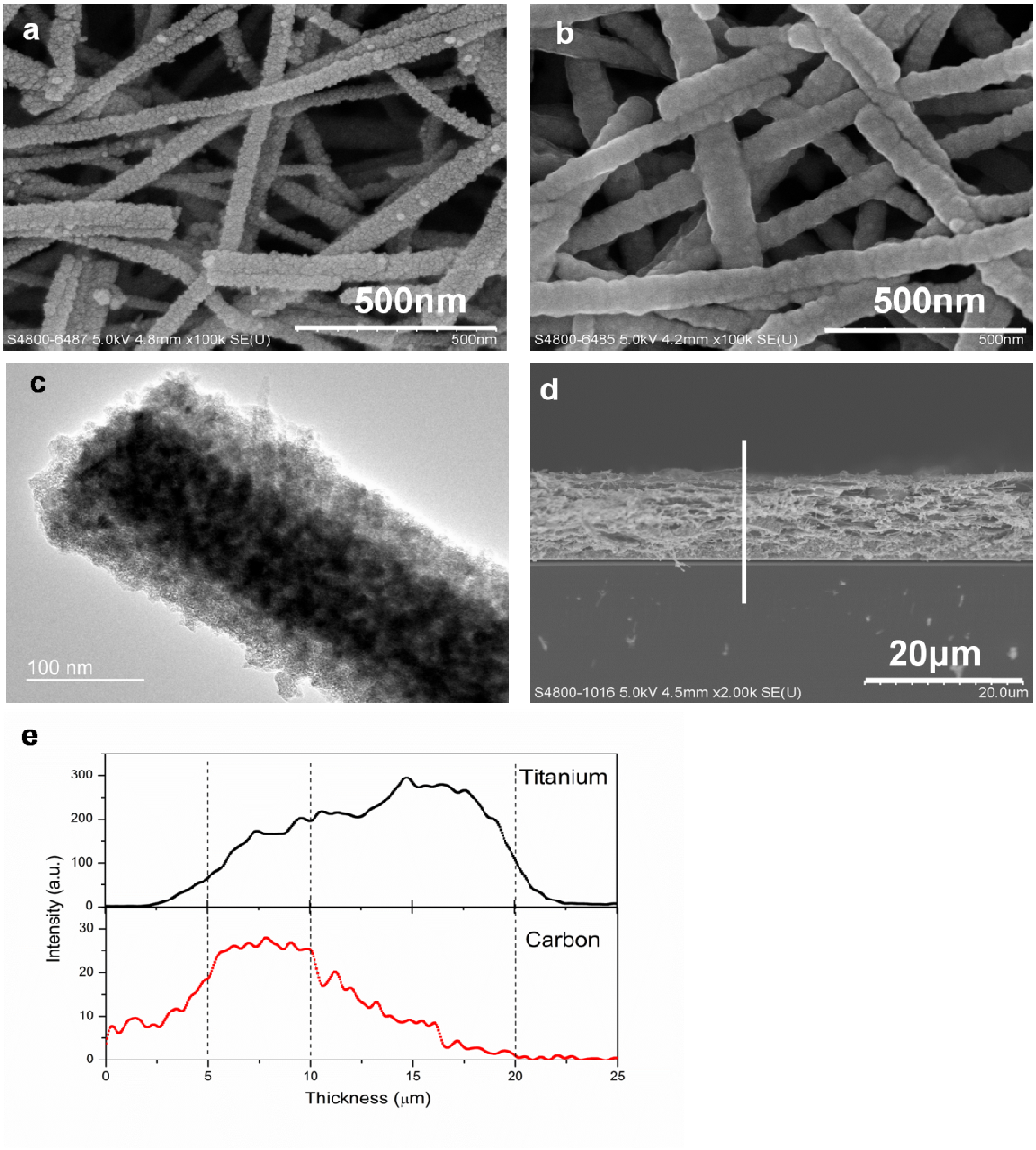

Fig 5.3 a, SEM image of TiO_2 nanofiber sensitized with N719; b, SEM image of CuPc (30 nm) coated N719 sensitized TiO_2 nanofiber; c, TEM image of CuPc coated N719 sensitized TiO_2 nanofiber; d, the cross-sectional SEM of TiO_2 nanofiber mat coated with CuPc; e, a line scanning element mapping the content of titanium and carbon.

Fig 5.4 delineates the absorption spectrum of various sensitized photoanode configurations, respectively: N719/TiO_2, CuPc/TiO_2 and CuPc/N719/TiO_2. The absorption bandwidth of N719 sensitized TiO_2 is in the range from 400 to 550nm, while the absorption bandwidth of CuPc coated TiO_2 are in two ranges, respectively, 340-380nm and 550-700nm. It is clear that upon introducing the CuPc shell layer, the absorption spectrum of the photoanode (CuPc/N719/TiO_2) has been broadened up including the near-infrared range.

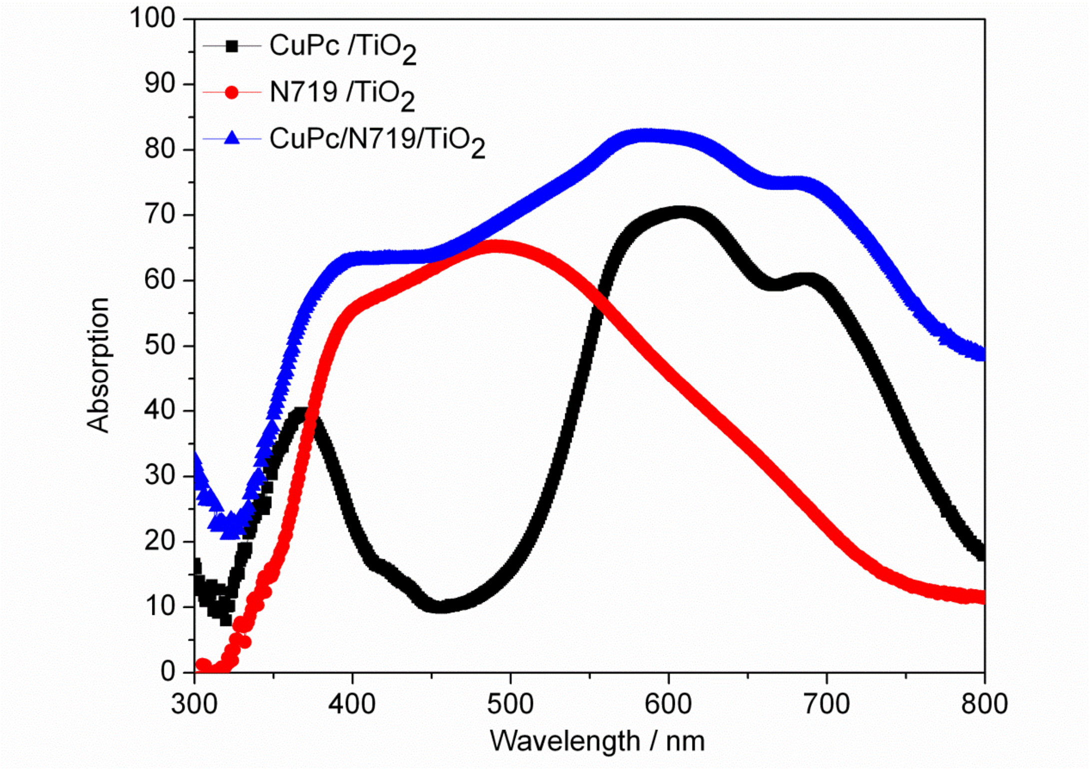

Fig 5.4 Absorption spectrum of photoanode: N719/TiO_2, CuPc/TiO_2, CuPc/N719/TiO_2

Furthermore, the photoluminescence (PL) emission spectrums corresponding to CuPc, N719, TiO_2, N719/TiO_2 and CuPc/N719/TiO_2 are shown, respectively, in

Fig 5.5. There is no evident emission peak for CuPc and N719 in the wavelength ranging between 330nm and 800nm. The emission spectrum of TiO_2 nanofiber film is around 420nm, which is mainly attributed to the recombination of photogenerated electron-hole pairs in TiO_2, which can be seen in Fig 5.6 a. Another peak, at about 470nm, is induced by the equipment, which can be ignored. It is interesting that after sensitized by the N719 dye, the emission intensity of TiO_2 nanofiber film is reduced. As is well known, the electron-hole pairs recombination in TiO_2 competes with the electron injection/hole transport. It suggests that the electron is transferred effectively from the lowest unoccupied molecular orbital (LUMO) of N719 to the CB of TiO_2 and concurrently hole transfers from the valence band (VB) of TiO_2 to the highest occupied molecular orbital (HOMO) of N719. In consequence, the number of electron-hole pairs in TiO_2 is reduced in the N719/TiO_2 system, thus the PL intensity is also reduced (Fig 5.6 b).

On the other hand, the emission intensity of N719/TiO_2 is enhanced with introduction of CuPc, which suggests the charge generation and transfer mechanism is as follows. Photons are absorbed by CuPc upon illumination and excited electrons are transferred directly to N719, and subsequently to the CB of TiO_2, while holes transfer from the VB of TiO_2 to the HOMO of N719, and subsequently to the HOMO of CuPc. When CuPc is introduced in N719/TiO_2, the concentration of electrons in the CB of TiO_2 is increased; the recombination rate is likewise higher. In comparison with N719/TiO_2system, CuPc/N719/TiO_2 shows indeed higher PL emission as depicted in Fig 5.5. With increasing electron-hole pairs recombination, the electron injection/hole transport rate is also increased as discussed contributing to higher performance.

Given there is no overlap between the absorption spectrum of N719 and the emission spectrum of CuPc, the FRET process according to Förster theory cannot be observed in our N719 sensitized TiO_2 -core, CuPc-shell device.

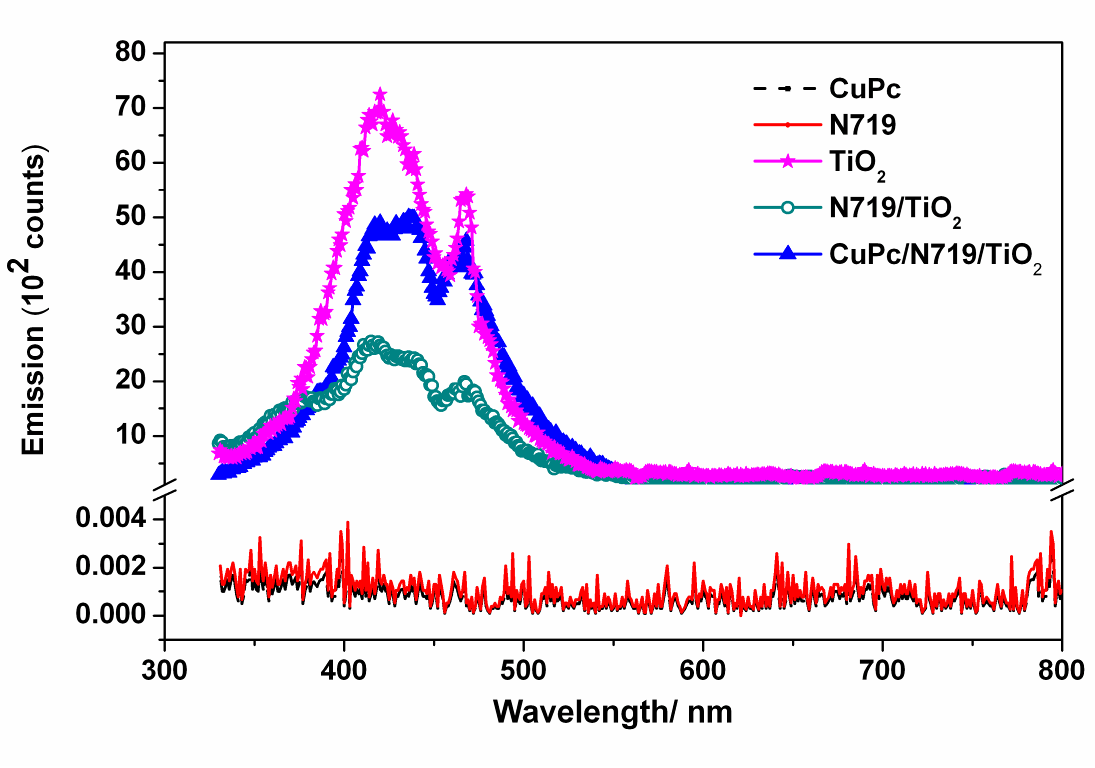

Fig 5.5 Emission spectrum of CuPc, N719, TiO_2, N719/TiO_2 and CuPc/N719/TiO_2

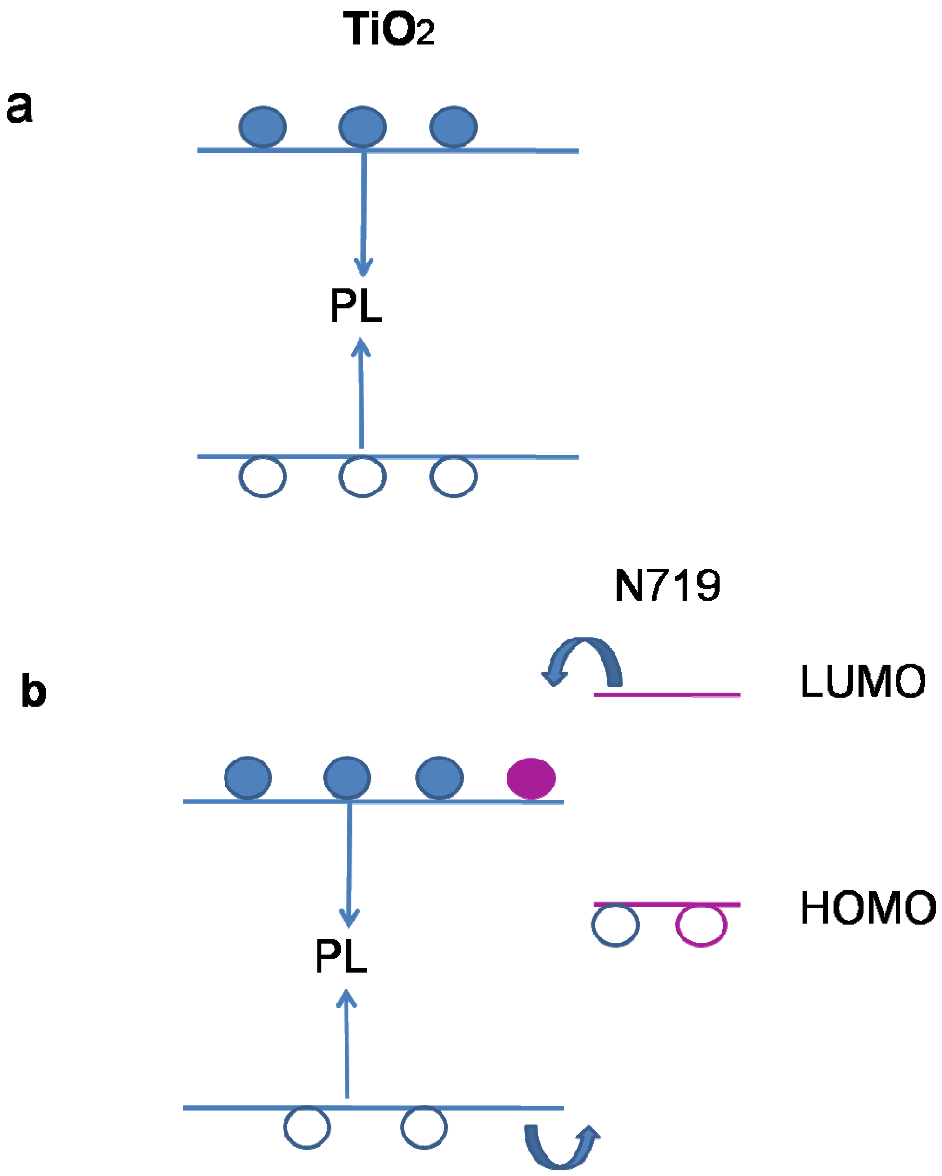

Fig 5.6 Schematic of photogenerated charges recombination and transfer between TiO_2 and N719

Fig 5.7 shows the *J-V* characteristics of DSSC, respectively, with and without 30nm CuPc layer under AM1.5 ($100mWcm^{-2}$) illumination; and results are tabulated in Table 5.1. The thickness of all the tested photoanodes of devices was maintained at 13 ± 1 μm. As shown in Table 5.1, the V_{oc} remained almost constant independent of the presence/absence of CuPc. The device sensitized with only N719 showed a PCE of 6.39% while the PCE for the device with an addition of 30nm CuPc shell escalated up to 9.48%, which is a 48% increase. This improvement is attributed primarily to the increase in J_{sc} and FF.

Table 5.1 Photovoltaic characteristics of DSSC with and without 30nm CuPc

	30nm CuPc	Without CuPc	Change %
J_{sc} ($mAcm^{-2}$)	21.12	14.97	41.08
V_{oc} (V)	0.74	0.75	-1.33
FF (%)	60.65	56.91	6.57
PCE (%)	9.48	6.39	48.36
R_s (Ωcm^2)	2.34	10.07	-76.76
R_p (Ωcm^2)	641.5	414.8	54.65

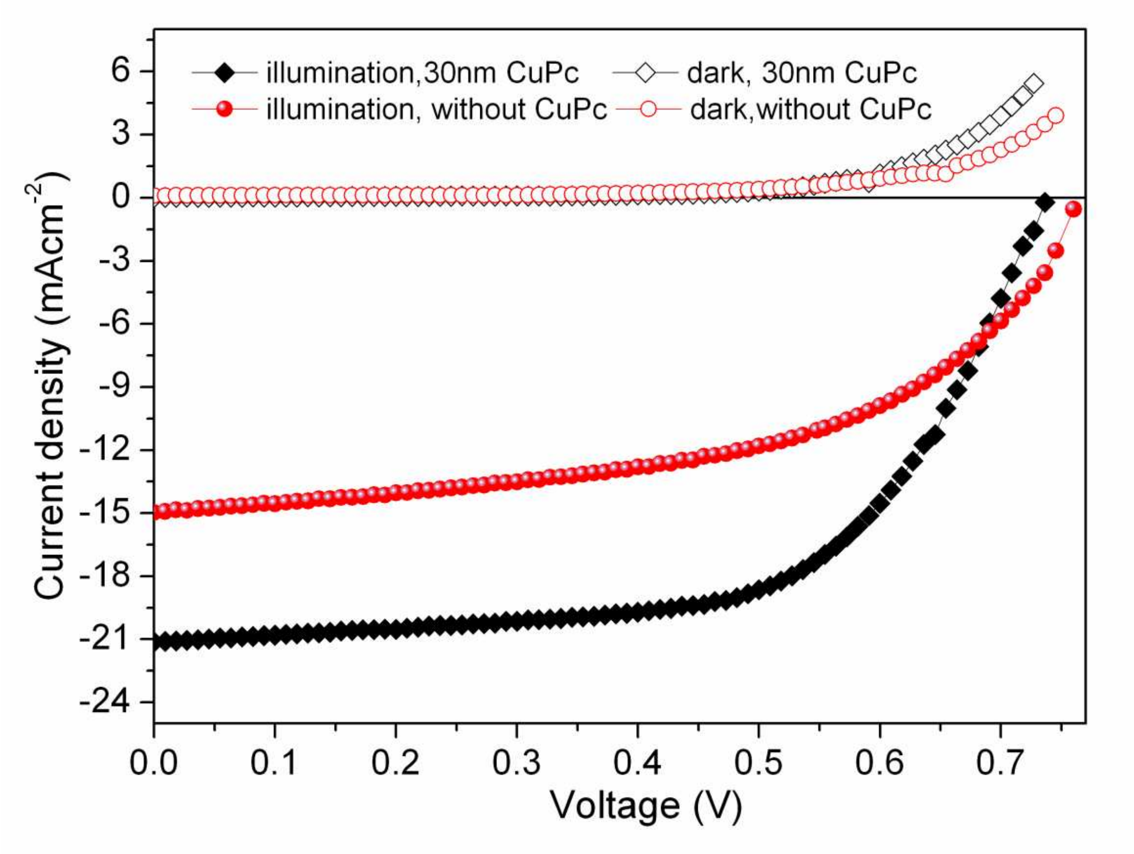

Fig 5.7 Photocurrent density– voltage (*J*-*V*) characteristics of DSSC devices with and without CuPc (30nm)

Interestingly, as shown in Fig 5.8 the reference device with a photoanode made of CuPc/TiO_2 was found to have extremely low J_{sc} and PCE, respectively, 0.67mAcm^{-2} and 0.18%. It is known that CuPc with multiple and symmetrical carboxyl groups is easy to synthesize, however it is difficult to sensitize the semiconductor, i.e. TiO_2, because electrons cannot inject directly from CuPc into the CB of TiO_2. Hence, the device with CuPc/TiO_2 photoanode shows disappointingly low PCE. The improved performance as evident from the high J_{sc} realized through introducing the CuPc shell was due to the cascade charge transfer from the CuPc through N719 to the CB of TiO_2. This is the second of the two routes for charge generation and transfer besides the primary route from N719 to the CB of TiO_2. As can be seen, besides harvesting light N719 also functions as a charge carrier, or transport channel, connecting CuPc and TiO_2.

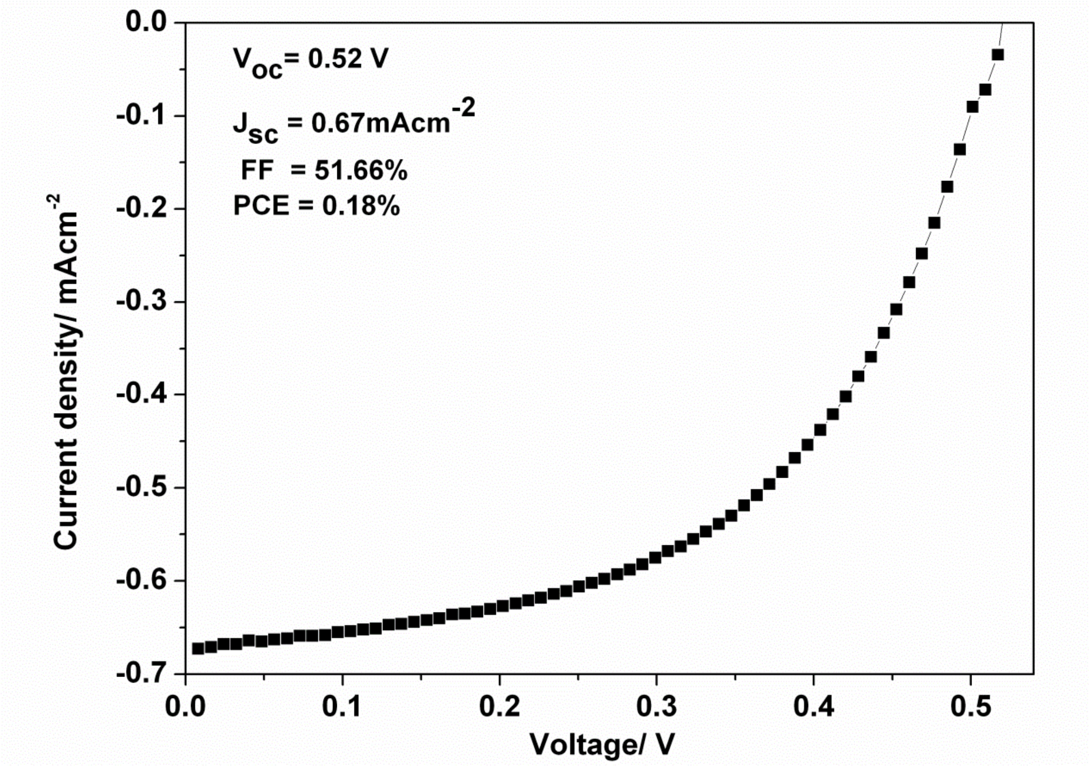

Fig 5.8 Photocurrent density –voltage (*J*-*V*) characteristic of device with the photoanode of CuPc/TiO_2 under AM1.5 (100mWcm^{-2})

Besides harvesting light, introducing the CuPc layer in the photoanode can further reduce the recombination process. Electron transport (ET) properties can be investigated by electrochemical impedance spectroscopy (EIS). Fig 5.9 is the EIS spectrum of DSSC devices with and without 30nm CuPc under

AM1.5 (100mWcm^{-2}) illumination. Three semi-circles are observed in the measured frequency between 10^{-1} and 10^{6} Hz (Fig.5.9), which represent the charge transport resistance at the Pt-counter electrode/ electrolyte (first semi-circle), charge transfer resistance at interface of photoanode/ dye/ electrolyte (second semi-circle), and diffusion process of I_3^- in the electrolyte (third semi-circle), respectively[49, 54, 77]. It can be seen that the device with 30nm CuPc layer shows lower charge transfer resistance, in other words, the charge transport property through the photoanode is improved with consequence that electron recombination being reduced.

Moreover, from the *J-V* curve, R_s (series resistance) and R_p (parallel resistance) can be calculated and they are listed in Table 5.1. R_s arise from the internal resistance and resistive contacts of the device, while R_p from the leakage of the current. For an efficient solar cell, small R_s but large R_p are needed. Here, through introducing the CuPc-shell, R_s decrease and R_p increase, which renders the device more efficient.

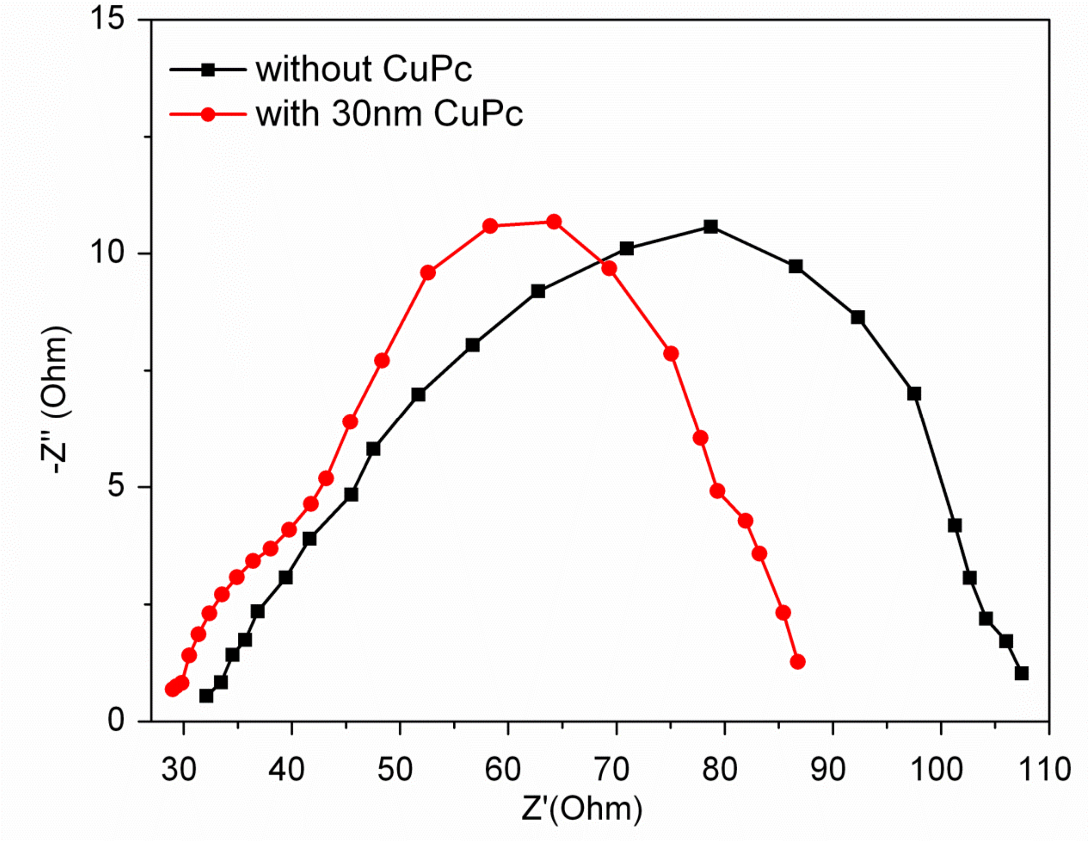

Fig 5.9 EIS of DSSC devices with and without 30nm CuPc under AM1.5 ($100mWcm^{-2}$) illumination

To provide further insight into the mechanism of enhanced J_{sc}, the normalized external quantum efficiency (EQE) is examined in the two wave-length regimes: 350 to 400nm and 550 to 800nm as depicted in Fig 5.10 a. The increase of EQE is attributed to the introduced CuPc that can absorb photons in these regions for additional charge generation. As shown in Fig 5.10 b, the normalized EQE enhancement, i.e. Δnormalized EQE, was calculated based on the difference between normalized EQE of the device with and without CuPc. The Δnormalized EQE has three peaks, respectively, at 355, 570 and 700nm, corresponding to 0.4, 0.23, and 0.37 enhancement in normalized EQE. These peaks match very well with those from the absorption spectrum of CuPc (see Fig. 5.4).

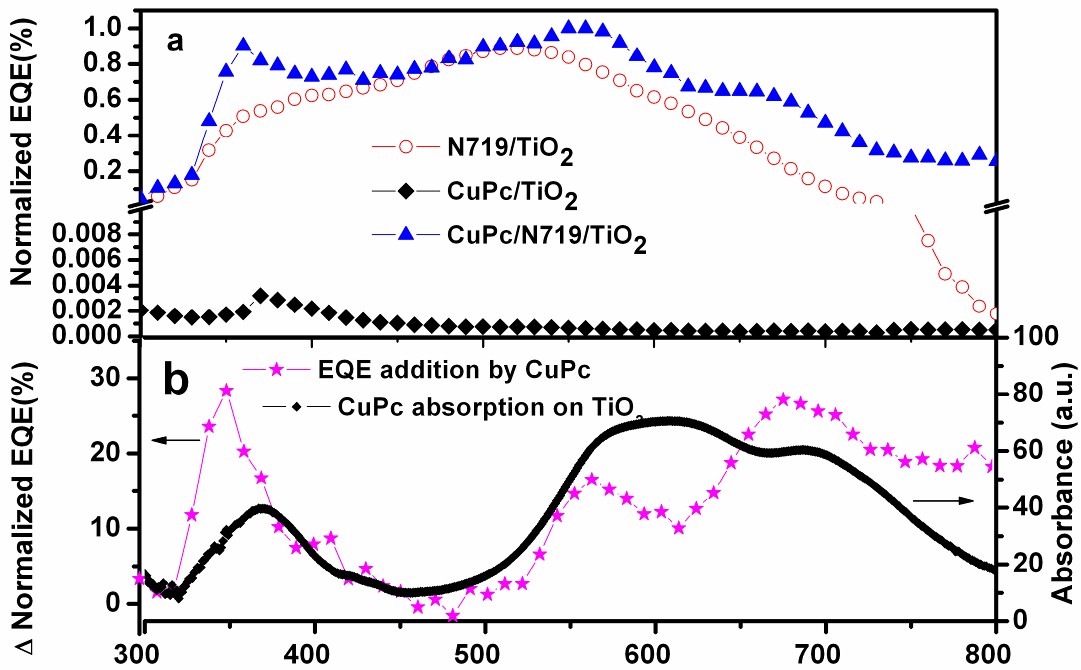

Fig 5.10 a, Normalized EQE versus wavelength of the DSSC with and without CuPc (30nm); b, Normalized EQE addition (Δ Normalized EQE) from adding 30nm CuPc and corresponding absorption spectrum of CuPc on TiO_2

It is known that I_3^- in the electrolyte is a “prefect quencher”[74, 78]. The excited state of the outer-most shell of the CuPc, which is exposed to the electrolyte, is therefore quenched (Fig 5.11).

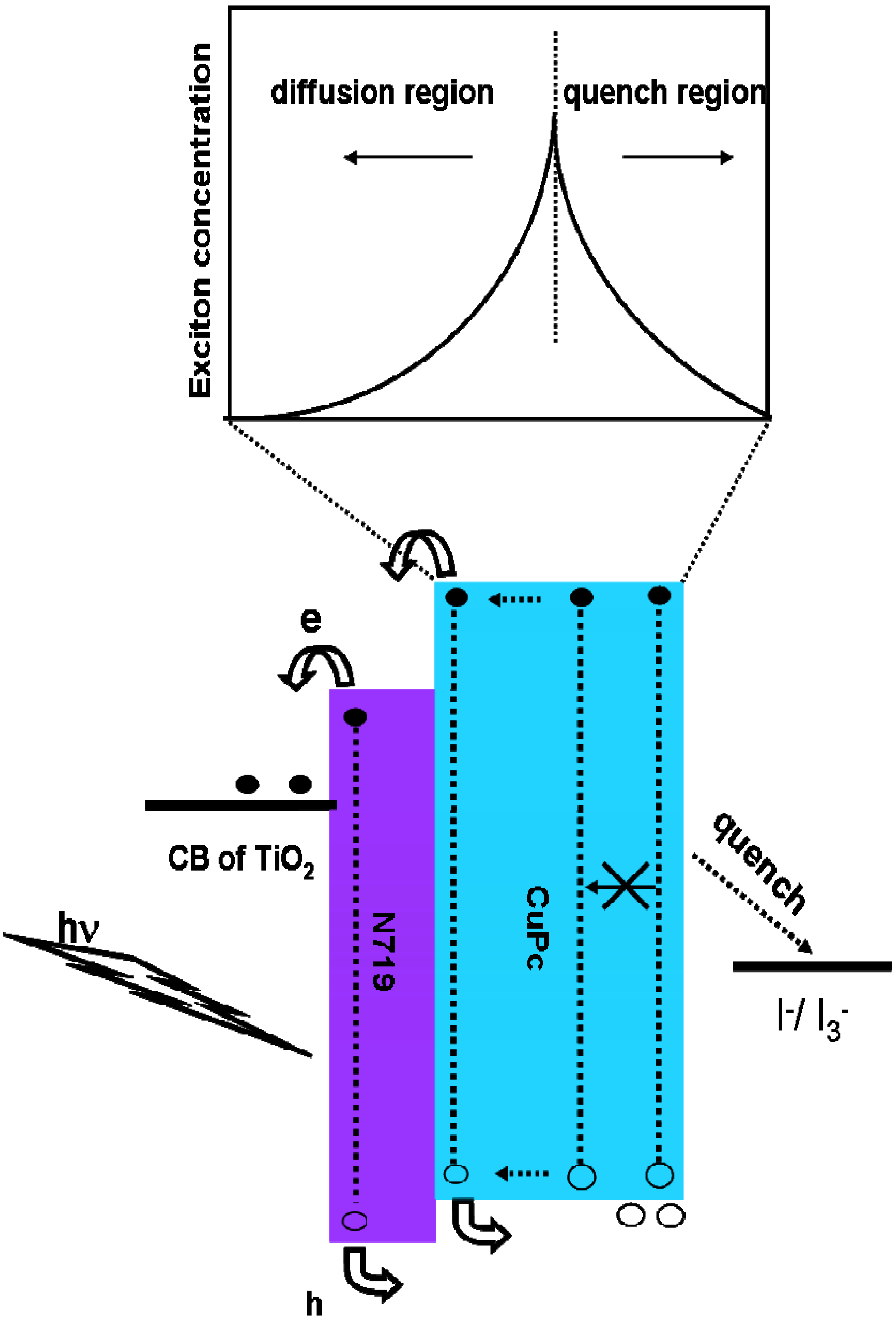

Fig 5.11 Schematic of electrolyte (I_3^-) quenching the excited state of the CuPc and relationship between exciton concentration and distance from closer to N719 to far from N719

As such, an appropriate CuPc shell should have a thickness of more than the exciton diffusion length (about 15nm) to compensate for the loss from the quenching effect. In our tests, different thicknesses from 20 to 40 nm of CuPc shell were tested for optimization. Shown in Fig 5.12, the SEM images reveal the morphology.

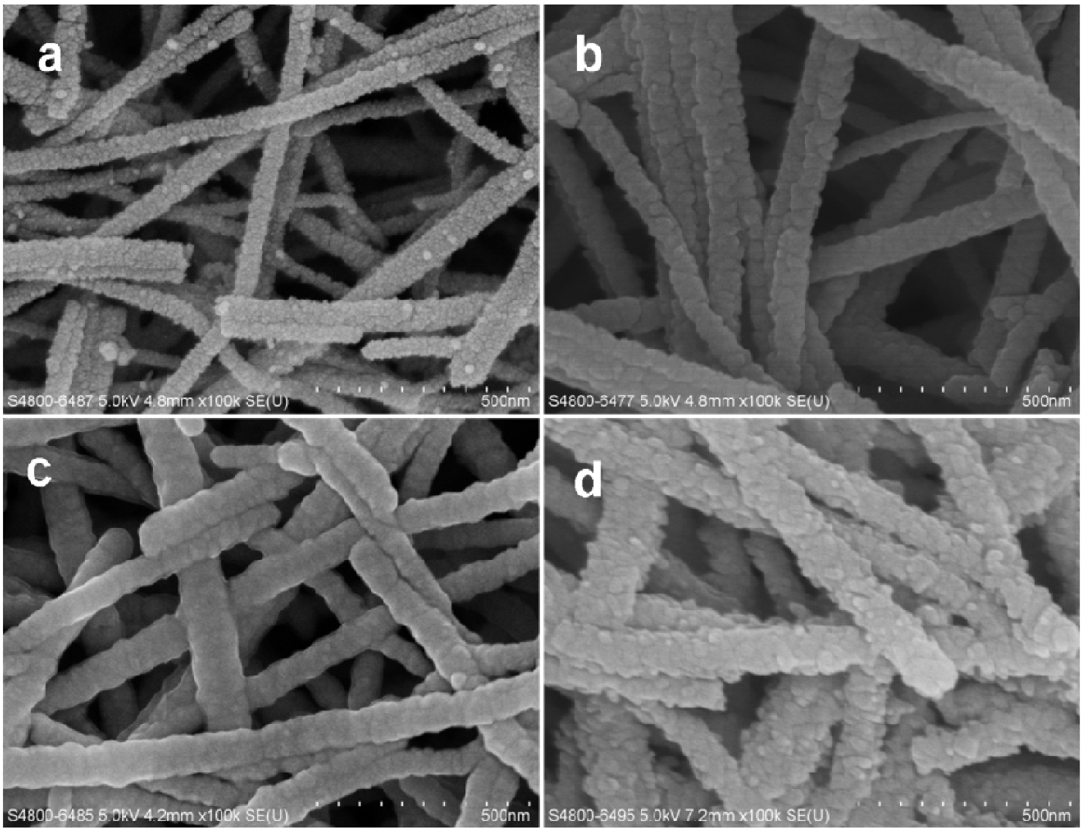

Fig 5.12 SEM images of CuPC coated N719 sensitized TiO_2 nanofibers: a, without CuPc; b, 20nm CuPc; c, 30nm CuPc; d, 40nm CuPc

The respective photovoltaic properties (V_{oc}, J_{sc}, FF and PCE) of these photoanodes are plotted in Fig 5.13 a-d. As shown in Fig. 5.13 c, V_{oc} for all the devices remains nearly constant at 0.73 ± 0.02V. As shown in Fig. 5.13 d, FF is maintained at 60% when thickness of the CuPc layer is less than 30nm, thereafter it decreases to 54% when the CuPc thickness is increased to 40nm. As shown in Fig. 5.13 a, b, the maximum PCE of 9.48% together with the highest J_{sc} are achieved when the CuPc layer thickness is at 30nm.

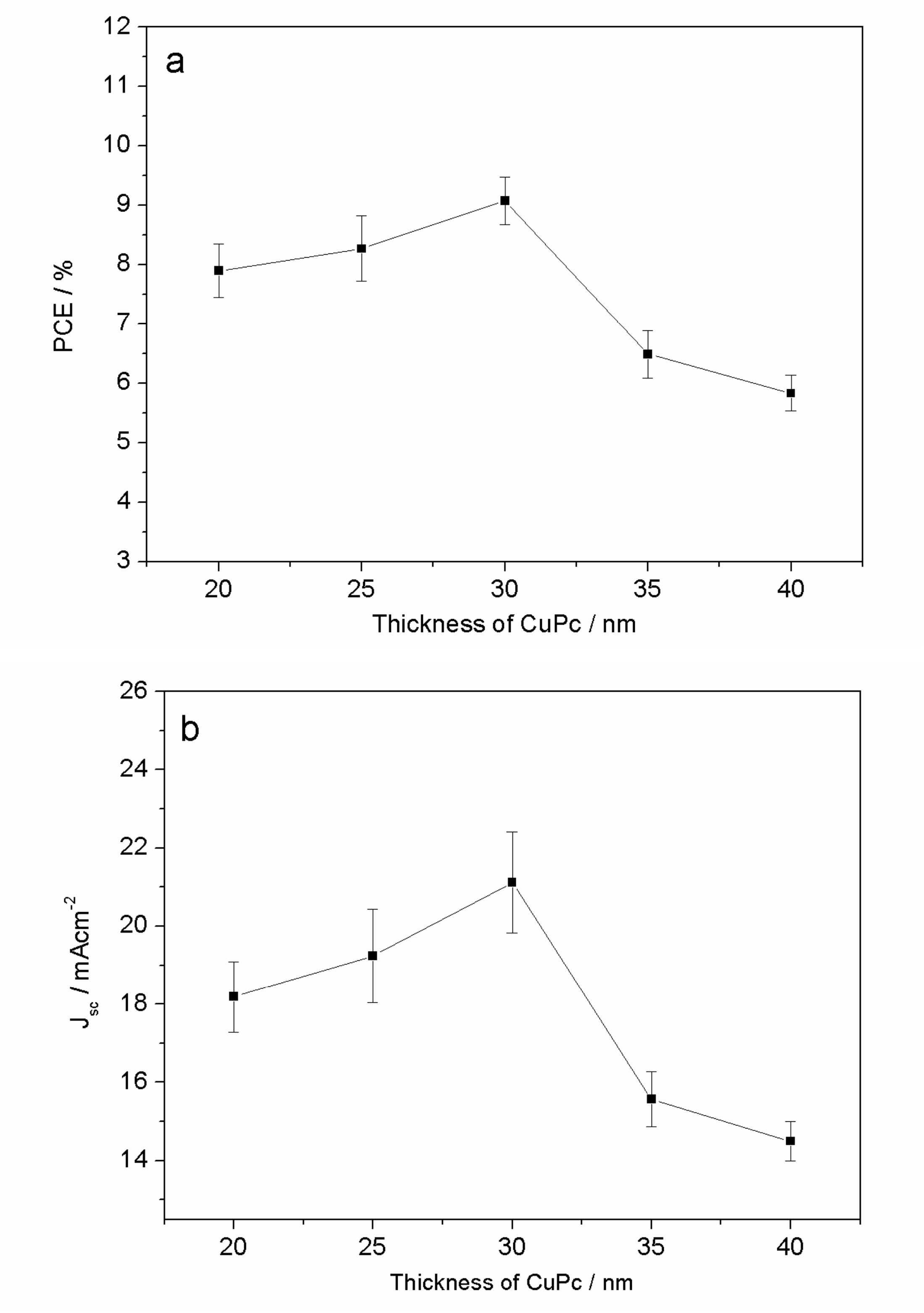

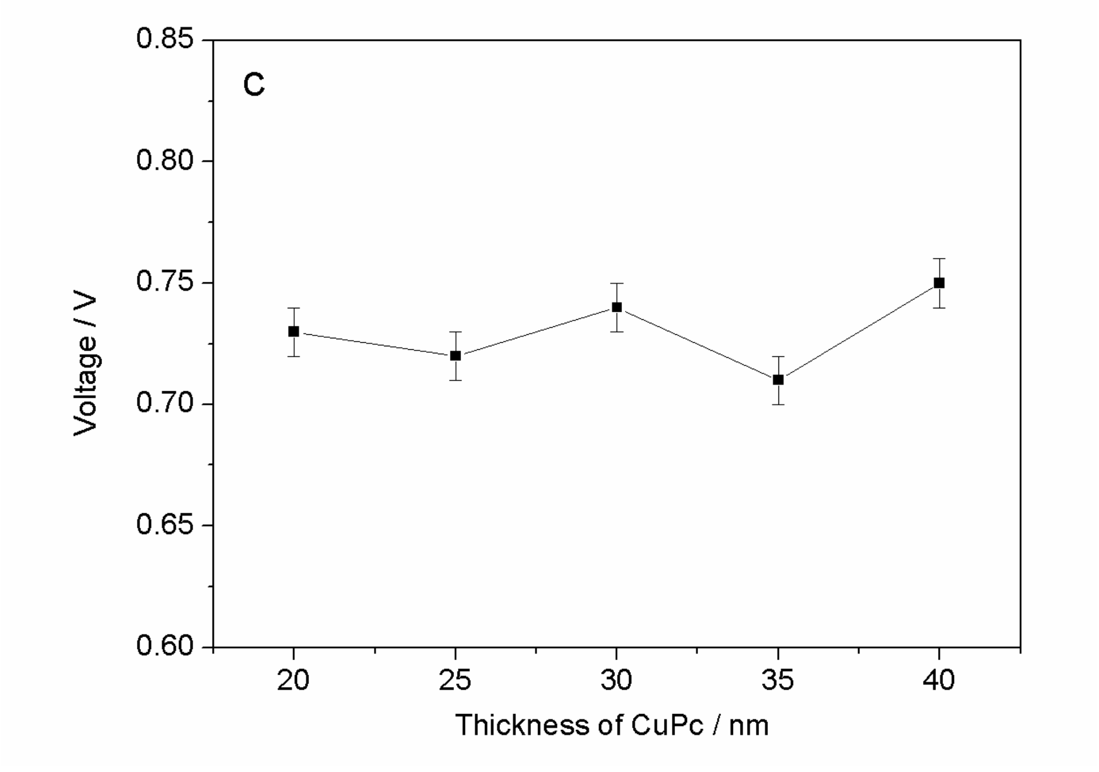

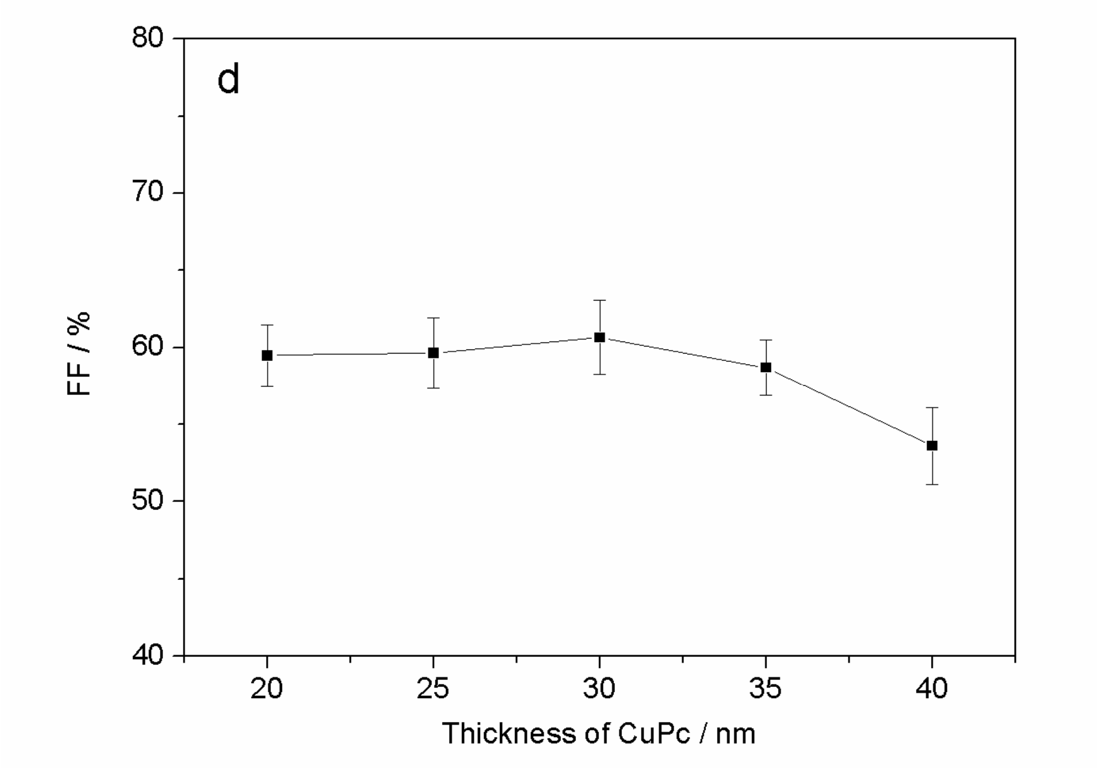

Fig 5. 13 Photovoltaic characteristic of DSSC devices with different thickness of CuPc. a, PCE versus thickness of CuPc; b, J_{sc} versus thickness of CuPc; c, V_{oc} versus thickness of CuPc; d, FF versus thickness of CuPc

On the other hand, poorer performance is obtained when the CuPc thickness is either above, or below, this optimal thickness. With increasing thickness of CuPc starting from a thin shell in the photoanode, more electrons are generated under solar irradiation and they get transferred to the TiO_2 photoanode via the N719, resulting in improved performance. However, when the thickness of CuPc exceeds the combined exciton diffusion length and the quench layer thickness, the excess CuPc incurs extra resistance for holes transport with negative consequence of retarding regeneration of N719 (see Fig 5.14).

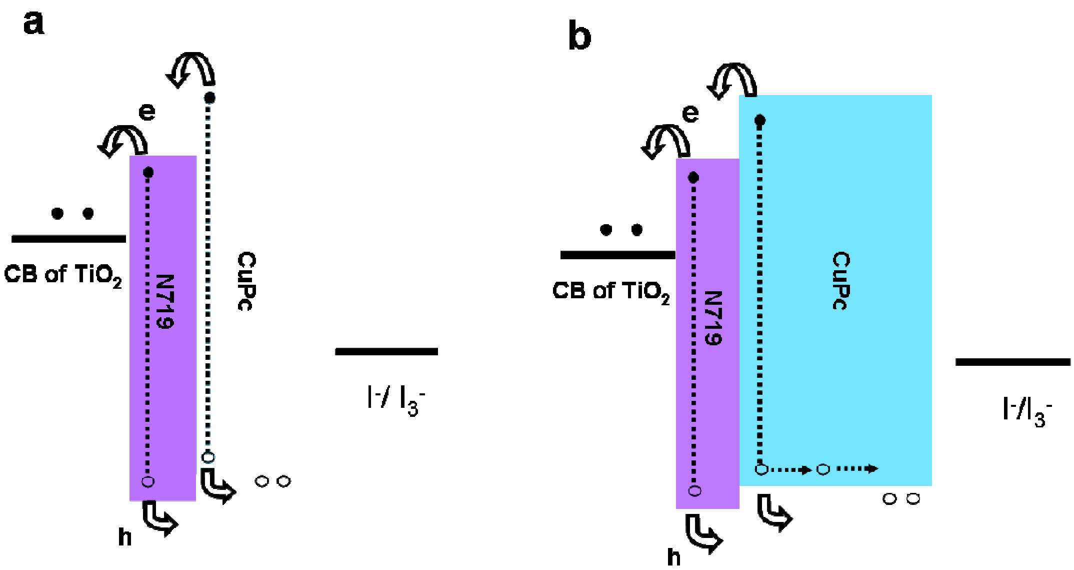

Fig 5.14 Schematic of holes transfer process in DSSC with core-shell photoanode: a with thinner CuPc shell; b, with thicker CuPc shell.

5.4 Conclusions

In conclusion, the results presented in this chapter demonstrate the viability of application of our novel photoanode with core-shell nanofiber structure in DSSC. The core TiO_2 nanofiber sensitized with one dye (N719), and the shell made from a second dye (CuPc), has the complementary absorption region that can broaden the absorption spectrum of device. The surface roughness and porosity of the semiconductor nanofiber provide favorable deposition of the dyes while the one-dimensional nanofibers further facilitate electron transport. Realization of high efficiency device, renewable energy solution is possible provided that a much more favorable dye, when compared to CuPc, can be identified.

Chapter 6.

Improved Electron Collection in Dye Sensitized Solar Cell Based on Electrospun TiO_2 Nanorod Incorporated with Carbon Nanotube

6.1 Introduction

As discussed in the previous chapters, through incorporating the novel scattering layer or introducing another dye in form of a shell wrapping the TiO_2 nanofibers in the photoanode can improve the light harvesting efficiency thereby enhance the total power conversion efficiency of the DSSC device. As well established in the literature, the electron transport in nanoparticle-based device is limited by the trap-limited diffusion process. The slow charge diffusion increases the probability of recombination, resulting in lower efficiency for the device. Moreover, the grain boundaries encountered during electron transport lead to fast recombination prior to their collection at the electrode. Much effort has been devoted to improve the charge transport property and collection efficiency.

One promising solution is to use one-dimensional nanostructure photoanode to replace the nanoparticle film, which provides a direct pathway for collection of charges generated throughout the device. Electron transport in one-dimensional nanostructure, such as nanowire, nanofiber, and nanorod is expected to be several orders of magnitude faster than that of nanoparticles. Another approach to improve the electron transport and collection is by incorporating highly electrically conductive materials, such as carbon tube, graphite, in a titanium photoanode. The presence of effective conductivity materials in the titanium photoanode is expected to improve the charge transport properties and extend the electron lifetime thereby improving the performance of the device. Several groups have reported that utilizing nanocomposites photoanodes, such as titanium/carbon nanotube, titanium/graphene, can enhance electron transport and collection efficiency [48, 49, 79-81].

Based on the idea of deploying direct-charge transport superhighway, here, the one-dimensional nanomaterials, TiO_2 nanorod and multiwall carbon nanotube (MWCNT), were both incorporated into the photoanode for DSSC. Specifically, the MWCNT is inserted in the TiO_2 nanorod by electrospinning with a simple one-step approach. Incorporating the MWCNT into TiO_2 nanorod can enhance the charge transport rate and improve the efficiency of the device. An impressive PCE of 10.24% has been achieved with a high FF of 74%[82].

6.2 Experiments

TiO_2/ PVP/ MWCNT composite nanofibers were first electrospun on FTO glass from precursor solution which contained TIP(4g), PVP (3.5g), acetic acid (2g), MWCNT (0.05～0.15g) and ethanol (100mL). The voltage of 70kV was applied over a collector distance of 19 cm. A layer of TiO_2 nanorods incorporated with MWCNT were peeled off from the original FTO glass after calcination and then transferred to another FTO glass with an ultra-thin adhesive TiO_2 paste. The TiO_2 nanorod photoanode incorporated with MWCNT was obtained after calcinating again at 450 °C for 2 hrs.

Before sensitization, the photoanode was first treated with an aqueous solution of 40mM $TiCl_4$ at 60°C for 15 min. After treatment, the photoanode was washed with ethanol and dried in vacuum at 80 ^{o}C. Subsequently, it was immersed in a solution of 0.3 mM N719 dye in absolute ethanol at 55°C for 24 h. The soaked photoanodes was then washed with absolute ethanol to remove “unanchored” dye molecules and subsequently dried in vacuum at room temperature.

Pt-sputtered FTO glass was used as the counter electrode. The counter electrode and dye-anchored photoanode were assembled into a sandwich structure with surlyn (DuPont, 25 μm). The internal space of the device was filled with an electrolyte.

6.3 Results and Discussion

Incorporating CNT into titanium nanosphere photoanode has been reported in many literatures. However, we have made an unique step different from others, which is to replace the previous attempt of using nanospheres wrapping the CNT by the one-dimensional titanium nanostructure to further improve the charge transport property. In our novel architecture, CNTs are inserted inside the TiO_2 nanorods. The charge transport routes in these three different architectures are depicted in **Scheme 6.1**. Among these three routes, electrons should be most effectively transported and collected in scheme 1c with minimal electron loss.

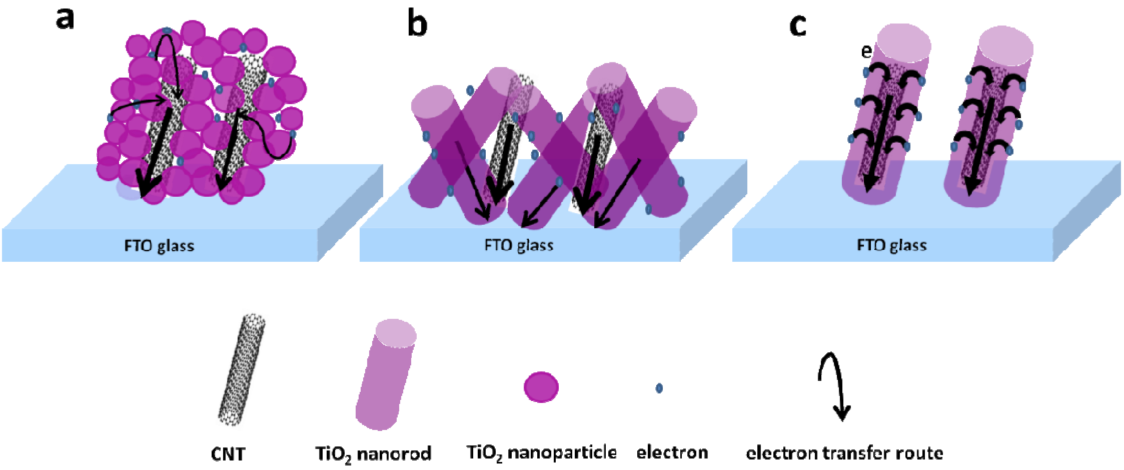

Scheme 6.1. Electron transport across photoanode: (1) CNTs totally surrounded/embraced by TiO_2 nanoparticles, (b) CNTs totally surrounded/embraced by TiO_2 nanorods, and (c) CNTs inside TiO_2 nanorods. The thickness of the arrow represents the electron transport speed, with thicker arrow representing faster electron transport

Fig 6.1 a displays the SEM image of TiO_2 nanorods incorporating MWCNT. The diameter of the nanorod is approximately 70nm, and the length of the nanorods is of order of hundreds of nanometers. Note that the MWCNT is not visible from the SEM image, which suggests that the MWCNT might be inside the TiO_2 nanorods.

Fig 6.1 b to d displays the related TEM images. From the TEM image of MWCNT (Fig 6.1 b), it can be seen that the outside diameter of the MWCNT ranges from 7 to 12nm and the inside diameter is about 3nm. The electrospun TiO_2 nanorods incorporating MWCNTs exhibits clear crystal lattice fringes (Fig 6.1 c and d).

The crystal inter-planar spacing of the TiO_2 grains is about 0.35nm corresponding to (101) planes of the anatase phase. On the other hand, the crystal inter-planar of 0.34nm corresponds to the (002) plane of the MWCNT. The foregoing morphology analysis indeed confirmed the MWCNTs were inside the TiO_2 nanorods.

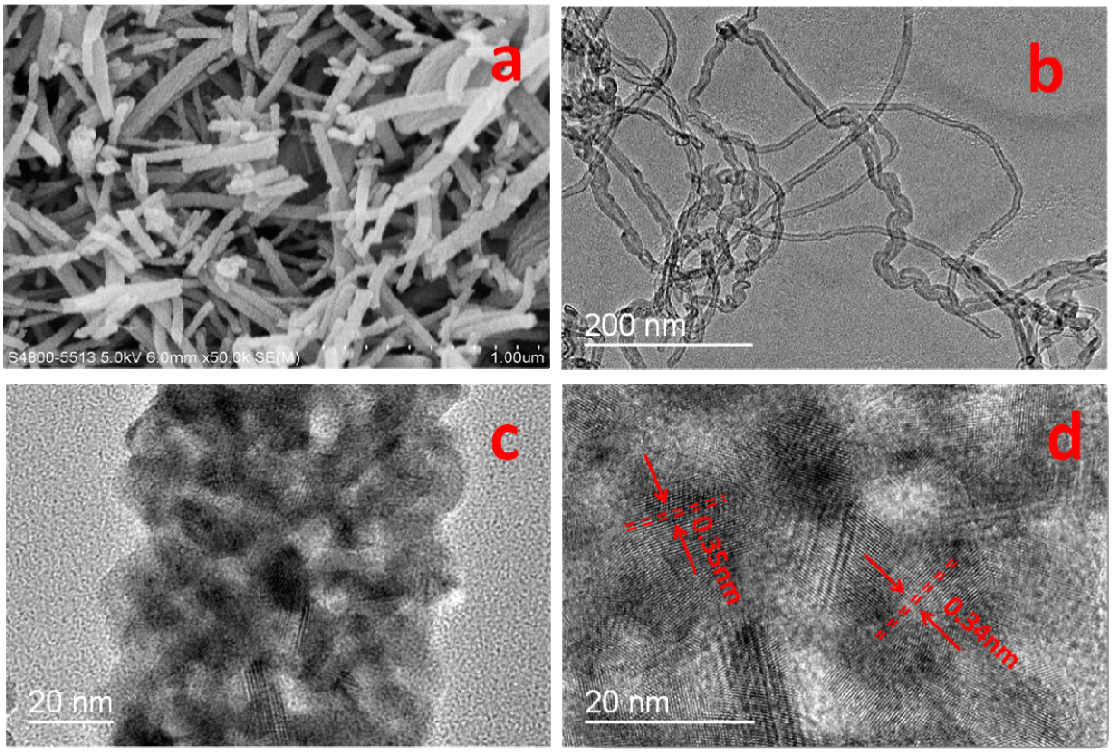

Fig 6. 1. SEM and TEM images: a. SEM image of TiO_2 nanorod incorporating MWCNTs; b and c are TEM images, respectively, of MWCNTs and TiO_2 nanorods incorporating MWCNTs; d. HRTEM image of TiO_2 nanorods incorporating MWCNTs.

Fig 6.2 a and b are, respectively, the XPS spectra of TiO_2 nanorod photoanode with and without MWCNT, which further confirm the presence of MWCNTs in the TiO_2 nanorods. The results shows that C 1s peak of photoanode with 0.1wt% MWCNT (in precursor solution for electrospinning) was stronger than that without MWCNT, which suggests that the MWCNTs were successful incorporated in the TiO_2 nanorods of the photoanode.

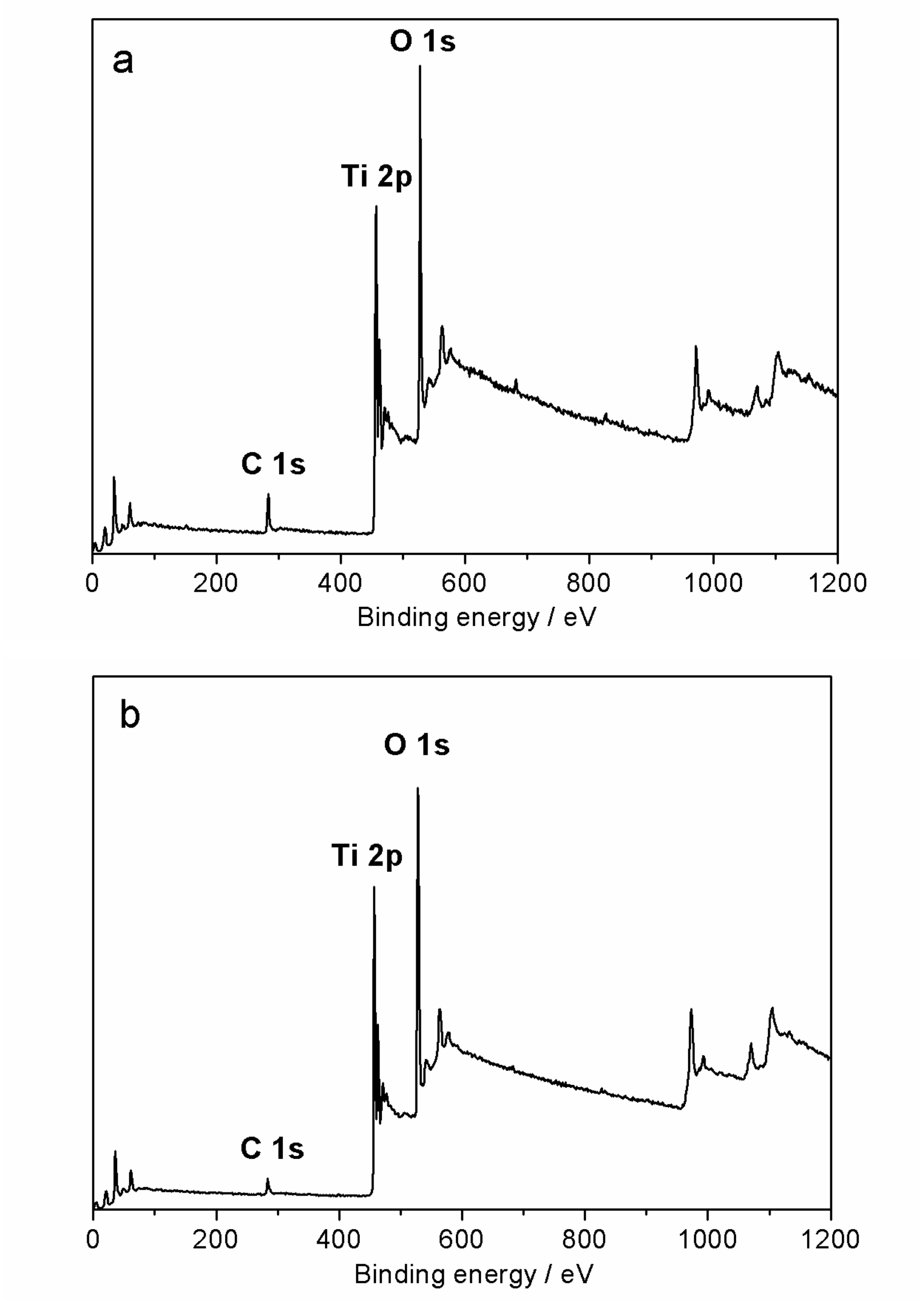

Fig 6. 2. XPS spectra of photoanode: a. with MWCNT (0.1wt% in precursor solution), and b. without MWCNT

Fig 6.3 is the Raman spectra of MWCNT, electrospun TiO_2 nanorod without and with MWCNT, respectively. From Fig 6.3, it can be observed that the disorder-induced D-band and G-band modes of MWCNT, peaks correspond to 1375 and 1575cm^{-1}, thus the D/G band ratio is 0.93. It is interesting to find that the intensity of G-band modes of MWCNT was reduced when the MWCNT was incorporated in the TiO_2 nanorods, while a new peak was observed at lower frequency approximately at 1850cm^{-1}, which corresponds to the one-dimensional linear C-chains consisting of more than 40 atoms inside the MWCNT[50, 53].

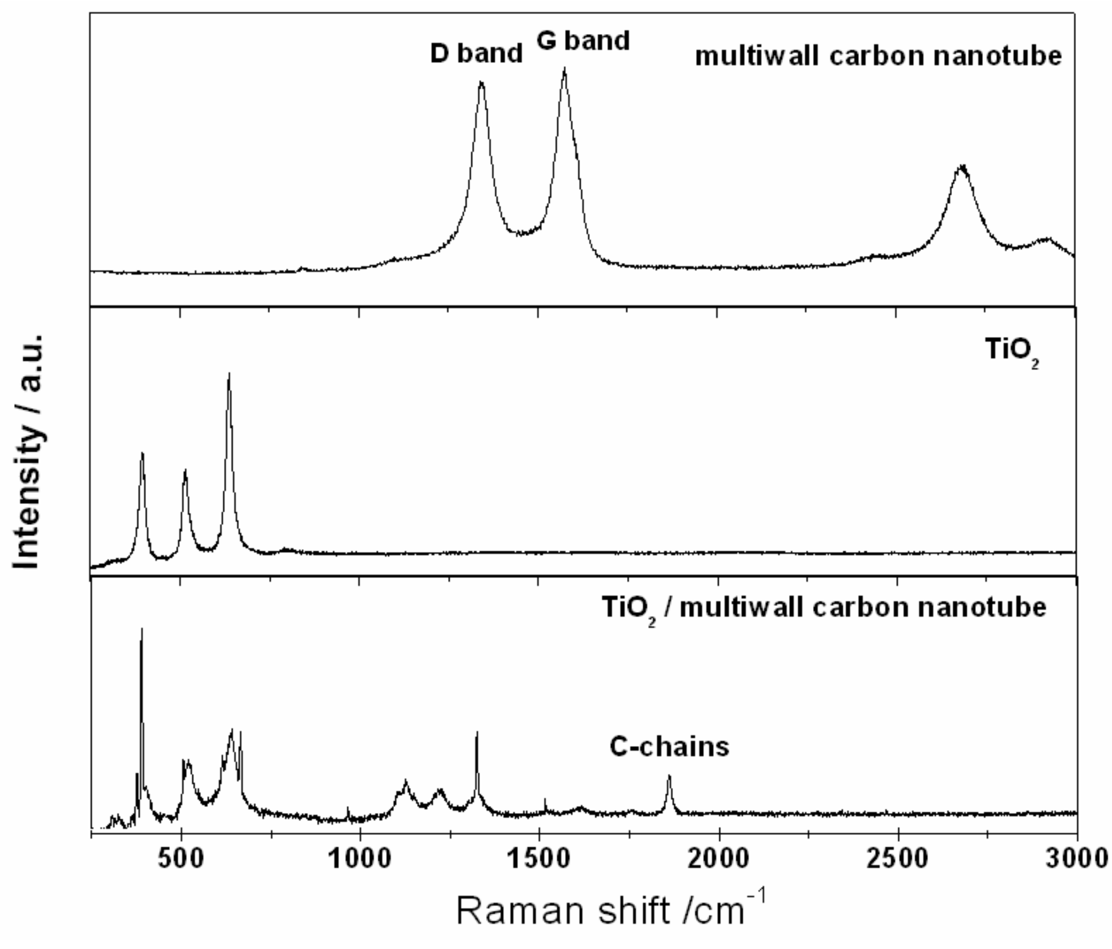

Fig 6.3 Raman spectra respectively of MWCNT, TiO_2 nanorod photoanode without and with MWCNT

To investigate the effect of thickness of the photoanode on the performance of the DSSC device, two sets devices each with different photoanode thickness, respectively, 6.6±0.7μm and 14.3±0.3 μm have been developed for the photovoltaic test. Furthermore, for each device the effect of MWCNT concentrations, respectively, 0.05, 0.10, and 0.15% in the precursor solution, on the performance of the device was also investigated. The performance on the device of TiO_2 nanofiber photoanode without MWCNT was determined for reference.

Fig 6.4 shows the typical *J-V* curves of these test devices. The details of the photovoltaic parameters, such as J_{sc}, V_{oc}, FF and PCE, were tabulated in Table 6.1. From the *J-V* curves and Table 6.1, it can be deduced that the FF has been substantially improved through introducing the MWCNT into the photoanode. With the same amount of MWCNT, the thicker photoanode shows both higher J_{sc} and V_{oc}.

To investigate the effect of the dosage of MWCNT in the photoanode on the performance of the DSSC device, different samples with weight percentages of MWCNT from 0.05% to 0.15% in the precursor solution for electrospinning were prepared. Fig 6.5 shows the effect of amount of MWCNT on J_{sc} and FF. By increasing the concentration of MWCNT from 0.05% to 0.1% for the thinner photoanode, J_{sc} increased from 8.92 to 11.1mAcm^{-2}, a 24%

improvement. On the other hand, similar tests in varying the concentration of MWCNT from 0.05% to 0.1% for the thicker photoanode shows 30% enhancement in J_{sc} can be realized.

However, both J_{sc} and PCE decreased in both sets of photoanode devices with further increase in the amount of MWCNT in the precursor solution to 0.15%. It is conjectured that excess MWCNT might have deposited on the surface of the TiO2 nanofibers precluding the N719 deposition on the nanofibers. Despite this reverse trend, the FF maintained increasing with increasing the amount of MWCNT.

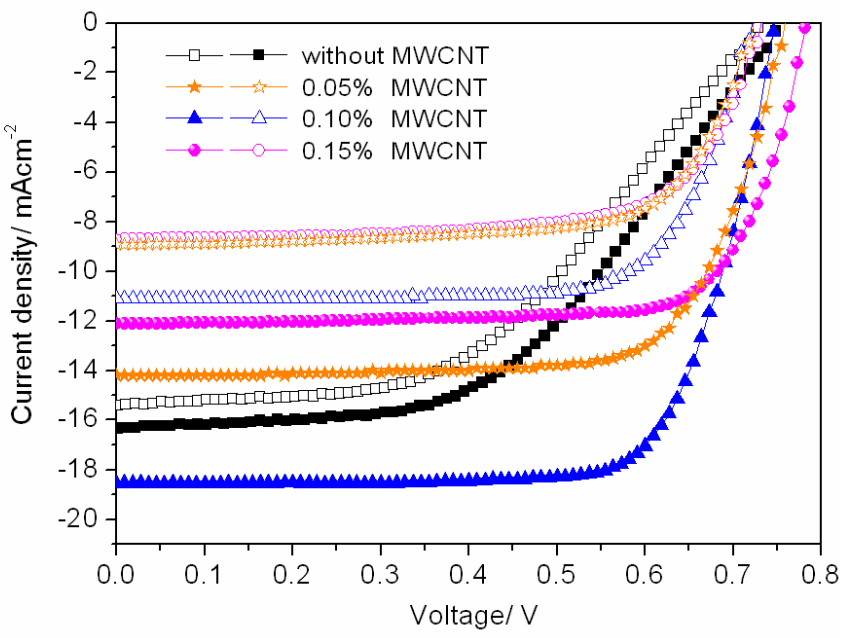

Fig 6.4. *J-V* characteristics of different photoanodes, hollow-symbol curve represents thinner photoanode with thickness about 6.6±0.7μm, and solid-symbol curve represents thicker photoanode with thickness about 14.3±0.3μm

Table 6.1 Photovoltaic parameters for DSSC with different photoanode

MWCNT in precursor solution	Thickness/μm	V_{oc}/V	J_{sc}/mAcm^{-2}	FF /%	PCE/%
0	7.90	0.73	15.40	50.08	5.63
	16.7	0.74	16.30	51.24	6.18
0.05 wt.%	6.70	0.72	8.92	70.22	4.51
	14.47	0.76	14.20	72.27	7.80
0.10 wt.%	6.04	0.72	11.10	73.07	5.84
	14.64	0.75	18.53	73.68	10.24
0.15 wt.%	7.32	0.73	8.72	75.87	4.38
	13.97	0.78	12.11	75.54	7.13

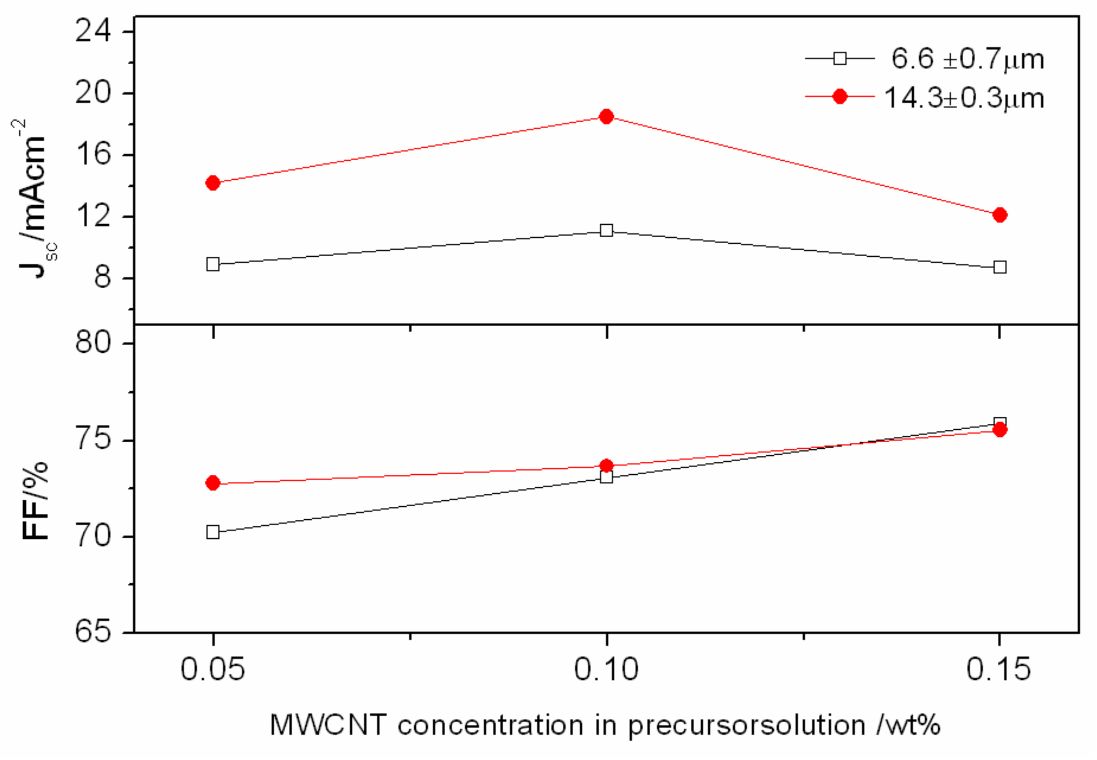

Fig 6.5. The effect of MWCNT concentration in precursor solution on J_{sc} and FF

The external quantum efficiency (EQE) measurement was carried out to further investigate the mechanism of enhancement in device performance. As seen in Fig 6.6, the normalized EQE response at the entire visible-light wavelength (350-700nm) is enhanced when the concentration of MWCNT in the precursor solution was increased from 0.05% to 0.10%. However, further increase in the concentration of MWCNT to 0.15%, results in reduction in EQE across the entire visible-light wavelength. It can be understood from the following. Given the MWCNT is incorporated inside the photoanode; it can rapidly capture and transport the photogenerated electrons and concurrently reduce the undesirable recombination and back-reaction. Therefore, at lower MWCNT concentration increasing the amount of MWCNT in the photoanode improves the charge collection efficiency and reduces the recombination, which results in improved performance, i.e. J_{sc} and EQE. However, at higher MWCNT concentration, there is competition of light harvesting between dye molecules (N719) and MWCNT, and as a result the dye loading capacity and thereby the power conversion efficiency are both reduced[79]. Therefore, it is necessary to optimize the amount of MWCNT in the photoanode to balance the electron transport property and dye loading capacity.

Upon optimization of the parameters for the photoanode, the high conversion efficiency of 10.24% has been attained for the photoanode with TiO_2 nanorods incorporating 0.1% MWCNT in the precursor solution for electrospinning. It is important to note that the improved efficiency for the photoanode incorporating MWCNT is largely due to the improved FF. Based on our previous studies[34], the FF of devices without incorporating MWCNT in the photoanode were typically between 50% and 55%. While incorporating MWCNT in the photoanode, the FF is boost to 70-75%, which is a 35% increase. Therefore, introducing MWCNT in the photoanode can improve the charge transport properties and suppress the recombination, both of which lead to improving the charge collection efficiency.

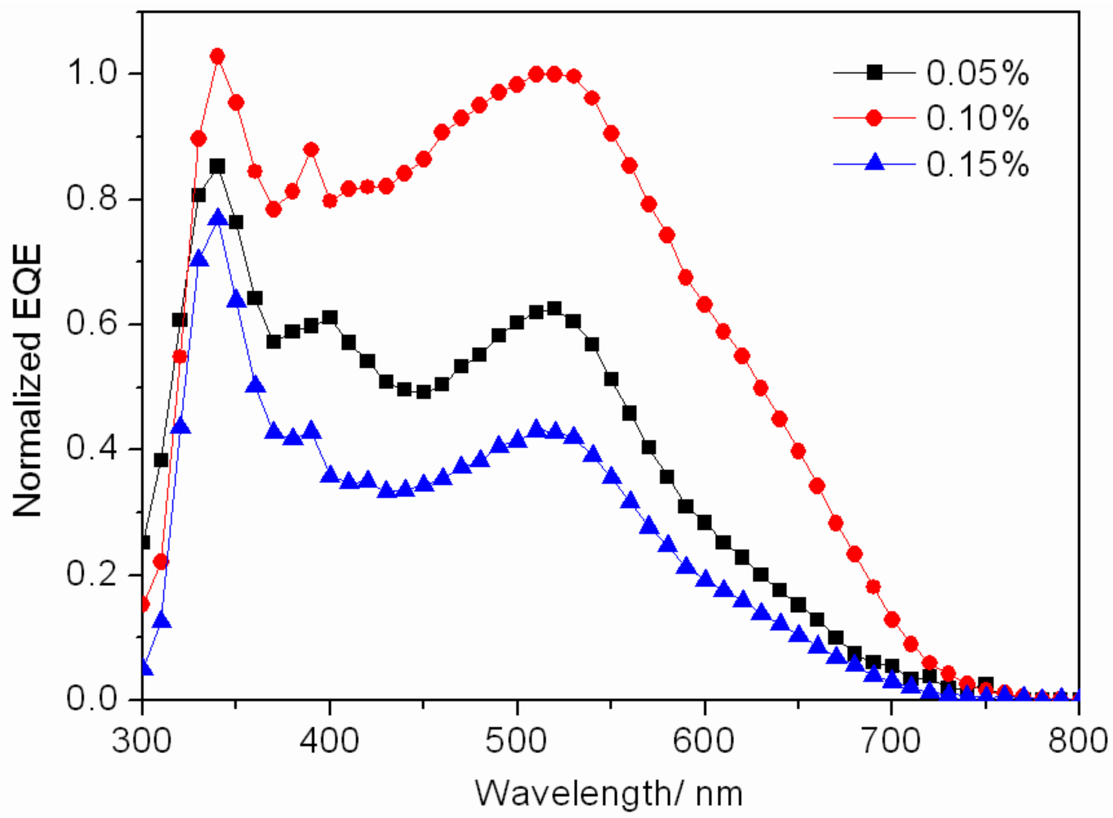

Fig 6.6. Normalized EQE spectra of thicker photoanode with different MWCNT concentration in precursor solution

6.4 Conclusions

In summary, MWCNT, an ideal electron transport superhighway, was introduced inside the electrospun TiO_2 nanorods. This configuration was successfully applied in the photoanode to improve the performance of DSSC device. The effect on the performance of the device for different concentrations of MWCNT in the precursor solution for electrospinning was investigated. The FF of the DSSC device increased with the MWCNT amount in the nanorods from 0.05% to 0.15% (in precursor solution). The J_{sc} first increased due to improved electron charge transport property and subsequently it decreased due to lower dye loading capacity of the photoanode at higher MWCNT concentration. With 0.1% MWCNT concentration, the DSSC device exhibited the highest efficiency of 10.24%, with the high J_{sc} of 18.53 $mAcm^{-2}$ and FF of 74%. The improved efficiency is largely due to the improved FF. These positive results confirm that the electrospun nanorods incorporating MWCNT provide an effective means to best utilize economical materials for developing photoanode with efficient charge transport properties for realizing solar energy conversion in the future.

Chapter 7

Conclusion and Further Work

7.1 Conclusion

In this thesis, the one-dimensional nanostructure material, TiO_2 nanofiber, is adopted for the photoanode replacing the conventional TiO_2 nanoparticles, which provide a direct path for electron transport and collection. There are several advantages of nanofibers that supersede the shortfall of nanoparticles. The TiO_2 nanofiber is composed of closely packed anatase single crystallites with sizes less than 10 nm, which shows large surface-to-volume ratio thereby favors dye adsorption. A high efficiency of 7.14% can be obtained in DSSC device based on TiO_2 nanofiber photoanode.

To further improve the efficiency of the DSSC based on TiO_2 nanofiber photoanode, two novel scattering layers were introduced in the photoanode to improve the light harvesting efficiency. The optimal high efficiency of 8.71% and 9.28% were achieved with the polydispersed-size TiO_2 nanoparticles and bigger diameter TiO_2 nanofiber as the scattering layer, respectively.

Another approach to improve the light harvesting efficiency is to utilize the dye cocktail. In chapter 5, a novel design of core-shell photoanode where a thin-shell of infrared dye was deposited on the core of sensitized TiO_2 nanofiber has been developed. In such architecture, photons are absorbed by the infrared dye and undergo charge transfer to the sensitizing dye, which not only broadens the absorption spectrum but further suppresses the recombination process. Specifically, in our tests the ruthenium-based dye (N719) sensitized TiO_2 nanofibers were wrapped by thin-shell of copper phthalocyanine (CuPc), a high efficiency of 9.48% was achieved.

Finally, to enhance the charge transfer and collection efficiency, multiwall carbon nanotube was incorporated in the TiO_2 nanorod photoanode. Embedded in the nanorod, the multiwall carbon nanotubes can effectively transport and collect photogenerated electrons thus reducing the recombination, thereby improving the efficiency of the device. A high efficiency of 10.24% was achieved in our tests with a high fill factor of 74%.

7.2 Further work

The most commonly used redox couple in an liquid electrolyte based DSSC device is iodide/tri-iodide (I^-/I_3^-), however, it is highly corrosive, volatile and photoreactive, interacting with common metallic components and sealing materials, which causes serious problems such as electrode corrosion, electrolyte evaporation and leakage. Consequently, these affect adversely the long-term performance and durability of the solar cell. One solution is to replace the iodine-based liquid electrolytes with solid, or quasi-solid, electrolyte to solve these problems.

Considerable efforts have been made to utilize solid-state organic, or inorganic p–type, hole transport materials (HTMs) to replace liquid electrolyte in DSSC[83, 84]. Inorganic p-type HTMs, such as CuI, CuBr, NiO or CuSCN, have been used as HTM candidates in SSDSSC but the power conversion efficiency of these devices were relative low (2-4%) when compared with liquid-based electrolyte devices[85-89].2,2’7,7’-tetrakis(N,N-di-p-methoxyphenyl-amine)-9,9’-spirobifluorene(Spiro-OMeTAD) is by far the most successful P-type organic HTM in solid-state DSSC with the efficiency of 6.08% [90].

A major obstacle of solid-state DSSC is that the solid HTMs (after dissolution in appropriate solvent) are difficult to fill the voids in the nanoporous TiO_2 layer. Currently, the effective photoanode thickness of the devices with solid HTMs has been limited by their penetration depth into the mesoporous TiO_2 layer to about 2 μm. The nano-scale pore diameter (less than 20 nm) and narrow pore structure of the photoanode made of TiO_2 nanoparticles (~20 nm), implying low porosity and permeability, render the HTMs (in solution) with relative high viscosity difficult to penetrate deeply into the mesoporous TiO_2 layer. Siamak Nejati used the initiated chemical vapor deposition (iCVD) technology to deposit HTM in photoanode, and their results showed that control iCVD conditions could achieve complete pore-filling for electrode with thicknesses up to 12 μm, which provided an effective way to overcome the hurdle[91]. Due to the more open structure, adopting TiO_2 nanotube as the photoanode to facilitate the polymer electrolyte to penetrate easily into the film, Ismael C. Flores *et al* achieved an efficiency of only 4.03% with their photoanode despite its thickness of 12μm[92]. A possible explanation is that air was trapped in open pores which disrupted the conduction path of the HTM in their thick photoanode.

The limited thickness of photoanode with nanoparticles due to the poor pore-filling brings out another shortcoming, the low light harvesting efficiency. The optical design of solid-state DSSC with thin-film photoanode is far from optimized, with more than 30% of the incident light at the strong absorption region of the dye being lost unless a very strong absorber is used, which is rare. An important challenge for solid-state DSSC is to obtain high light harvesting efficiency. Incorporation of more than one dye/absorber in the device is considered as an effective method to increase the light harvesting efficiency through extending the absorption spectrum based on either charge or energy transfer [93-95]. Recently, Kristina Driscoll blended the HTM, spiro-OMeTAD, with the secondary near-infrared dye, which can extend the spectral response of solid-state excitonic solar cells leading to improved PCE in comparison with using only the standard-dye devices[95].

The other drawback of solid-state DSSC is the fast electron-hole recombination at the interface of HTM/ TiO_2. The recombination rate is much higher than that in liquid electrolyte device because the recombination of electron with I^-/I_3^- in the liquid-electrolyte device depends on a chemical reaction, while in solid-state device holes recombine with electron via a much faster electronic process. In several publications[96-99], coating an insulating layer, such as Al_2O_3, SiO_2, $SrTiO_3$, on the surface of TiO_2 could increase the efficiency of solid-state DSSC by reducing the recombination. O'Regan *et al* inserted a thin layer of Al_2O_3 in the interface of TiO_2/ CuSCN in solid-state DSSC. As a result the fill factor, which measures the recombination rate, has been improved[96].

In summary, the major problems that limit the performance of solid-state DSSC device are: (1) it is difficult for HTM to penetrate completely into the pores in the mesoporous TiO_2 photoanode; (2) poor light harvesting efficiency at the strong dye absorption region; and (3) fast recombination rate at the interface between TiO_2 and HTM. If these hurdles can be addressed, the solid-state DSSC can bring the energy sector a promising future.

Based on our past experience [34, 82], using electrospun TiO_2 nanofiber to prepare a photoanode for solid-state DSSC is possible. Comparing with the TiO_2 nanoparticles (~20nm diameter) layer, the nanofiber (~60nm diameter) mat exhibits higher pore volume and lower solid packing density that lead to high permeability. The viscous HTM solution can effectively penetrate into the mat, more so as compared to the mat made of close-size small nanoparticles. This can be seen from Fig. 3.8 a that the diameter of pores in the TiO_2 nanofiber mat ranges from hundreds of nanometers to several micrometers.

Bibliography

[1] M. Gratzel, *Nature* **2001**, *414*, 338.

[2] M. A. Green, *Solar cells:Operating principles, Technology and System Applications*, Prentice-Hall, **1982**.

[3] M. Gratzel, *Inorganic Chemistry* **2005**, *44*, 6841.

[4] B. O'Regan, M. Gratzel, *Nature* **1991**, *353*, 737.

[5] L. M. Goncalves, V. de Zea Bermudez, H. A. Ribeiro, A. M. Mendes, *Energy & Environmental Science* **2008**, *1*, 655.

[6] J. Burschka, N. Pellet, S.-J. Moon, R. Humphry-Baker, P. Gao, M. K. Nazeeruddin, M. Gratzel, *Nature* **2013**, *499*, 316.

[7] S. J. Fonash, *Solar cell device physics* Academic Press, **2010**.

[8] M. A. Green, *Third generation photovoltaics: advanced solar energy conversion,* Berlin, New York, Springer, **2003**.

[9] S. Bailey, J. McNatt, R. Raffaelle, S. Hubbard, D. Forbes, L. Fritzenmeier, W. Maurer, in *Photovoltaic Specialists Conference (PVSC), 2009 34th IEEE*, **2009**, pp. 001909.

[10] I. Repins, M. Contreras, M. Romero, Y. Yan, W. Metzger, J. Li, S. Johnston, B. Egass, C. DeHart, J. Scharf, B. E. McCandless, R. Noufi, *Characterization of 19.9% Efficient CIGS Absorbers: Preprint*, **2008**.

[11] K.Kalyanasundaram, *Dye-sensitized solar cells*, CRC Press, **2010**.

[12] R. F.Pierret, *Semiconductor Device Fundamentals*, Addison-Wesley,

1996.

[13] J. Moser, *Monatshefte fur Chemie und verwandte Teile anderer Wissenschaften* **1887**, *8*, 373.

[14] S. Namba, Y. Hishiki, *The Journal of Physical Chemistry* **1965**, *69*, 774.

[15] J. Bourdon, *The Journal of Physical Chemistry* **1965**, *69*, 705.

[16] H. Tributsch, H. Gerischer, *Berichte der Bunsengesellschaft für physikalische Chemie* **1969**, *73*, 850.

[17] A. Yella, H.-W. Lee, H. N. Tsao, C. Yi, A. K. Chandiran, M. K. Nazeeruddin, E. W.-G. Diau, C.-Y. Yeh, S. M. Zakeeruddin, M. Gratzel, *Science* **2011**, *334*, 629.

[18] M. Grätzel, *Journal of Photochemistry and Photobiology C: Photochemistry Reviews* **2003**, *4*, 145.

[19] X.-L. Yu, J.-G. Song, Y.-S. Fu, Y. Xie, X. Song, J. Sun, X.-W. Du, *The Journal of Physical Chemistry C* **2011**, *114*, 2380.

[20] J. Qian, P. Liu, Y. Xiao, Y. Jiang, Y. Cao, X. Ai, H. Yang, *Advanced Materials* **2009**, *21*, 3663.

[21] S. Gubbala, V. Chakrapani, V. Kumar, M. K. Sunkara, *Advanced Functional Materials* **2008**, *18*, 2411.

[22] K. Hayamizu, Y. Aihara, S. Arai, W. S. Price, *Solid State Ionics* **1998**, *107*, 1.

[23] J.-H. Yum, P. Chen, M. Grätzel, M. K. Nazeeruddin, *ChemSusChem* **2008**, *1*, 699.

[24] N. Robertson, *Angewandte Chemie International Edition* **2006**, *45*, 2338.

[25] J.-J. Cid, J.-H. Yum, S.-R. Jang, M. K. Nazeeruddin, E. Martínez-Ferrero, E. Palomares, J. Ko, M. Grätzel, T. Torres, *Angewandte Chemie* **2007**, *119*, 8510.

[26] J. N. Clifford, A. Forneli, H. Chen, T. Torres, S. Tan, E. Palomares, *Journal of Materials Chemistry* **2011**, *21*, 1693.

[27] N. W. Duffy, L. M. Peter, R. M. G. Rajapakse, K. G. U. Wijayantha, *The Journal of Physical Chemistry B* **2000**, *104*, 8916.

[28] B. H. Lee, M. Y. Song, S.-Y. Jang, S. M. Jo, S.-Y. Kwak, D. Y. Kim, *The Journal of Physical Chemistry C* **2009**, *113*, 21453.

[29] T. Oekermann, D. Zhang, T. Yoshida, H. Minoura, *The Journal of Physical Chemistry B* **2004**, *108*, 2227.

[30] M. A. Green, K. Emery, Y. Hishikawa, W. Warta, E. D. Dunlop, *Progress in Photovoltaics: Research and Applications* **2012**, *20*, 12.

[31] M. Law, L. E. Greene, J. C. Johnson, R. Saykally, P. Yang, *Nat Mater* **2005**, *4*, 455.

[32] P. Joshi, L. Zhang, D. Davoux, Z. Zhu, D. Galipeau, H. Fong, Q. Qiao, *Energy & Environmental Science* **2010**, *3*, 1507.

[33] S. H. Ko, D. Lee, H. W. Kang, K. H. Nam, J. Y. Yeo, S. J. Hong, C. P. Grigoropoulos, H. J. Sung, *Nano Letters* **2010**, *11*, 666.

[34] L. Yang, W. W.-F. Leung, *Advanced Materials* **2011**, *23*, 4559.

[35] X. Feng, K. Zhu, A. J. Frank, C. A. Grimes, T. E. Mallouk, *Angewandte Chemie* **2012**, *124*, 2781.

[36] W. Guo, X. Xue, S. Wang, C. Lin, Z. L. Wang, *Nano Letters* **2012**, *12*, 2520.

[37] Y. Li, Z. Liu, C. Liu, J. Ya, L. E, W. Zhao, Q. Chen, J. Bai, *Journal of the American Ceramic Society*, *95*, 1343.

[38] M. Kimura, H. Nomoto, N. Masaki, S. Mori, *Angewandte Chemie International Edition* **2012**, *51*, 1.

[39] W. M. Campbell, K. W. Jolley, P. Wagner, K. Wagner, P. J. Walsh, K. C. Gordon, L. Schmidt-Mende, M. K. Nazeeruddin, Q. Wang, M. GrÃ¤tzel, D. L. Officer, *The Journal of Physical Chemistry C* **2007**, *111*, 11760.

[40] F. Huang, D. Chen, X. L. Zhang, R. A. Caruso, Y.-B. Cheng, *Advanced Functional Materials* **2010**, *20*, 1301.

[41] A. Usami, *Chemical Physics Letters* **1997**, *277*, 105.

[42] S. Hore, P. Nitz, C. Vetter, C. Prahl, M. Niggemann, R. Kern, *Chemical Communications* **2005**, 2011.

[43] S. Hore, C. Vetter, R. Kern, H. Smit, A. Hinsch, *Solar Energy Materials and Solar Cells* **2006**, *90*, 1176.

[44] C.-H. Yip, Y.-M. Chiang, C.-C. Wong, *The Journal of Physical Chemistry C* **2008**, *112*, 8735.

[45] S. Chappel, S.-G. Chen, A. Zaban, *Langmuir* **2002**, *18*, 3336.

[46] Y. Diamant, S. G. Chen, O. Melamed, A. Zaban, *The Journal of*

Physical Chemistry B **2003**, *107*, 1977.

[47] N. G. Park, G. Schlichthorl, J. van de Lagemaat, H. M. Cheong, A. Mascarenhas, A. J. Frank, *The Journal of Physical Chemistry B* **1999**, *103*, 3308.

[48] X. Dang, H. Yi, M.-H. Ham, J. Qi, D. S. Yun, R. Ladewski, M. S. Strano, P. T. Hammond, A. M. Belcher, *Nat Nano* **2011**, *6*, 377.

[49] Y. H. Jang, X. Xin, M. Byun, Y. J. Jang, Z. Lin, D. H. Kim, *Nano Letters* **2011**, *12*, 479.

[50] V. Scuderi, S. Scalese, S. Bagiante, G. Compagnini, L. Durso, V. Privitera, *Carbon* **2009**, *47*, 2134.

[51] J. F. Watt, *An introduction to surface analysis by XPS and AES,* Wiley, **2003**.

[52] A. Hu, S. Griesing, M. Rybachuk, Q.-B. Lu, W. W. Duley, *Journal of Applied Physics* **2007**, *102*, 074311.

[53] X. Zhao, Y. Ando, Y. Liu, M. Jinno, T. Suzuki, *Physical Review Letters* **2003**, *90*, 187401.

[54] L. Han, N. Koide, Y. Chiba, T. Mitate, *Applied Physics Letters* **2004**, *84*, 2433.

[55] C.-P. Hsu, K.-M. Lee, J. T.-W. Huang, C.-Y. Lin, C.-H. Lee, L.-P. Wang, S.-Y. Tsai, K.-C. Ho, *Electrochimica Acta* **2008**, *53*, 7514.

[56] A. Greiner, J. H. Wendorff, *Angewandte Chemie International Edition* **2007**, *46*, 5670.

[57] Z.-M. Huang, Y. Z. Zhang, M. Kotaki, S. Ramakrishna, *Composites Science and Technology* **2003**, *63*, 2223.

[58] R. Chandrasekar, L. Zhang, J. Howe, N. Hedin, Y. Zhang, H. Fong, *Journal of Materials Science* **2009**, *44*, 1198.

[59] I. S. Chronakis, *Journal of Materials Processing Technology* **2005**, *167*, 283.

[60] J. M. Deitzel, J. Kleinmeyer, D. Harris, N. C. Beck Tan, *Polymer* **2001**, *42*, 261.

[61] C. L. Casper, J. S. Stephens, N. G. Tassi, D. B. Chase, J. F. Rabolt, *Macromolecules* **2003**, *37*, 573.

[62] C. Tanford, *Physical chemistry of macromolecules*, New York, Wiley, **1961**.

[63] M. U. Beer, P. J. Wood, J. Weisz, *Carbohydrate Polymers* **1999**, *39*, 377.

[64] J. Ferber, J. Luther, *Solar Energy Materials and Solar Cells* **1998**, *54*, 265.

[65] X. Zhao, H. Lin, X. Li, J. Li, *Materials Letters* **2011**, *65*, 1157.

[66] S. Chuangchote, T. Sagawa, S. Yoshikawa, *Applied Physics Letters* **2008**, *93*, 033310.

[67] P. Zhu, A. S. Nair, S. Yang, S. Peng, S. Ramakrishna, *Journal of Materials Chemistry* **2011**, *21*, 12210.

[68] E. Garnett, P. Yang, *Nano Letters* **2010**, *10*, 1082.

[69] P. Wang, S. M. Zakeeruddin, J. E. Moser, M. K. Nazeeruddin, T. Sekiguchi, M. Gratzel, *Nat Mater* **2003**, *2*, 402.

[70] M. K. Nazeeruddin, F. De Angelis, S. Fantacci, A. Selloni, G. Viscardi, P. Liska, S. Ito, B. Takeru, M. Gratzel, *Journal of the American Chemical Society* **2005**, *127*, 16835.

[71] G. K. Mor, J. Basham, M. Paulose, S. Kim, O. K. Varghese, A. Vaish, S. Yoriya, C. A. Grimes, *Nano Letters* **2010**, *10*, 2387.

[72] K. Shankar, X. Feng, C. A. Grimes, *ACS Nano* **2009**, *3*, 788.

[73] S. R. Scully, P. B. Armstrong, C. Edder, J. M. J. Fréchet, M. D. McGehee, *Advanced Materials* **2007**, *19*, 2961.

[74] B. E. Hardin, E. T. Hoke, P. B. Armstrong, J.-H. Yum, P. Comte, T. Torres, J. M. J. Frechet, M. K. Nazeeruddin, M. Gratzel, M. D. McGehee, *Nat Photon* **2009**, *3*, 406.

[75] L. Yang, W. W.-F. Leung, *Advanced Materials* **2013**, *25*, 1792.

[76] C.-F. Chi, H.-W. Cho, H. Teng, C.-Y. Chuang, Y.-M. Chang, Y.-J. Hsu, Y.-L. Lee, *Applied Physics Letters, 98,* 012101.

[77] K. Park, J. Xi, Q. Zhang, G. Cao, *The Journal of Physical Chemistry C* **2011**, *115*, 20992.

[78] J. R. Lakowicz, *Principles of Fluorescence Spectroscopy*, New York : Kluwer Academic/Plenum, **1999**.

[79] K.-M. Lee, C.-W. Hu, H.-W. Chen, K.-C. Ho, *Solar Energy Materials and Solar Cells* **2008**, *92*, 1628.

[80] N. Yang, J. Zhai, D. Wang, Y. Chen, L. Jiang, *ACS Nano* **2010**, *4*, 887.

[81] P. Brown, K. Takechi, P. V. Kamat, *The Journal of Physical Chemistry C* **2008**, *112*, 4776.

[82] L. Yang, W. W.-F. Leung, *Advanced Materials* **2013**, *25*, 1792.

[83] Y. Bai, Y. Cao, J. Zhang, M. Wang, R. Li, P. Wang, S. M. Zakeeruddin, M. Gratzel, *Nat Mater* **2008**, *7*, 626.

[84] U. Bach, D. Lupo, P. Comte, J. E. Moser, F. Weissortel, J. Salbeck, H. Spreitzer, M. Gratzel, *Nature* **1998**, *395*, 583.

[85] J. X. Junnian Chen, Ke Fan, Tianyou Peng, , *Electrochimica Acta* **2011**.

[86] G. R. R. A. Kumara, A. Konno, G. K. R. Senadeera, P. V. V. Jayaweera, D. B. R. A. De Silva, K. Tennakone, *Solar Energy Materials and Solar Cells* **2001**, *69*, 195.

[87] J. Bandara, H. Weerasinghe, *Solar Energy Materials and Solar Cells* **2005**, *85*, 385.

[88] E. V. A. Premalal, G. R. R. A. Kumara, R. M. G. Rajapakse, M. Shimomura, K. Murakami, A. Konno, *Chemical Communications* **2010**, *46*, 3360.

[89] Q. B. Meng, K. Takahashi, X. T. Zhang, I. Sutanto, T. N. Rao, O. Sato, A. Fujishima, H. Watanabe, T. Nakamori, M. Uragami, *Langmuir* **2003**, *19*, 3572.

[90] N. Cai, S.-J. Moon, L. Cevey-Ha, T. Moehl, R. Humphry-Baker, P. Wang, S. M. Zakeeruddin, M. Gratzel, *Nano Letters* **2011**, *11*, 1452.

[91] S. Nejati, K. K. S. Lau, *Nano Letters* **2010**, *11*, 419.

[92] I. C. Flores, J. N. de Freitas, C. Longo, M.-A. De Paoli, H. Winnischofer, A. F. Nogueira, *Journal of Photochemistry and Photobiology A: Chemistry* **2007**, *189*, 153.

[93] H. Choi, S. Kim, S. O. Kang, J. Ko, M.-S. Kang, J. N. Clifford, A. Forneli, E. Palomares, M. K. Nazeeruddin, M. Grätzel, *Angewandte Chemie International Edition* **2008**, *47*, 8259.

[94] G. K. Mor, J. Basham, M. Paulose, S. Kim, O. K. Varghese, A. Vaish, S. Yoriya, C. A. Grimes, *Nano Letters*, *10*, 2387.

[95] K. Driscoll, J. Fang, N. Humphry-Baker, T. Torres, W. T. S. Huck, H. J. Snaith, R. H. Friend, *Nano Letters* **2010**, *10*, 4981.

[96] B. C. O'Regan, S. Scully, A. C. Mayer, E. Palomares, J. Durrant, *The Journal of Physical Chemistry B* **2005**, *109*, 4616.

[97] G. R. R. A. Kumara, K. Tennakone, V. P. S. Perera, A. Konno, S. Kaneko, M. Okuya, *Journal of Physics D: Applied Physics* **2001**, *34*, 868.

[98] A. Kay, M. Gratzel, *Chemistry of Materials* **2002**, *14*, 2930.

[99] V. O. Williams, N. C. Jeong, C. Prasittichai, O. K. Farha, M. J. Pellin, J. T. Hupp, *ACS Nano*, *6*, 6185.